technische universität
dortmund

Dissertation

zur Erlangung des Doktorgrades

der Naturwissenschaften

Dr. rer. nat.

Structural analysis of 1,3,7-trimethylxanthine formations on Au(111)

Malte Georg Hendrik Schulte
geboren in Meschede

2021

Lehrstuhl für Experimentelle Physik I
Fakultät Physik
Technische Universität Dortmund

Der Fakultät für Physik der Technischen Universität Dortmund zur Erlangung des akademischen Grades eines Doktors der Naturwissenschaften vorgelegte Dissertation.

Erstgutachter:	Prof. Dr. Carsten Westphal
Zweitgutachter:	Prof. Dr. Dr. Wolfgang Rhode
Abgabedatum:	18.06.2021
Prüfungsdatum:	20.08.2021

Für Annegret

Abstract

1,3,7-Trimethylxanthine ($C_8H_{10}N_4O_2$), better known as caffeine, has an asymmetric and achiral structure. These properties result in two enantiomers on the surface upon adsorption and affect the structural arrangement of the molecules on a crystalline substrate. Therefore, a structural analysis of caffeine molecules in mono- and submonomolecular coverage on weakly interacting substrates allows to study this influence.

In this work, the formation of caffeine molecules on a Au(111) surface is investigated by scanning tunneling microscopy (STM), low-energy electron diffraction (LEED), X-ray photoelectron spectroscopy (XPS), and density functional theory (DFT) calculations. The thin caffeine films are prepared by molecular beam epitaxy (MBE) in ultra-high vacuum (UHV) and studied at room temperature. In monomolecular coverage, the caffeine molecules assemble in a quasi-hexagonal phase on Au(111). Thereby, two mirrored domains are measurable with respect to the substrate surface in STM and LEED experiments. From these measurements, a periodic layer with only one molecule in the unit cell is initially deduced. In XPS experiments, no strong interaction with the substrate is observed. This motivates a theoretical analysis of the caffeine monolayer structure, which is performed with ab-initio DFT simulations. From the simulation results, it can be concluded that a caffeine monolayer formation with at least three molecules in different chiralities per unit cell is preferred. This hypothesis is in accordance with all recorded measurement data.

In addition to the room temperature study, a structural analysis is performed at low temperatures focusing on submonolayer coverage of caffeine molecules on the Au(111) surface. In monolayer coverage, the quasi-hexagonal order of the caffeine molecules on the gold substrate can be reproduced at low temperatures. Also, it can be shown that more than one molecule is present in the adsorbate unit cell and the three-molecule unit cell hypothesis is strengthened. In contrast to the room temperature STM measurements, it is possible to perform investigations of the submonolayer coverage at low temperatures. There, distinct assemblies of caffeine molecules are found in defined orientation to the substrate. These can be identified as building blocks of chiral motifs on the surface. For higher coverage the transition to the dense quasi-hexagonal monolayer is observable. Thus, the assembled formations of the building blocks disappear and the aforementioned monolayer formation recurs. These results contribute to the understanding of the formation process of caffeine monolayers on crystalline substrates.

Kurzfassung

1,3,7-Trimethylxanthin ($C_8H_{10}N_4O_2$), besser bekannt als Koffein, besitzt eine asymmetrische und achirale Struktur, was bei Adsorption zu zwei Enantiomeren auf der Oberfläche führt. Diese Oberflächenchiralität hat einen Einfluss auf die strukturelle Anordnung der Moleküle auf einem kristallinen Substrat. Die Strukturanalyse von Koffeinmolekülen in mono- und submonomolekularer Bedeckung auf schwach wechselwirkenden Substraten ermöglicht es diesen Einfluss zu untersuchen.

In dieser Arbeit wird die Anordnung von Koffeinmolekülen auf einer Au(111)-Oberfläche mittels Rastertunnelmikroskopie (STM), niederenergetische Elektronenbeugung (LEED), Röntgenphotoelektronenspektroskopie (XPS) und Dichtefunktionaltheorie (DFT)-Berechnungen untersucht. Dafür werden dünne Koffeinfilme mittels Molekularstrahlepitaxie (MBE) im Ultrahochvakuum (UHV) präpariert und zunächst bei Raumtemperatur untersucht. Die Koffeinmoleküle ordnen sich bei monomolekularer Bedeckung in einer quasi-hexagonalen Phase auf Au(111) an. Dabei sind zwei gespiegelte Domänen in Bezug auf die Substratoberfläche in STM und LEED Experimenten messbar. Aus diesen Messungen wird zunächst auf eine periodische Schicht mit nur einem Molekül in der Einheitszelle geschlossen. In durchgeführten XPS-Experimenten wird keine starke Wechselwirkung mit dem Substrat beobachtet. Dies motiviert eine theoretische Analyse der Koffein-Monolagen-Struktur, welche mit ab-initio DFT Simulationen durchgeführt wird. Aus den Ergebnissen der Simulation lässt sich folgern, dass eine Koffein-Monoschicht mit mindestens drei Molekülen in unterschiedlichen Chiralitäten pro Einheitszelle präferiert wird. Diese Hypothese ist kompatibel mit allen aufgenommenen Messdaten.

Zusätzlich zur Untersuchung bei Raumtemperatur erfolgt eine Strukturanalyse bei tiefen Temperaturen mit Fokus auf Submonolagen-Bedeckung der Koffeinmoleküle. In der Monolagen-Bedeckung kann auch bei tiefen Temperaturen die quasi-hexagonale Ordnung der Koffeinmoleküle auf dem Goldsubstrat reproduziert werden. Ebenfalls kann gezeigt werden, dass mehr als ein Molekül in der Adsorbat-Einheitszelle vorhanden ist und die Hypothese der dreimolekularen Einheitszelle wird gestärkt. Im Gegensatz zu den Raumtemperatur STM Messungen gelingt es bei tiefen Temperaturen Untersuchung bei Submonolagen-Bedeckung durchzuführen. Dort werden distinkte Ansammlungen von Koffeinmolekülen in definierter Ausrichtung zum Substrat gefunden. Diese können als Bausteine chiraler Motive auf der Oberfläche identifiziert werden. Im Übergang zur dichten quasi-hexagonalen Monolage geht die Struktur dieser Bausteine verloren und die bekannte Formation stellt sich ein. Diese Ergebnisse tragen zusätzlich zum Verständnis des Formationsprozesses einer Koffein-Monolage bei.

Contents

Chapter 1

Introduction

Studies of organic monolayers have a long history in science, dating back to the beginning of the 20th century. In a remarkable article from 1936 Irving Langmuir describes these two-dimensional films as a real world analogue of the popular novella *"Flatland"* by Edwin A. Abbott published in 1884 [1]. This satirical novella describes the fictional two-dimensional world of Flatland to comment on the hierarchy of Victorian culture, while exploring mathematical dimensions for a larger audience. The idea of changing dimensions is still up-to-date and has its impact on our understanding of physics. Especially, reducing dimensions and possibly complexity is a main driving factor for the study of thin films and surfaces. At that time Langmuir described and measured organic molecules with hydrophilic and hydrophobic ends (fatty acids) in monolayer films at gas-liquid interfaces. These films are comparable to more complex cell membranes, and therefore are a model system for many biological processes. Furthermore, these films can be transferred to solids and are used in the coating industry. They are called Langmuir-Blodgett films, named after him and his collaborator Katharine B. Blodgett, who mainly contributed to the preparation technique [2, 3]. However, there is a striking quote attributed to Nobel laureate Wolfgang Pauli that describes the state of the art for surface exploration in the period during and after World War II:

'God made Solids - But Surfaces were made by the Devil.'
attributed to Wolfgang Pauli [4]

This quote summarizes the difficulties encountered in the experimental study of surfaces. Therefore, only dramatic technological developments could made it possible to further investigate surfaces and thin films. Fortunately, these improvements occurred in the 1960s and 1970s when ultra-high vacuum (UHV) systems became commercially available which allowed the analysis of clean and defined surface structures [5]. Especially, methods utilizing electrons in the energy range from 50 eV to 500 eV with a mean free paths in the order of a few angstroms paved the way to study surfaces and interfaces [6]. The next big step was the invention of the scanning tunneling microscope (STM) in the early 1980s, which made the atomic structure of surfaces accessible in real space. It helped to differentiate between different long range reconstructions, and made the observation of local phenomena possible [7]. With this tool and further understanding of the processes occurring at the surface, a wide range of physical systems could be explored.

The topics of molecular adsorption and supramolecular formations on surfaces have evolved in recent decades. One of the main area of interest has been the self-assembly of deposited organic molecules on surfaces [8]. A step in the development of supramolecular systems on surfaces was the observation of organized domains formed between a biotin derivative and streptavidin [9]. Another observation was the extended surface chirality in the adsorption of the enantiomers of tartaric acid onto copper [10]. Therefore, modern imaging techniques can provide precise structural information about the formation of molecules on metal surfaces. This can be used to study supramolecular organization and heterogeneous catalysis in adsorbed systems [11]. Therefore, self-assembly is a key point for understanding and fabricating nanostructured surfaces, for catalysis, and possibly a way to explore the origin of life [12].

Moreover, the self-assembly of organic molecules on 2D-materials like graphene attracted a lot attention during the last decades. Due to the modification of the electronical properties of graphene by adsorbates it is of particular interest [13, 14]. As electrical devices became smaller and organic electronics came into focus, the study of thin organic electronics was a logical next step. A main focus in the branch of organic electronics was to reduce costs and to apply flexible solutions for modern problems [15]. Most notably is the organic light-emitting diode (OLED) technique, which has conquered the consumer market and increased its share in the global economy [16]. Moreover, in the ongoing climate crisis organic thin films could provide the world with efficient, reusable, and climate friendly solutions and applications in the areas of corrosion protection, surface catalysis, and on surface chemistry [17]. Further developments and applications of surface-dependent processes will benefit from an improved understanding of the structural behavior of a wide variety of materials at the surface and interface [18].

Hence, it is necessary to increase the knowledge about the structural formation of molecular adsorbents on defined surfaces, especially weak interacting species. An interesting model system is the aromatic 1,3,7-trimethylxanthine molecule, better known as caffeine, the most widely used psychoactive drug in the world [19]. The structural formations of these caffeine molecules in thin films have gained interest in recent years. In particular, the preparation of crystalline thin films of caffeine molecules and their structural studies on different substrates have been investigated [20–22]. In addition, the study of the growth process for the defined preparation of organic thin films is of interest. Röthel *et al.* found preferential orientations of caffeine crystals on ionic substrates such as mica, NaCl, and KCl [23]. These formations are interesting and difficult to study because of the intermolecular interactions of caffeine and its asymmetric and achiral structure. Due to this structure caffeine has a prochiral character that leads to two enantiomers on the surface upon adsorption and affects the molecular assembly on a crystalline substrate.

Moreover, due to the dynamically disordered structure and the large unit cell, the determination of these phases has only been achieved recently with x-ray powder diffraction. This shows that the structure determination of polymorphic phases is complex, especially with the undetermined structure of one form. Additionally, polymorphism is a big challenge in pharmacological research and the understanding of the formation process is key for safe and reliable drug development and production. Polymorphism can also occur in organic thin films [24, 25]. The use of caffeine molecules in pharmaceutics is very limited. Nevertheless, it can function as a model system to investigate structural properties and crystallization nuclei for different polymorphs of small, asymmetric, and achiral molecules. Moreover, applications of thin caffeine layers could prevent corrosion [26–28] and enhance the performance of Perovskite solar cells [29]. Furthermore, the molecular adsorption of caffeine on single-walled carbon nanotubes was studied to investigate possible filter or sensor applications of carbon nanotubes [30].

Therefore, a basic research attempt is performed to increase the understanding of the formation of weakly adsorbed molecules. In this work, a bottom-up approach is used for this purpose and a fundamental investigation of the monolayer formation of caffeine is carried out. To investigate the interactions and the influence of on-surface chirality of caffeine, a combined theoretical and experimental approach is used. As a simple and accessible model system, Au(111) is used as a substrate. Therefore, the present work reports on the monolayer formation of caffeine on Au(111) characterized by STM, low-energy electron diffraction (LEED), x-ray photoelectron spectroscopy (XPS), and density functional theory (DFT) calculations.

In order to present the obtained results, this thesis is divided into 8 chapters. The following chapter 2 introduces the adsorbate-substrate system and presents information about the adsorption process in general. Additionally, the concept of on-surface chirality is discussed. Chapter 3 explains the theoretical background of the used experimental methods and provides additional insights to the data processing and its analysis. The different experimental setups utilized in this thesis are described in chapter 4.

Afterwards, the experimental results are presented. In chapter 5 all components necessary for the preparation of the sample surfaces are presented. Furthermore, the preparation of the Au(111) substrate and the deposition process of the organic caffeine film are discussed there. The analysis of the resulting caffeine molecule formations on Au(111) is then divided into two main chapters. Chapter 6 focuses on the analysis of a dense caffeine monolayer formation at room temperature, which is studied by STM, LEED, XPS, and DFT calculations. Derived from these results a structural model is proposed and discussed in comparison to the literature.

In chapter 7, a further investigation of the formation of caffeine molecules on Au(111) is shown at low temperatures. There, the dense monolayer formation is investigated with intra-molecular resolution. In addition, the low-temperature chapter focuses on the study of submonolayer caffeine coverage. Therefore, supramolecular assemblies and chiral motifs of the caffeine molecules on the gold surface are presented. Finally, the chapter 8 summarizes the results, refers to the current scientific context, and concludes with an outlook and suggestions for further studies.

Chapter 2

Background

Starting with background information, this chapter provides fundamentals useful for the further analysis of the adsorbate-substrate system. The first section introduces the caffeine molecule, and its macroscopic and microscopic structural properties. The second section briefly summarizes some concepts of molecular adsorption that are useful for understanding the sample preparation. The third section gives an overview of the gold substrate and its structure.

2.1 Caffeine

The caffeine molecule is a naturally occurring purine base of the xanthine class, more specifically a methylxanthine alkaloid that is chemically related to the adenine and guanine bases of DNA [31]. Due to this chemical similarity caffeine functions as an antagonist of adenosine receptors in the brain [32]. This makes it a psychoactive substance and a stimulant of the human central nervous system [19].

Caffeine has a long tradition in many cultures and is available all over the world with little or no regulation [33]. An ancient Chinese legend says that the emperor Shen Nung first discovered tea in 2437 BC when the wind blew leaves into his boiling water. He was fascinated by the pleasant aroma and invigorated after drinking it [34]. Caffeine has a bitter taste and is an ingredient of many beverages such as coffee, tea, cola soft drinks, or energy drinks [35]. People drink caffeinated beverages to relieve or prevent drowsiness and to improve cognitive performance [31]. Its use correlates with the reduction of diabetes, liver disease, and an overall reduction of mortality [36]. However, the use of caffeine could come with light drug dependence effects like withdrawal symptoms in the form of headache, fatigue, and concentration difficulties [37]. About 85% of the U.S. population, across all age groups, consumes at least one caffeinated beverage per day, with a mean daily caffeine intake of 165 mg per person [38]. For comparison a cup of coffee contains about 29 mg to 176 mg of caffeine [39] and an intake higher than 200 mg can lead to insomnia, nervousness, headache, tachycardia, arrhythmia, and nausea [40]. Nevertheless, due to the effects on the human central nervous system, caffeine is utilized as a treatment for premature infant breathing disorders [41].

Another anecdote has been passed down that Johann Wolfgang von Goethe suggested to the chemist Friedlieb Ferdinand Runge to find the substance in coffee that has such an effect on humans. And in 1819 Runge isolated relatively pure caffeine for the first time [42]. The first synthesis of caffeine from its chemical components was carried out by Hermann Emil Fischer in 1895. Two years later, he derived the structural formula of caffeine as a part of the work for which he was awarded the Nobel Prize in Chemistry in 1902 [43].

Structure

The caffeine molecule or 1,3,7-trimethylxanthine is a xanthine derivative with the molecular structure shown in figure 2.1. The xanthine core of caffeine consists of two fused rings, the pyrimidine core ring with six atoms and the five-atom imidazole ring. All six atoms in the pyrimidine ring are sp^2 hybridized and planar. The imidazole ring is also planar due to its aromatic π-bonding system. This makes all nitrogen atoms in the caffeine molecule coplanar and thus the entire molecule. Attached to the two rings are three methyl groups, two oxygen atoms, and one additional hydrogen atom. In addition, the entire caffeine molecule is aromatic using Hückel's rule, which was further verified by DFT [44].

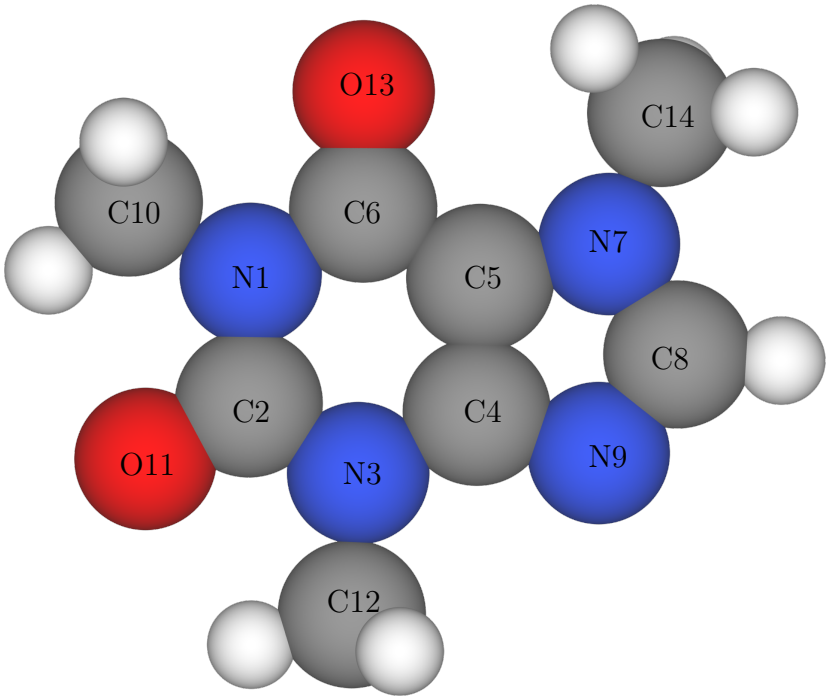

Figure 2.1: Molecular structure of caffeine ($C_8H_{10}N_4O_2$) and assignment of numbers to atoms within the molecule. Carbon (C) atoms are shown in gray, nitrogen (N) in blue, oxygen (O) in red, and hydrogen (H) in white. Representation by VESTA [45].

Pure caffeine is a white, odorless, crystalline powder at room temperature and atmospheric pressure. Three polymorphs and a hydrate of caffeine are currently reported in the literature. The caffeine monohydrate structure was first determined by Sutor (1958) [46]. The three different crystalline phases are the α or I- , β or II-, and γ or III-form, which were further characterized by Derollez *et al.* (2005) [47], Lehmann and Stowasser (2007) [48], and Dichi *et al.* (2014) [49], respectively.

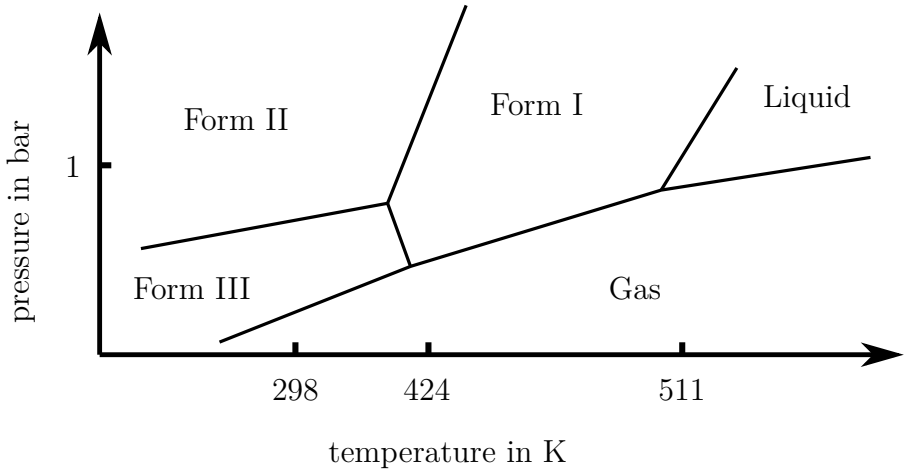

Figure 2.2: Phase diagram of caffeine. Reproduced from Dichi *et al.* [49].

Figure 2.2 shows the phase diagram of the three crystal phases as well as the liquid and gas phases, which was obtained by Dichi *et al.* [49]. The low-temperature phase form II is stable at room temperature and atmospheric pressure and transforms into the high-temperature form I over 141 °C and melts at 236 °C. The reconversion from form I to the form II is kinetically inhibited, so that form I can be metastable at room temperature for weeks [20]. The low-pressure phase form III is obtained at pressures of 1×10^{-5} mbar and room temperature. It is metastable at atmospheric pressure and transforms to form I during heating [49]. The crystal structures of anhydrous caffeine polymorphic phases form I and II are shown in figure 2.3. The structure of form III is currently undetermined, but is expected to be similar to form I [49].

Form I caffeine is a dynamically disordered high-temperature phase that crystallizes in the trigonal space group R3c. The unit cell parameters are: $a, b = 14.937$ Å and $c = 6.898$ Å, resulting in a unit cell volume of $V = 1332$ Å^3 [20]. As shown in figure 2.3 (a) and 2.3 (c) the molecules in this dynamically disordered phase form two nearly hexagonal layers of flat molecules which are stacked on top of each other. At each individual molecule position three preferential orientations rotated around the perpendicular axis of the flat xanthine core of the caffeine molecule were determined [47, 50].

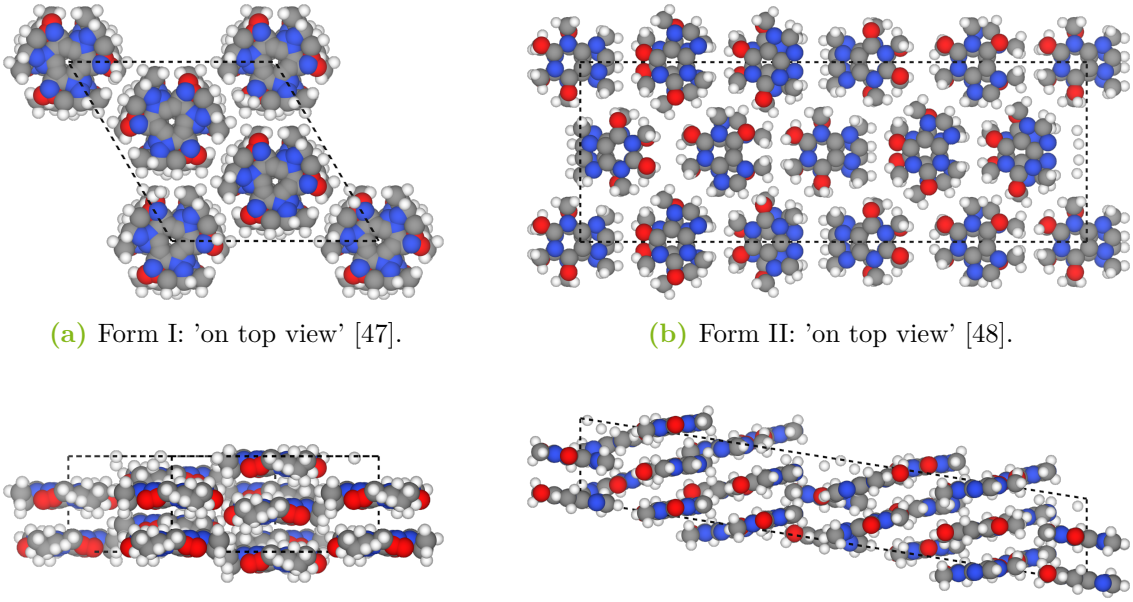

(a) Form I: 'on top view' [47].

(b) Form II: 'on top view' [48].

(c) Form I: 'side view' [47].

(d) Form II: 'side view' [48].

Figure 2.3: Perspective drawings of the caffeine form I and II unit cells determined by Derollez *et al.* [47], and Lehmann and Stowasser [48] in a space-filling depiction, visualized by the VESTA software package [45]. Each unit cell is shown in a 'on top view' and a 'side view' which is 90° rotated around the horizontal axis of the 'on top view'. (a) Form I unit cell which shows the three preferential orientations of the caffeine molecule on each site. (b) Form II unit cell. (c) The molecules are nearly parallel aligned to the hexagonal plane. (d) Formation of molecular stacks parallel to the c axis of form II. The viewing direction is along the b axis.

The room temperature caffeine phase - form II - crystallizes in the monoclinic space group Cc with five crystallographic independent and in sum 20 molecules in the asymmetric unit cell as depicted in figure 2.3 (b). The unit cell parameters are: $a = 43.04\,\text{Å}$, $b = 15.07\,\text{Å}$, $c = 6.95\,\text{Å}$, with an inclination angle of $\beta = 99.03°$, which results in a unit cell volume of $V = 4453\,\text{Å}^3$ [48].

The determination of these phases has only been achieved recently with x-ray powder diffraction. This shows that the structure determination of polymorphic phases is complex, especially with the undetermined structure of form III. This is due to the dynamically disordered structure, the large unit cell of the caffeine structures, and the asymmetry of the caffeine molecule. In addition, the asymmetric and achiral character of the caffeine molecule leads to two on-surface chiralities and this prochiral behavior could have an impact on its monolayer formation [51, 52]. A similar behavior was found for the related xanthine derivative theophylline on Au(111) [53] and theobromine on Au(111) and graphene/SiC(0001) [54].

2.2 Molecular adsorption

Before further investigating the formation of caffeine thin films, this section presents a basic description of molecular adsorption. Adsorption is a surface process and describes the adhesion of atoms, ions or molecules from a gas, liquid or dissolved solid to a surface. In contrast, absorption is a phenomenon of a bulk or volume material in which an absorbent is dissolved. The term desorption describes the reverse process, while sorption includes both processes. The adsorption process is classified depending on the strength of the interaction in chemisorption or physisorption, which are described afterwards [55].

In many cases for UHV applications the desorption is neglected and the rate of adsorption depends just on the pressure of the adsorbate in the residual gas. Therefore, the adsorption could be roughly calculated with kinetic gas theory over the rate of gas molecules colliding with a surface unit area per time. This impinging rate is calculated by:

$$I = \frac{p}{\sqrt{2\pi m k_{\mathrm{B}} T}}, \tag{2.1}$$

There the pressure p, the molecular mass m, the Boltzmann constant k_{B}, and the absolute temperature T are used to express the formula [55].

A further description of the adsorption process from gas particles is the Langmuir adsorption model, which includes desorption. In this model the adsorbate is treated as a ideal gas at isothermal conditions and the adsorption and desorption processes are assumed to be reversible and equal in the equilibrium. Treating all adsorption sites equal, limiting the process to one monolayer, with at most one particle at each adsorption side, the Langmuir equation can be derived and represented by [8]:

$$\theta_A = \frac{K_{\mathrm{eq}}\, p_A}{1 + K_{\mathrm{eq}}\, p_A} \tag{2.2}$$

Here θ_A is the relative occupancy of the adsorption sites and p_A is the partial pressure of the adsorbate. K_{eq} is the associated equilibrium constant, which is the ratio of the adsorption and desorption rate. As shown in equation 2.1 the adsorption rate is $k_{\mathrm{ad}} \propto \frac{1}{\sqrt{2\pi m k_{\mathrm{B}} T}}$. The desorption is described via a temperature-dependent Boltzmann term with $k_{\mathrm{des}} \propto \exp(-E_{\mathrm{ads}})/k_{\mathrm{B}}T$.

The Langmuir adsorption model has its limitations because it neglects multilayer growth, surface roughness, and adsorbate-adsorbate interactions. Nevertheless, it shows that temperature-dependent desorption plays a role that could reduce the coverage.

2.2.1 Physisorption

Physisorption describes the adsorption, in which the adsorbate and the surface remain intact after deposition. Therefore, the electronic structure of the atom or molecule is barely disturbed during physisorption. The fundamental interaction force of physisorption is the Van der Waals force (VdW). It arises from the interaction between induced, permanent or transient electric dipoles [55].

A potential way to model Van der Waals forces is via the Lennard-Jones potential which is often used to model the isotropic part of the total VdW as a function of distance. The Lennard-Jones potential models soft repulsive and attractive interactions and is shown in figure 2.4.

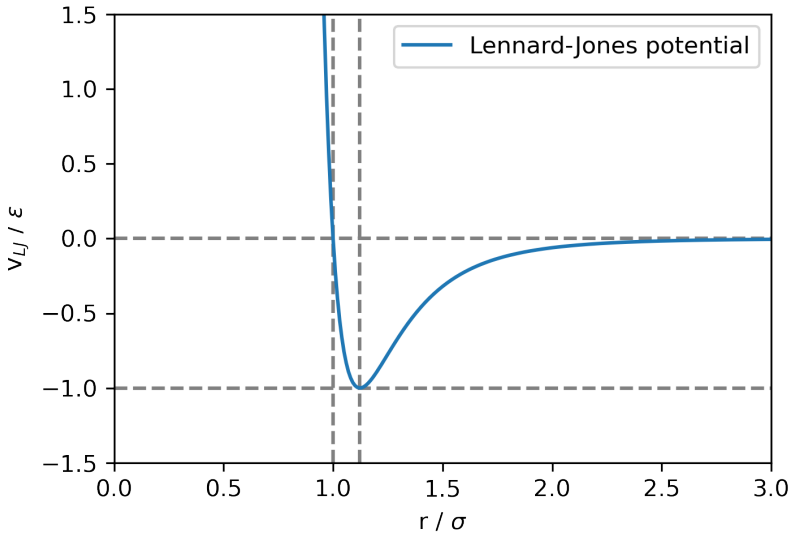

Figure 2.4: Depiction of the Lennard-Jones potential as a function of r in units of σ.

In mathematical terms the Lennard-Jones potential is modeled with:

$$V_{\mathrm{LJ}} = 4\varepsilon \left[\left(\frac{\sigma}{r}\right)^{12} - \left(\frac{\sigma}{r}\right)^{6} \right] = \varepsilon \left[\left(\frac{r_{\mathrm{m}}}{r}\right)^{12} - 2\left(\frac{r_{\mathrm{m}}}{r}\right)^{6} \right] \tag{2.3}$$

Hereby is r the distance between two interacting particles in units of σ, which is the distance at which point the potential V_{LJ} is zero. The minimum is at $r = 2^{1/6}$ where the potential energy is $-\varepsilon$. The repulsive term ($1/r^{12}$ term) describes the Pauli repulsion at short distances of the interacting particles due to overlapping electron orbitals and the attractive term ($1/r^{6}$ term) describes attraction at long ranged interactions, which vanish at infinite distance between two particles. In combination, the Lennard-Jones potential describes electronically neutral atoms or molecules.

An example for physisorped films is the class of long-chain functionalized alkanes [56]. Moreover, flat physisorbed molecules tent to adsorb along their flat side to increase the magnitude of the VdW forces with some degree of rotational freedom [50]. In addition, physisorption is a potential way to storage hydrogen [57]. And recently an example of a bond transition from physisorption to chemisorption of CO molecules was observed [58].

2.2.2 Chemisorption

In contrast to physisorption, chemisorption is an adsorption in which a chemical reaction occurs between the surface and the adsorbate as a result of the adsorption. The reaction induces strong interaction between the adsorbate and the substrate surface and hence creates new types of electronic bonds, which are detectable with sensitive measurements, for example XPS. The binding energy depends on the involved species and is typically in the order of $1 - 10\,\mathrm{eV}$ [55].

Chemisorption allows the formation of long-range ordered surface phases that are very stable. A common example of chemisorption is metal adsorbates on a metal surface, which play a special role in heterogeneous catalysis [59]. A further example of chemisorbed films is the class of self-assembled thiol molecules (RS−H) adsorbed on gold surfaces. Due to the adsorption the thiols form strong Au−SR bonds with the surface and release H_2. The densely packed SR groups protect the surface [60]. Due to the stable structure of caffeine molecules, chemisorption does not play a significant role in this work. But in all molecular adsorbate films, chirality has a great influence on the adsorption structure. Therefore, a short description will be presented in the next section.

2.2.3 On-surface chirality

The geometric property when an object and its mirror image cannot be superimposed is called chirality. The word chirality is derived from the Greek word *kheir*, which means 'hand', since the left and right hands are a basic example of this property. Both hands are mirror images of each other, but incongruent to each other and cannot be brought into coincidence, as shown in figure 2.5 (a) [61]. This concept of chirality is transferable to molecules and is exemplified in figure 2.5.

A chiral molecule and its mirror molecule are called a pair of enantiomers. If the molecule can be superimposed to its mirror molecule, it is called achiral [62]. To distinguish both enantiomers they are commonly labeled with (R) as the abbreviation of the Latin words

rectus for right and (S) *sinister* for left [63]. Furthermore, a distinction is made between homochiral and heterochiral ensembles in which only one or both enantiomers are present, respectively. A heterochiral ensemble with equal amounts of both enantiomers is called a recemic mixture [64].

The first experiment which connected geometric chirality to a measurable property was performed by Louis Pasteur in 1848. He obtained two different types of crystals from tartaric acid solution and showed that these induce opposite rotations in plane-polarized light. Pasteur contributed this effect to a chiral arrangement in the molecular structure [65]. This was later verified and both enantiomers of tataric acid are shown as examples in figure 2.5 (b). The molecules are mirror symmetric but incongruent to each other as the molecule is not flat and therefore are enantiomers.

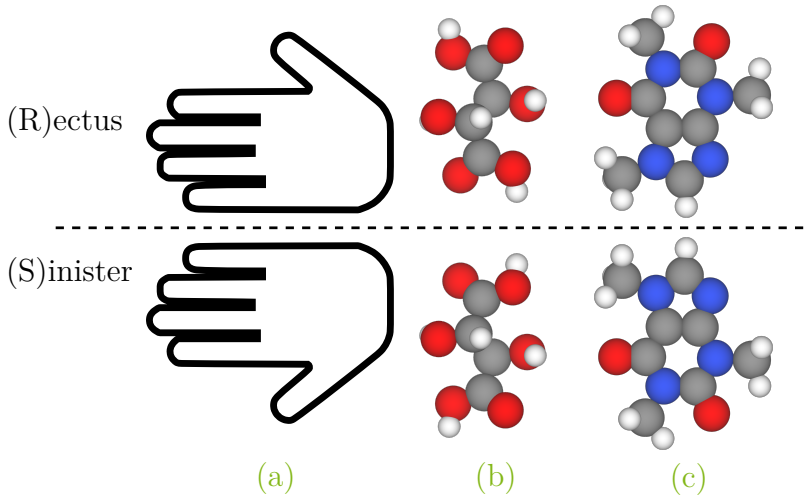

Figure 2.5: Depiction of chiral arrangements mirrored at the dashed horizontal line. (a) A model of a right and left hand, which are a simple representation of a chiral entity. (b) Chiral tartaric acid. (c) Mirrored caffeine molecules.

Additionally, chirality is also a property which can be applied to an adsorbate-substrate system. Due to the lower dimensionality, the mirror-symmetry is often broken at the interface. Achiral molecules that turn chiral due to an interaction, in this case adsorption, are called prochiral [64]. As a third example the caffeine molecule is shown with its mirrored molecule in figure 2.5 (c). It is mirror symmetric but also congruent neglecting the rotation of the individual methyl groups. But due to the broken symmetry at the surface the mirrored molecules are no longer congruent and therefore prochiral. Moreover, four combination of molecules and surfaces in terms of chiral and achiral are possible. Therefore, the field of chiral adsorption covers a wide range and the principles of mirror symmetry breaking were studied [52, 66]

2.3 Gold

This chapter presents a short description and some properties of the gold substrate. Gold is a group 11 element with the atomic number 79 and the element symbol Au (latin *aurum*). It is a transition metal and characterized by its bright yellow color in elemental form and a high electrical conductivity. It is one of the least reactive chemical elements and is solid under standard conditions. Thus, gold occurs in nature in its elemental form, but is relatively rare. Historically, gold is best known as a precious metal, which is used for coins, jewelry and art [67].

The inert behavior results from the d-orbital being completely filled with ten electrons, which is also the basis for the physical classification as precious metal [68]. Due to its inert behavior a gold substrate interacts weakly with adsorbed atoms. This makes gold relatively easy to prepare for surface analysis and allows to study weak interacting molecules like caffeine due to the absence of strong substrate adsorbate interactions.

2.3.1 Crystal structure

Solid gold crystallizes in a face-centered cubic (fcc) lattice with a lattice constant of $a = 408\,\text{pm}$ and four atoms in the unit cell, which is shown in figure 2.6 (a). Every fcc atom has a coordination number of 12. Hence, every gold atom has 12 nearest neighbors at a distance of $a/\sqrt{2} = 288\,\text{pm}$. Depending on the crystal cut different surface planes are realized. These planes are described by their Miller indices (h, k, l).

Miller indices are a triplet of integers describing a family of lattice planes. They are denoted by the reciprocal value of the intersection of the plane with the axes of the lattice vectors of the ideal crystal. The resulting triplet is expended to integers and is then a set of Miller indices (h, k, l) which is a normal vector of the described plane given the native crystal axes. Additionally, the notation $[hkl]$ describes a direction in real space. Negative values are conventionally marked by a bar over the number like in $[\bar{1}00]$.

In figure 2.6 (b) an unreconstructed Au(111) plane is depicted. The resulting surface is a quasi-hexagonal lattice. Though, fcc crystal planes are stacked in an ABC stacking order inducing a three fold symmetry, which can be measured by x-ray or electron diffraction measurements. The symmetry group is 6pmm for the top layer and 3pmm taking all layers into account.

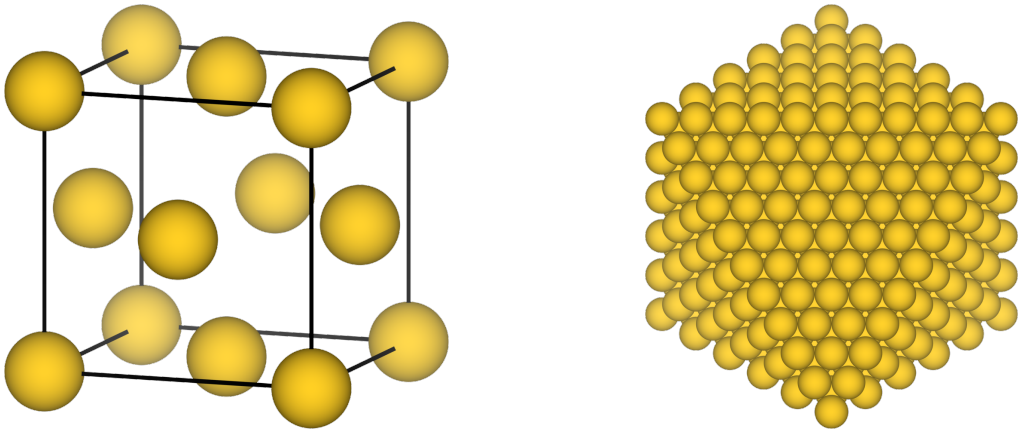

(a) Gold fcc unit cell, a = b = c = 408 pm. (b) Au(111) crystal plane.

Figure 2.6: Illustration of a gold structure model. (a) The bulk unit cell in fcc coordination. (b) A cut through a gold cube of $5 \times 5 \times 5$ unit cells in the 111 plane. Modeled with Vesta [45].

2.3.2 Surface reconstruction

In an ideal crystal, the equilibrium position of each individual atom is determined by minimizing the energy of all other atoms in the crystal, resulting in a periodic structure. At the surface the bonding symmetry is broken, resulting in a redistribution of energy, which changes the atom equilibrium positions. Hence, the surface can differ from the ideal geometry of the bulk crystal, which can be described by relaxation or reconstruction of the topmost layers [59].

Relaxation of the surface refers to a change in the position of the surface atoms relative to the bulk positions, while the bulk unit cell at the surface remains intact. The surface atoms often move in a direction perpendicular to the surface plane, which usually results in a smaller distance between the layers. Sometimes this is compensated by an increased distance in a deeper layer. Some surfaces also experience relaxation in the lateral and in the normal direction, so that the upper layers are shifted relative to the rest to minimize the positional energy.

Surface reconstruction refers to a change of the surface layer relative to the corresponding bulk plane geometry. A reconstruction can affect one or more layers on the surface and can either preserve the total number of atoms in a layer or have more or less atoms than in the corresponding bulk layer. Reconstruction is common with many metal surfaces especially for high Miller index crystals [59]. Usually, fcc (111) planes are the most stable metal surfaces as they have the most nearest neighbors in one plane. Besides platinum, gold is another fcc metal which forms a reconstruction of the (111) surface plane [69–71].

The Au(111) surface exhibits a $(22 \times \sqrt{3})R30°$ reconstruction. The resulting unit cell is rather large and its periodicity and shape was a topic of the scientific discussion for many years [72–77]. In figure 2.7 a model of the $(22 \times \sqrt{3})R30°$ reconstructed Au(111) surface unit cell is shown [76]. The insertion of one gold atom into the $[1\bar{1}0]$-crystal direction every 22 atoms results in 23 Au atoms on 22 lattice places. Hence, this leads to a ∼4 % decreased nearest neighbor distance and different stacking sequences inside the unit cell. The right side of the model in figure 2.7 starts with a fcc stacking order of gold atoms in hollow positions corresponding to an ABCABC stacking sequence. Moving to the left side, the reduced nearest neighbor distance forces the atoms into a bridge position with slightly increased height perpendicular to the surface, resulting in surface buckling. Further to the left, the Au atoms pack in a hexagonal close-packed (hcp) order, reducing the stacking sequence of the four topmost layers to ABAB [77].

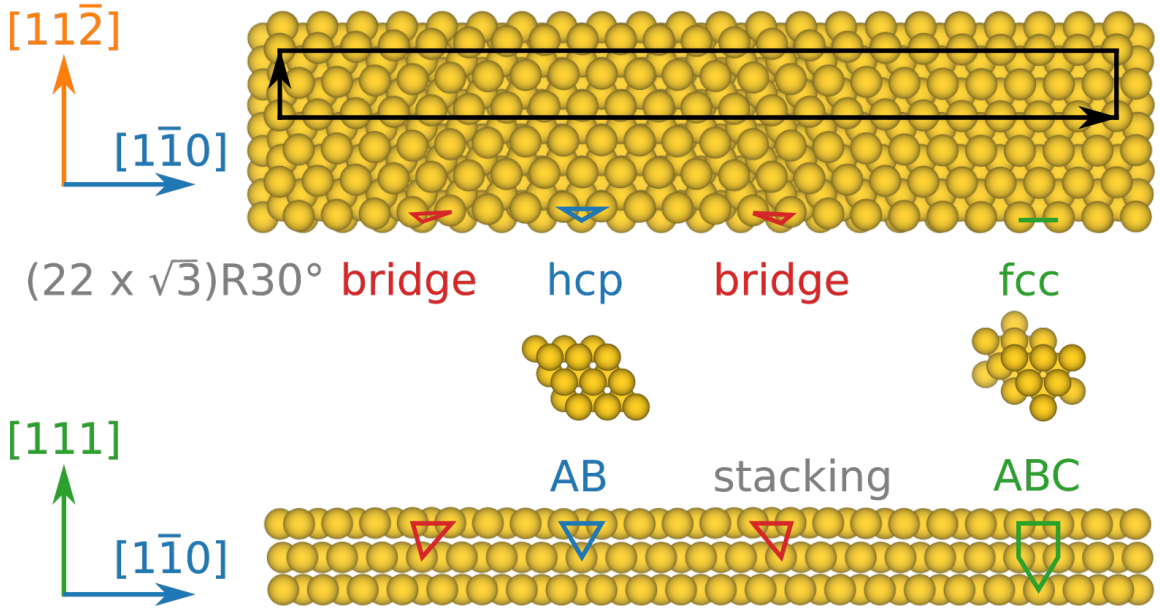

Figure 2.7: Representation of the Au(111) $(22 \times \sqrt{3})R30°$ 'herringbone'-reconstruction after the model of Hanke and Björk [76].

The $(22 \times \sqrt{3})R30°$ reconstruction occurs in three 120° rotated domains, which often switches after about 15 nm inducing a herringbone like zigzag pattern. This explains the commonly used term 'herringbone'-reconstruction referring to this reconstruction. The hcp stacking area in the transition zone between two domains is called 'elbow side' containing one atom with reduced (five) and one with increased (seven) in-plane coordination. Hence, the reaction capability at these 'elbows' is increased and the adsorption process mostly starts there [78].

Chapter 3

Experimental methods

The following chapter contains a description of the surface analysis techniques. The focus is on the scanning tunneling microscope (STM) as a real space imaging tool. Furthermore, low-energy electron diffraction (LEED) is used for structural investigations in k-space. In addition, the x-ray photoelectron spectroscopy (XPS) provides chemical information about the sample. As a complementary analysis method, density functional theory (DFT) simulations are briefly discussed at the end.

3.1 Scanning tunneling microscopy

In 1981, the STM was invented by Binnig and Rohrer at the IBM research facility in Rüschlikon, Switzerland [7, 79, 80]. This microscope utilizes the quantum mechanical tunnel effect to measure the electron density of a conducting surface with spatial resolution. In order to achieve high lateral resolution, the surface is scanned with an atomically sharp tip and its position is recorded by a computer. This invention made it possible to obtain true spatial images of surfaces and adsorbates at atomic resolution. The importance of this invention was recognized only five years later with the 1986 Nobel Prize in physics [81, 82].

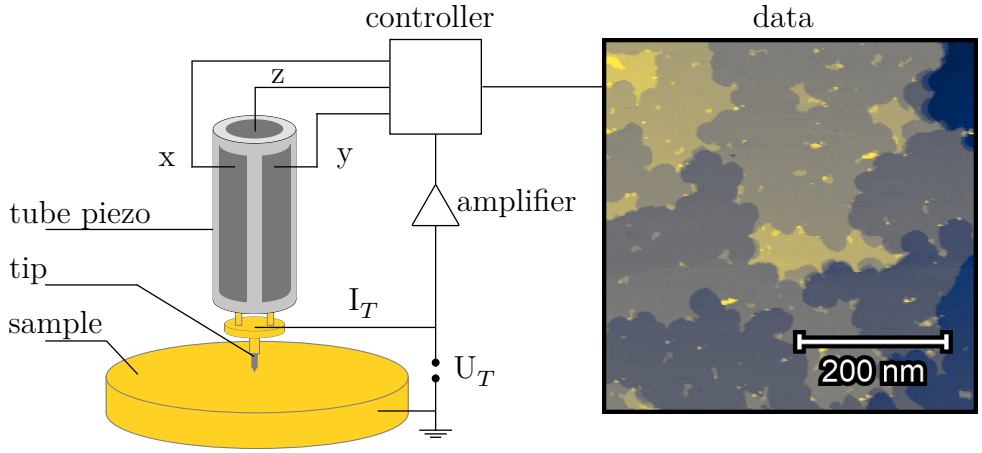

Figure 3.1: Schematic of a simple scanning tunneling microscope. A sample is probed via a sharp tip attached to a tube piezo driven by a controller in the x, y, and z directions. The controller measures the tunnel current and adjusts the bias voltage. Depending on the measurement mode, the data is displayed as a color-coded 2D image.

Figure 3.1 shows a schematic diagram of the basic design of a tunnel microscope. The ideally monoatomic tip is attached to the piezo tube and conducts the tunnel current via the tunnel contact. This current is between 10 pA and 100 nA. To measure this current reliably, it is increased with an amplifier. Afterwards the data is recorded by the computer and the position of the piezo tube is controlled by a feedback loop. For the here used variable temperature scanning tunneling microscope (VT-STM) from *Omicron* the sample is connected to ground potential and the voltage is applied to the tip, which is also controlled by the computer.

3.1.1 Basic principles

In a STM, a sharp and conductive tip is moved so close to a sample that an electrical current flow can be measured. Due to the tunnel effect, some electrons can overcome the vacuum tunnel barrier, which is energetically forbidden according to classical physics. To maintain the current flow, an electrical bias voltage is applied between the tip and the sample. The probability of electrons tunneling through the potential barrier depends on the width and height of the potential barrier. Therefore, the current scales with the distance between tip and sample and is used to image the topography.

In order to move an atomically sharp tip precise and reproducible over the sample, the inverse piezoeffect is utilized. The piezoelectric effect occurs when a variation in expansion causes a change in the electrical polarization in a material. Hence, the inverse piezoelectric effect induces change of the length by applying a voltage. Piezoelectric materials are crystalline materials with no inversion symmetry, for example, quartz (SiO_2) or lead zirconate titanate based ceramics, which are used in modern STMs. With these piezoceramics very precise and small changes in length of less than 0.1 Å can be realized and measured. The expansion can be controlled by applying an external voltage. Two different designs of piezoceramics are used. The first concept was a tripod consisting of three independent piezoceramic stepper-motors, each covering one spatial direction [79]. Later, a scanner was developed consisting of one piezoceramic tube with electrodes located on opposite sides of the tube to control deflection in the x and y directions. The electrode for the z deflection is located inside the tube. This design is used for the experiments in this work. An illustration of such a piezo tube is shown in figure 3.1.

A feedback loop utilizing proportional-integral (PI) controllers is used to avoid collisions between the tip and the sample and to ensure noise suppression. The STM can be operated in two different modes. On one hand the constant current mode, in which the sample is scanned and the height of the tip is adjusted in each step so that the specified current

is kept constant. In this mode, the deflection of the tip is recorded and displayed which is performed by recording the applied voltage to the z-deflection of the piezo tube. On the other hand the constant height mode, which records the position of the piezo and the tunnel current while scanning. Since the feedback loop is suppressed in this mode, the risk of a tip-sample collision is increased. In this mode, the structures can be identified by changes in the tunnel current. In real measurements, both, the height position of the piezo ceramic, and the current flow are recorded, since both modes can only be approximated.

3.1.2 Theoretical description

The tunnel current was first described theoretically in 1928 with the explanation of field emission by Fowler et al. [83] and the α-radiation by Gamow [84] using a one-dimensional tunnel barrier. In principle, a model to describe the scanning tunneling microscope consists

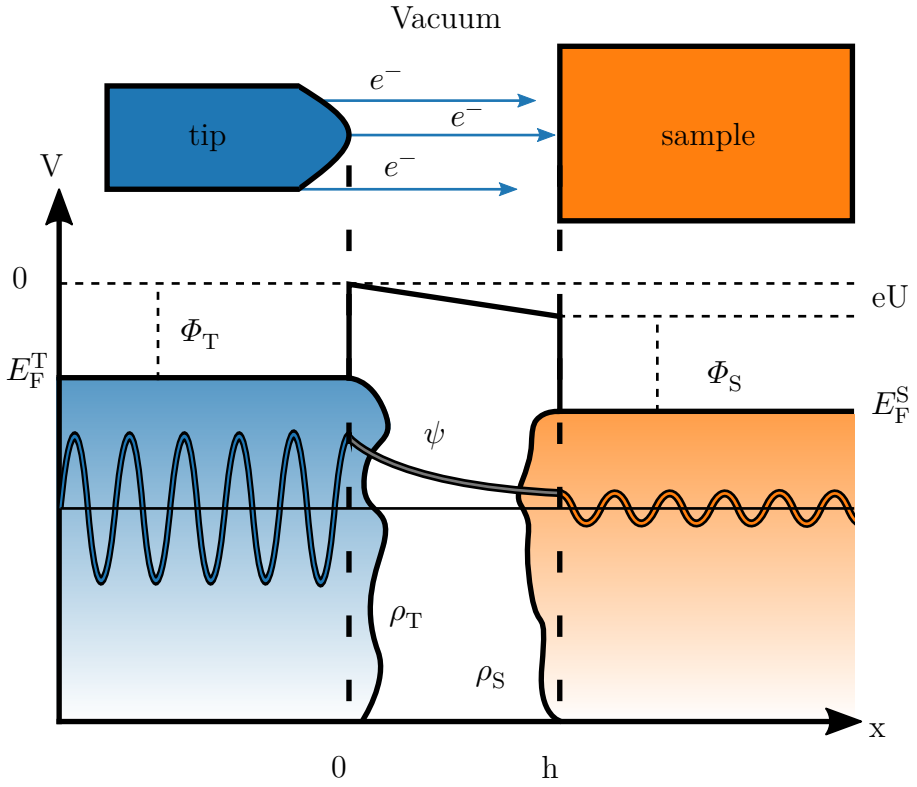

Figure 3.2: Sketch of a 1D vacuum tunnel barrier between a tip and a sample. The Fermi level of the sample is shifted by the applied voltage U. The amplitude wave function of the electrons arriving from the tip side is exponentially decreased on the sample side by the vacuum tunneling barrier. The frequency and thus the energy of the electron has not changed due to the elastic tunneling process. The electron density of states of tip ρ_T and sample ρ_S is sketched and visualized with a color gradient.

of three parts - a tip, the vacuum tunnel barrier, and the sample. In figure 3.2 these three areas are drawn from left to right in a one-dimensional model. On the left side the tip is shown in blue. The area in the center represents the vacuum tunnel barrier, and the sample is indicated on the right side in orange. The Fermi level of the tip $E_{\mathrm{F}}^{\mathrm{T}}$ is indicated and the vacuum potential is set to 0. The Fermi level of the sample $E_{\mathrm{F}}^{\mathrm{S}}$ is shifted by an applied voltage U. Moreover, the work function of the tip Φ_{T} and sample Φ_{S} are shown and the electron density of states of the tip ρ_{T} and sample ρ_{S} are sketched and visualized with a color gradient. The solution of the Schrödinger equation for an electron with the energy E in each of the three regions is indicated with ψ.

To calculate this wave function for an electron in a one-dimensional model, the vacuum tunnel barrier is assumed to be a rectangle with the height V_0. Hence, no voltage is applied and V_0 is an averaged or effective work function. Then the wave function is calculated individually for each area. The electron in the tip (T) is modeled by an incoming plane wave and a wave that is reflected at the work function barrier with the complex reflection coefficient R [85]. Thus the expression for this part of the wave function is

$$\psi_{\mathrm{T}} = A\exp(ikx) + R\exp(-ikx), \tag{3.1}$$

with the wave vector $k = \sqrt{\frac{2m_{\mathrm{e}}E}{\hbar^2}}$, the reduced Planck constant $\hbar$, the electron mass m_{e} and the energy E of the electron. In the vacuum area (V), the wave is described with the approach:

$$\psi_{\mathrm{V}} = A_{\mathrm{V}}\exp(\kappa x) + R_{\mathrm{V}}\exp(-\kappa x) \tag{3.2}$$

Here the decay length is $\kappa = \sqrt{\frac{2m_{\mathrm{e}}(V_0-E)}{\hbar^2}}$ with the vacuum potential height V_0. The wave arriving in the sample (S) is described by:

$$\psi_{\mathrm{S}} = T\exp(ikx) \tag{3.3}$$

with the transmission coefficient T. Using the time-independent Schrödinger equation

$$\left[-\frac{\hbar^2}{2m}\frac{\partial^2}{\partial x^2} + V(x)\right]\psi(x) = E\psi(x) \tag{3.4}$$

and the condition of the continuity of the wave and its dissipation at the edges of the vacuum barrier, the transmission coefficient is given by

$$T(E) = \frac{2k\kappa\exp(-ikh)}{2k\kappa\cosh(\kappa h) - i(k^2-\kappa^2)\sinh(\kappa h)} \tag{3.5}$$

with the width of the vacuum barrier h. Here, the tunnel current is proportional to the square of this coefficient. Assuming a large and wide barrier with $\kappa h \gg 1$ simplifies the expression with $\sinh^2(\kappa h) \approx \frac{1}{4}\exp(2\kappa h)$ [79]:

$$I_\mathrm{T} \propto |T|^2 = \frac{1}{1 + \frac{V_0^2}{4E(V_0-E)}\sinh^2(\kappa h)} \tag{3.6}$$

$$\approx \frac{16E(V_0-E)}{V_0^2}\exp(-2\kappa h) \propto \exp\left(-2\kappa h\right). \tag{3.7}$$

Thus, this simple description of the tunnel current can explain that electrons near the Fermi level can overcome the vacuum tunnel barrier with a probability that depends exponentially on the tip-sample distance. With an applied voltage, the potentials can be shifted relative to each other so that a continuous, directed tunnel current can be maintained.

Bardeen approach

In 1961 Bardeen developed a more general view of the tunneling process for thin insulator layers in superconductors [86]. He used a many-body approach and solved the problem with time-dependent perturbation theory assuming that the interaction of tip and sample is small, which is not always the case [87]. In this concept, the transfer rate ω from an electron state of the tip μ to a sample state ν can be obtained with Fermi's Golden Rule [88]:

$$\omega = \frac{2\pi}{\hbar}\left|M_{\mu\nu}\right|^2 \delta(E_\mu - E_\nu) \tag{3.8}$$

The transition matrix element $M_{\mu\nu}$ describes the transition from the initial state μ to the final state ν. The δ-distribution allows only elastic transitions where the energy of the initial state E_μ is equal to the energy of the final state E_ν and thus represents the conservation of energy. To calculate the tunnel current, all transitions are summed up and multiplied with the electron charge e. The occupation probability for electrons is described by the Fermi-Dirac distribution, where $f(E)$ represents occupied and $[1-f(E)]$ unoccupied states. Taking into account forward and backward tunneling, and a bias voltage U, the tunnel current is given by:

$$I_\mathrm{T} = \frac{2\pi e}{\hbar}\sum_{\mu\nu}\left(f(E_\mu)[1-f(E_\nu+eU)] - f(E_\nu+eU)[1-f(E_\mu)]\right)\left|M_{\mu\nu}\right|^2\delta(E_\mu - E_\nu) \tag{3.9}$$

To determine the matrix element in the Bardeen approach, the Schrödinger equation is solved separately for both sides of the barrier using the Wentzel-Kramers-Brillouin

approximation (WKB approximation). Afterwards, an expression for the matrix element $M_{\mu\nu}$ is found using first-order time-dependent perturbation theory, which leads to the so-called 'Bardeen integral':

$$M_{\mu\nu} = -\frac{\hbar^2}{2m_\mathrm{e}} \int d\vec{S}(\psi_\mu^* \nabla\psi_\nu - \psi_\nu \nabla\psi_\mu^*) \tag{3.10}$$

The integration is performed alongside the separation interface S inside the barrier [86].

Tersoff-Hamann approximation

Based on the Bardeen integral for general tunneling processes, Tersoff and Hamann developed a theory in 1983 to describe the tunnel current of a scanning tunneling microscope [89, 90]. Their theory assumed low voltages ($U \to 0$) and low temperatures ($T \to 0$), which simplified the tunnel current from equation 3.9 to:

$$I_\mathrm{T} = \frac{2\pi e}{\hbar} eU \sum_{\mu\nu} \left|M_{\mu\nu}\right|^2 \delta(E_\mu - E_\mathrm{F})\delta(E_\nu - E_\mathrm{F}) \tag{3.11}$$

At low temperatures, reverse tunneling is omitted and the Fermi-Dirac distribution approaches a step function. The case of small bias voltages considers only tunnel transitions near the Fermi edge with the Fermi energy E_F and is realized by the δ distributions.

To calculate the transition element, sample and tip are again described independently. The sample is modeled with a surface wave function which decays exponentially normal to the surface and has the following shape:

$$\psi_\nu = \frac{1}{\sqrt{\Omega_\mathrm{S}}} \sum_{\vec{G}} a_G \exp\left(-\sqrt{\kappa^2 + \left|\vec{k}_{||} + \vec{G}\right|^2} \cdot z\right) \cdot \exp\left(i\left[\vec{k}_{||} + \vec{G}\right] \cdot \vec{x}\right) \tag{3.12}$$

Where Ω_P is the volume of the sample, $k = \sqrt{\frac{2m_\mathrm{e}\Phi}{\hbar^2}}$ is the decay length into vacuum with the work function Φ, $\vec{k}_{||}$ is the wave vector of the surface-Bloch function and $\vec{G}$ is the reciprocal lattice vector of the surface. For the tip it is assumed that the exponential decay is so strong that only the foremost atom, which is approximated by a spherical s-orbital, plays a role. It is also assumed that the material of tip and sample are identical and therefore the work function Φ is the same. This results in a tip wave function of:

$$\psi_\mu = \frac{1}{\sqrt{\Omega_\mathrm{T}}} c_\mathrm{T} \kappa R \exp(\kappa R) \frac{\exp(-\kappa|\vec{r} - \vec{r_0}|)}{\kappa|\vec{r} - \vec{r_0}|}. \tag{3.13}$$

Where Ω_T is the volume of the tip and c_T is a geometry factor of order 1 for the assumption that $R \gg \kappa^{-1}$. The dimensions of the sample $R, \vec{r_0}$ and d are shown in figure 3.3.

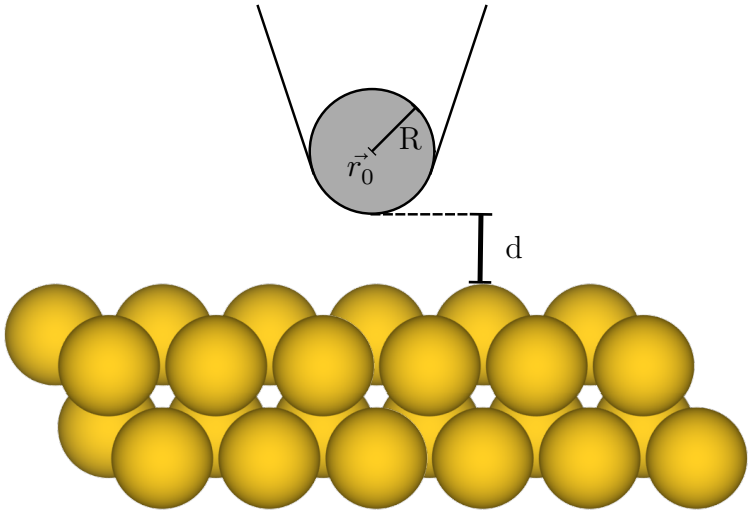

Figure 3.3: Model of a STM tip in the Tersoff-Hamann approximation [89]. The tip consists of a spherical s-orbital with radius R and a distance d between tip and sample surface. Here, the sample is represented by gold atoms of the same size dimension as the tip.

This allows the evaluation of the Bardeen integral and provides an expression for the tunnel current [90]:

$$I_{\mathrm{T}} = 32\frac{\pi^3}{\hbar}e^2 U \Phi^2 \rho_{\mathrm{T}}(E_{\mathrm{F}})\frac{R^2}{\kappa^4}\exp(2kR)\cdot\sum_{\nu}\left|\psi_{\nu}(\vec{r_0})\right|^2\delta(E_{\nu}-E_{\mathrm{F}}) \tag{3.14}$$

Besides the names used above, ρ_{T} is the density of states of the tip at the Fermi level per volume. The sum in equation 3.14 is equivalent to the local density of stated of the sample with $\sum_{\nu}\left|\psi_{\nu}(\vec{r_0})\right|^2\delta(E_{\nu}-E_{\mathrm{F}}) \equiv \rho(\vec{r_0};E_{\mathrm{F}})$. Thus, the STM measures the local density of states at a constant current. This approximation applies only for metallic substrates, a large distance between tip and sample a tip where the s-orbital dominates the density of states.

The assumptions used in the Tersoff and Hamann approach are rarely completely correct in reality. Ohnishi and Tsukada used molecular orbital theory to calculate the conductivity of tungsten clusters of size 4-5 atoms as a tip and showed that the conductivity is mainly given by the d_{z^2} orbital [91]. Chen generalized the approach of Tersoff and Hamann by allowing other active tip orbitals than the s-orbital. Thus, he showed that atomic resolution can be achieved with localized metallic p_z or d_{z^2} tip states [92]. These occur in d-band metals such as platinum, iridium or tungsten. Semiconductors that form p_z orbitals, such as silicon [93], can also be used as a tip material.

In order to optimize the description of the tunnel current, more precise models and assumptions about the investigated substrates are needed. The basics of the perturbation theory approaches have been explained in the previous sections. It should be noted that

in the previous explanations the wave functions are not orthogonal to each other and only small interactions can be described via perturbation theory. Since it is possible to manipulate adsorbates with the tip, a small perturbation of the system is not always present. An extension of this model is the description of the wave functions in a local orbital base using Green's functions and the resulting orthogonality. In 1987 Tuskada and Nobuyuki [94] laid the foundation for the description of tunneling processes using Green's functions. Hence, Hamilton operators for the tip, the sample and for the transition are used and treated separately. Pendry et al. [95] and Todorov et al.[96] utilized this idea and developed a general expression for the tunneling current density j_T with:

$$j_\mathrm{T} = \frac{2\pi e}{\hbar} \int \mathrm{Tr}[\rho_\mathrm{T}^0(E) t^\dagger(E) \rho_\mathrm{S}^0(E) t(E)][f(E) - f(E + eU)] dE \tag{3.15}$$

With the density of states matrix ρ of tip (T) sample (S) and the transition matrix t. Various approximations and types of interaction can be considered here, such as tight binding methods [96], Hückel approximation [97], density functional theory [98], or scattering theory [99].

3.1.3 Experimental implementation

The STM measurements are performed at different facilities using two types of *Omicron* STMs. The measuring tip is always an electrochemically etched tungsten tip, which is further sharpened in-situ. Figure 3.4 (a) shows a scheme of the etching process. A 20 % sodium hydroxide solution (NaOH) is used as etching solvent. A platinum ring cathode is placed at the bottom of a cup and a tungsten wire with a diameter in the range of 100 µm to 200 µm is mounted onto a tip holder utilized as the anode in the etching circuit. The tungsten wire is inserted about 0.8 mm into the etching solution to complete the circuit. When a voltage is applied, the following reactions occur at the air/electrolyte interface [100]:

$$\text{Cathode (Platinium):} \quad 6\,H_2O + 6\,e^- \longrightarrow 3\,H_2(g) + 6\,OH^- \tag{3.16}$$

$$\text{Anode (Tungsten):} \quad W(s) + 8\,OH^- \longrightarrow WO_4^{2-} + 4\,H_2O + 6\,e^- \tag{3.17}$$

Due to the electrochemical etching the tungsten wire shrinks and the electric current declines as the effective wire diameter decreases. When an abrupt current change occurs the controller switches off the current as the change indicate a disruption of the tungsten wire. The tip is then cleaned with distilled water and examined under a light microscope.

In figure 3.4 (b) an example of a successfully etched tip is shown. Due to the contact with the electrolyte and air oxidation occurs at the tip and in-situ sharpening by voltage pulses or electron bombardment is necessary. A further analysis of the etching process and the optimal parameters was performed in the bachelor thesis of L. Stevens [101] and more theoretical insights can be found in the work of T. T. Tsong [102].

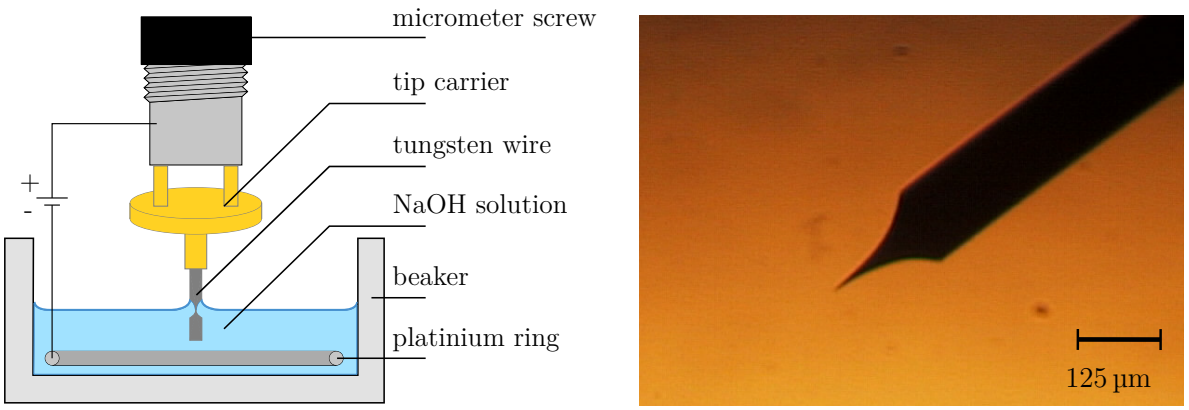

(a) Scheme of the electrochemical tip etching process. **(b)** Light microscopic image of an etched tip.

Figure 3.4: The STM tip etching process. (a) Schematic depiction of the tip etching process. (b) A successfully etched tip of a 125 µm thick tungsten wire.

For each measurement the voltage and current setpoints are adjusted to achieve the best result. Due to the more stable tunneling conditions for low temperature STM measurements, reference series for LT currents and voltages are shown in chapter 7. As shown before this depends on the chemical elements, structure, density of states, and the applied voltage. Therefore, these effects have to be taken into account analyzing absolute height differences in STM. For each STM measurement the size, the applied bias voltage U_{gap}, and additionally for constant current measurements the current setpoint I_{setpoint} is given in short as: $(\text{size}, I_{\text{setpoint}}, U_{\text{gap}})$.

Moreover, it is almost impossible to produce atomically flat surfaces and align them perpendicular to the tip. Therefore, the raw data of STM measurements are more or less two-dimensional tilted planes with small steps modulated on them. In order to detect structures on these gradients, post processing methods like plane subtraction, leveling, and line corrections are necessary. In this thesis the post processing, lattice constant determination, and data visualization of the STM measurements are carried out with the Gwyddion software package [103]. The lattice constants are determined by 2D-fast Fourier transform (FFT), autocorrelation function (ACF), or power spectral density function (PSDF) and averaged across several measurements to minimize the effects of piezo creep and hysteresis. The PSDF is a FFT of the autocorrelation function, that can reveal spots belonging to measured periodicity which can be fitted to estimate the lattice constants

in different directions. This function has proven to be a good approximation for lattice constants measured in two dimensional images [104]. More details about the analysis and interpretation of scanning probe microscopy measurements can be found in the work of P. Klapetek [105]. A systematic uncertainty due to shear or calibration could not be excluded by averaging, therefore the measured lattice constants are cross-checked with LEED measurements, which are explained hereafter.

The colormap 'cividis' is used to display the STM images barrier-free, as it enables an almost identical visual data interpretation for color-blind and non color-blind people. Furthermore, this colormap is perceptually uniform in hue and brightness, and increases in brightness linearly [106]. Therefore, the choice of this colormap ensures the correct representation of linear data sets including the 2D STM measurements which use colormaps to present the measured height or current at each individual position.

3.2 Low-energy electron diffraction

The next experimental method described here is the low-energy electron diffraction (LEED) method. This is a technique in which a conducting periodic sample is irradiated with monoenergetic electrons and the resulting diffraction pattern is analyzed. To obtain a diffraction pattern, the wave properties of the electrons have to be considered. In 1924, de Broglie established a wave theory for particles, analogous to the already proven wave-particle dualism of light [107]. Its validity could be experimentally confirmed in 1927 by the electron scattering experiments of Davisson and Germer on a nickel single crystal [108], and by Thomson on a celluloid film [109]. For these findings, de Broglie received the Nobel Prize in 1929, as did Davisson and Thomson for the experimental proof in 1937 [82].

The strong interaction of the electrons with atoms and the resulting small inelastic mean free path (IMFP) in solids make electrons particularly interesting for surface-sensitive investigations. This relationship is shown by the so called 'universal curve' in figure 3.5. The IMFP of electrons shows a minimum at an electron energy of about 40 eV more or less independent of the element [110]. Adding, that this is only an approximation and several improvements to this description have been made [111]. And especially, for very low kinetic energies the 'universal curve' is not an adequate description [112]. Combining the small information depth and the diffraction ability of low-energy electrons, the diffraction patterns of elastically scattered electrons can be used to determine the geometric structure of atomically periodic surfaces. As a first kinetic approximation, the diffraction pattern is a 2D Fourier transform of the first atomic layer, neglecting several effects [113].

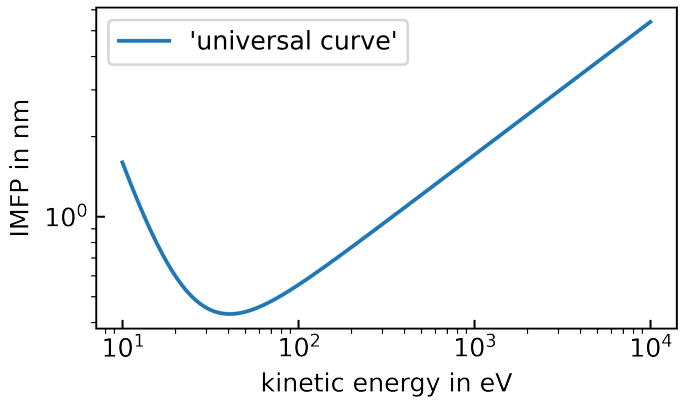

Figure 3.5: Depiction of the inelastic mean free path of electrons in the approximation of IMFP $= \frac{143\,\mathrm{nm\,eV^2}}{E_{\mathrm{kin}}^2} + 0.054\,\mathrm{nm}\sqrt{\mathrm{eV}} \cdot \sqrt{E_{\mathrm{kin}}}$, with E_{kin} in eV [110]. Sometimes this curve is called 'universal curve' in surface science literature.

3.2.1 Basic principles

In LEED, an electrically conductive, grounded sample is irradiated with focused monoenergetic electrons perpendicular to its surface. At the surface, most of the irradiated electrons are absorbed and cannot be used for structure determination. Moreover, most of the backscattered electrons have interacted inelastically with the sample. And since only coherent, elastically scattered electrons can form an interference pattern, the inelastically scattered electrons have to be filtered out. The remaining electrons are made visible by fluorescence on a concentrically arranged fluorescent screen, revealing the diffraction pattern. From this pattern the surface periodicity can be determined. The probing electron energy depends on the periodicity of the structure and is typically in the range of 20 eV to 500 eV, which corresponds to the de Broglie wavelength

$$\lambda = \frac{h}{mv} = \frac{h}{\sqrt{2m_{\mathrm{e}}E_{\mathrm{kin}}}} \tag{3.18}$$

of 0.5 Å to 3 Å. Here, h is the Planck constant, m the mass of the particle, and v its velocity. In addition, m_{e} is the electron mass and E_{kin} is the electron's kinectic energy. The coherence region of the filament typically has a diameter of 100 Å to 200 Å [114], so surface structures must be periodic in this size to show interference. The beam diameter is up to 1 mm wide, so many interaction processes and coherence regions are averaged over a macroscopic range. Therefore, the intensities of the different areas are added up, since they overlap incoherently. Defects and irregular adsorbate structures lead to a higher background noise [115].

3.2.2 Theoretical description

The constructive interference of diffraction of plane waves at a grid, can be described with the Laue condition:

$$\Delta\vec{k} = \vec{k_0} - \vec{k_s} = \vec{G}. \tag{3.19}$$

Here $\vec{k_0}$ is the incident, $\vec{k_s}$ the scattered wave vector, and $\vec{G}$ a reciprocal lattice vector. The breaking of the translational symmetry at the surface leads to the fact that the momentum transfer in vertical direction depends only on the conservation of energy. This reduces the Laue condition at the surface to $\vec{k_{s\parallel}} - \vec{k_{0\parallel}} = \vec{G_{hk}}$. With $\vec{k_{s\parallel}}$ and $\vec{k_{0\parallel}}$ being the components of the incoming and outgoing wave vector parallel to the surface and $\vec{G_{hk}}$ is the reciprocal lattice vector of the surface. Due to the broken translational symmetry at the surface the reciprocal lattice points become reciprocal lattice rods. The Ewald sphere construction in reciprocal space is a simple way to visualize when the Laue condition is fulfilled, and therefore is shown in figure 3.6. The incident wave vector $\vec{k_0}$ generates a sphere and at

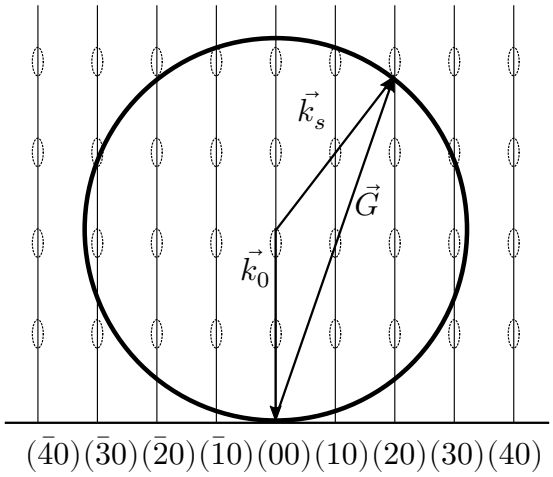

Figure 3.6: A schematic representation of an Ewald sphere in two dimensions. The wave vector of an incident electron is marked with $\vec{k_0}$ and for the scattered electron with $\vec{k_s}$. The reciprocal lattice vector is labeled with $\vec{G}$ [116].

every intersection of the sphere surface with reciprocal lattice rods, the Laue condition is fulfilled and constructive interference occurs in form of a visible reflex. An increase of the kinetic energy of the incident electrons leads to a larger Ewald sphere and thus to more intersections and more reflections on the screen [115]. Due to multiple scattering effects the spot intensity varies and is larger for intersections that are marked as ellipsoids in figure 3.6. Therefore, to fully describe the intensity and energy dependence of the reflexes, multiple scattering methods have to be used, which are described in literature [115, 117].

3.2.3 Experimental implementation

Figure 3.7 shows the basic construction of an electron optics suitable for LEED. In the center of the system is a cathode, that emits electrons, which are accelerated with a defined energy perpendicular onto the sample. Thereafter, a system of electron lenses is build to focus the electron beam. Furthermore, several hemispherical grids are concentrically aligned around the sample to filter out the elastically diffracted electrons. In principle, only two grids are necessary. For a better resolution and less interference, three grids are used as standard. The here used *ErLEED 3000D* system from *SPECS* is equipped with four grids, which also allows Auger electron spectroscopy (AES). The first grid is connected to the sample potential, which usually corresponds to ground potential, to generate a field-free space between the sample and the first grid. The second and third grids are connected and thus the applied voltage functions as a retarding field to filter out the inelastically scattered electrons. This is followed by the grounded fourth grid. The filtered electrons are accelerated by a bias voltage of 5 keV to 7 keV onto the luminescent screen to produce light. There, the diffraction pattern becomes visible when a periodically reconstructed sample surface is probed, and is recorded with a camera [59].

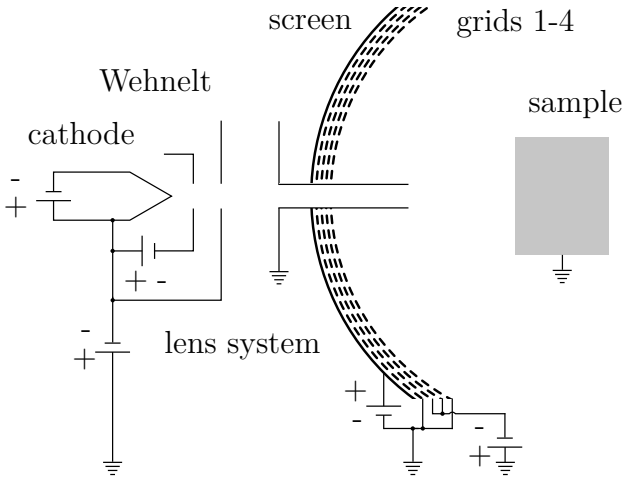

Figure 3.7: Schematic representation of the LEED optics. The cathode acts as an electron gun. The emitted electrons are focused by the Wehnelt and the lens system, and are then directed to the sample. The backscattered electrons are filtered through the grid system and accelerated to the luminescent screen where they are made visible.

The grids are made of molybdenum and coated with gold to avoid potential changes due to differences in work function. The glass luminous screen is coated with transparent and conductive indium tin oxide, which is additionally coated with a phosphor. The phosphor emits photons when electrons with sufficient energy excite it. The cathode is made of a material with a low work function, for example lanthanum hexaboride (LaB_6), thoria

coated iridium, or tungsten. Noting that evaporated molecules could limit the use of the LEED system because they could contaminate the cathode housing and create a locally high pressure that prevents electrons from leaving the housing.

A useful tool to analyze LEED pattern is the LEEDpat program developed by Hermann and van Hove [118]. This simulation program allows to generate LEED patterns for various superstructures on given substrate symmetry groups and a model of the corresponding real space structure. Hence, an easy and fast comparison between measurement data and proposed structure models is possible.

3.3 X-ray photoelectron spectroscopy

To study the chemical composition and bonds of the topmost atomic layers of sample surface, the x-ray photoelectron spectroscopy method can be used, which is based on the photoelectric effect. In order to utilize this effect, an electrically conducting sample is irradiated with monochromatic photons and the emitted photoelectrons are collected by measuring their kinetic energy. Therefore, the photoelectric effect is described in more detail in the following. Thereafter, a brief description of the synchrotron radiation source DELTA, and details about the interpretation of the results are given.

3.3.1 The photoelectric effect

The photoelectric effect describes the emission of photoelectrons when light of sufficient frequency ν interacts with a solid. In 1905 Albert Einstein provided the theoretical description of this effect, for which he was awarded the Nobel Prize in physics in 1921 [82, 119]. Einstein described light as quantized energy, so-called photons, whereby each photon has the energy $E_{\mathrm{ph}} = h\nu$. Here, h corresponds to Planck's constant and ν to the light frequency. When a photon hits an electron bound in a solid, it is absorbed and transfers its entire energy to the electron. If the absorbed energy is higher than the electron binding energy, the electron can be released from the bond, leaving a core-hole. Such an electron is released from the solid if the energy of the incident photon is greater than the sum of the binding energy and the work function. The excess energy is transferred to the photoelectron as kinetic energy E_{kin}. The energy balance of this process is described by the photoelectric equation:

$$E_{\mathrm{kin}} = h\nu - E_{\mathrm{b}} - \Phi_{\mathrm{s}} \tag{3.20}$$

where E_{kin} is the kinetic energy of the photoelectron after leaving the solid, E_b is the binding energy of the electron in the solid and Φ_s is the work function of the sample. Φ_s describes the energy difference between the Fermi energy E_F and the vacuum energy E_{vac}. The binding energy E_b is the energy difference between the Fermi energy E_F and the energy of the orbital in which the electron is bound [120]. The emission of a photoelectron from the solid as a result of the photoelectric effect is shown schematically in figure 3.8. The emitted electrons can then be detected and displayed in a photoelectron spectrum

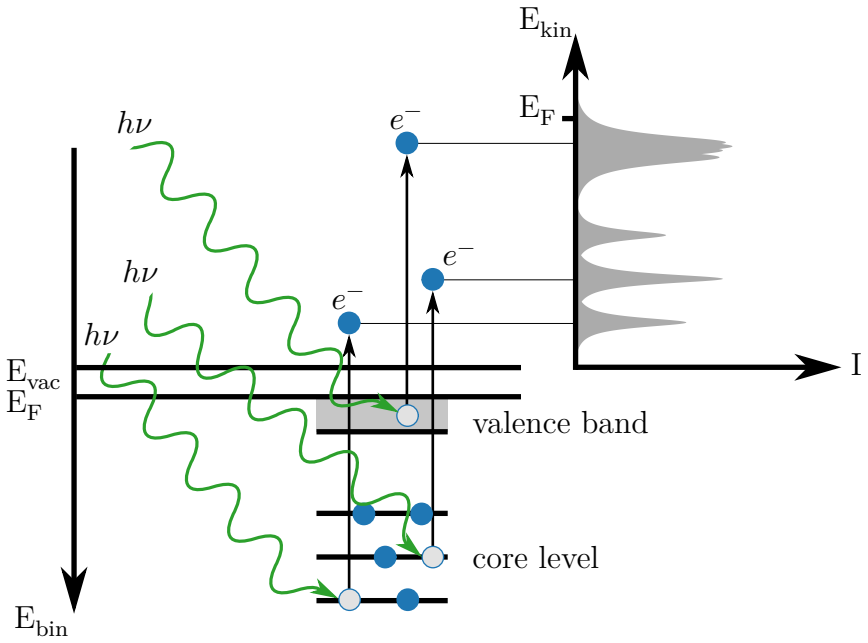

Figure 3.8: Sketch of the photoemission process. The electrons are indicated by blue circles and core-holes by grey circles. On the left side, the sample is irradiated with photons of energy $h\nu$ represented by green waves. Due to the photoelectric effect, some electrons bound in the solid are emitted with a specific kinetic energy. The emitted electrons are then recorded by the analyzer in a photoelectron spectrum, exemplified in the upper right.

similar to the sketched spectrum on the right side of the figure 3.8. Since the kinetic energy of each detected electron depends on its binding energy, the core-levels of the sample can be detected in element-specific core-level peaks. In addition to the core-level peaks, various other lines such as Auger or energy loss peaks can be observed in a photoelectron spectrum. Auger peaks are generated by a relaxation process after the photoemission. Their kinetic energy could overlap with specific core-level peaks. However, since the kinetic energy of the Auger electrons does not depend on the exciting photon energy, shifting the photon energy separates the Auger and core-level peaks. The photoelectrons can also lose energy through non-quantized processes, which lead to a continuous background that increases for lower kinetic energy and make a background correction necessary [55]. As described in section 3.2, electrons interact strongly with a solid which lead to a small

IMFP there. Thus, all detectable electrons come from near the sample surface. This effect can be enhanced by measuring at grazing emission, which effectively increases the path of the electrons through the solid. This increases the absorption probability, resulting in a higher percentage of surface electrons detected by the analyzer. Therefore, measurements at a high emission angle of exemplary $\Phi = 60°$ with respect to the surface normal, are more surface sensitive than measurements at normal emission [121].

Taking a closer look at the specific core-level peaks reveals further insights. A single peak is not measured as an ideal δ-peak due to various broadening phenomena. One is lifetime broadening with a Lorentzian peak shape according to the uncertainty principle. Since the resulting core-hole decays with a certain lifetime, the energy of the emitted photoelectron is thus folded with a Lorentzian. In metals, there is an additional effect because the conduction band allows many different electron-hole pairs to affect the final state, thus smearing the peak toward lower kinetic energies. To compensate this effect, a convolution of a power law and a Lorentzian is used, called the Doniach-Sunjich profile [122]. The asymmetry of the Doniach-Sunjich profile is quantified by an asymmetry parameter α describing the tail to lower kinetic energies. In addition, all experimental influences such as the linewidth of the light source or the resolution of the spectrometer contribute to a Gaussian broadening. The convolution of a Gaussian and a Lorentzian function is called a Voigt profile, which reproduces many core-level signals well.

The core-levels with non-vanishing angular momentum quantum number l split into doublet components due to spin-orbit coupling. Since the total angular momentum $\vec{j}$ is defined as the sum of the orbital angular momentum $\vec{l}$ and the spin $\vec{s}$, the interaction energy depends on the orientation of the projections of the spin and the orbital momenta. Hence, the total angular momentum quantum number is $j = l \pm \frac{1}{2}$ depending on parallel or antiparallel alignment of the momenta [120]. For example, the f orbital splits into the states $f_{5/2}$ and $f_{7/2}$. Each state is degenerate $2j + 1$ times, which thus determines the occupation number of the state. Therefore, the occupation ratio of the $f_{5/2}$ and $f_{7/2}$ states is $3 : 4$, which is also its intensity ratio. Moreover, a higher total angular momentum corresponds to a lower binding energy and thus a higher kinetic energy in a photoelectron spectrum, which is shown later for the Au 4f signal in figure 6.15.

Furthermore, a high-resolution spectrum of a specific core-level provides information about the chemical environment of the studied surface atoms. Each individual atom has a specific binding energy, which is dependent, among other things, on the relative electronegativity of its binding partners. This results in the so-called chemical shift which is measurable with XPS. To illustrate the effect, the reproduced C 1s core-level spectrum of ethyl trifluoroacetate is shown in figure 3.9. Each peak is depicted with a Voigt-profile

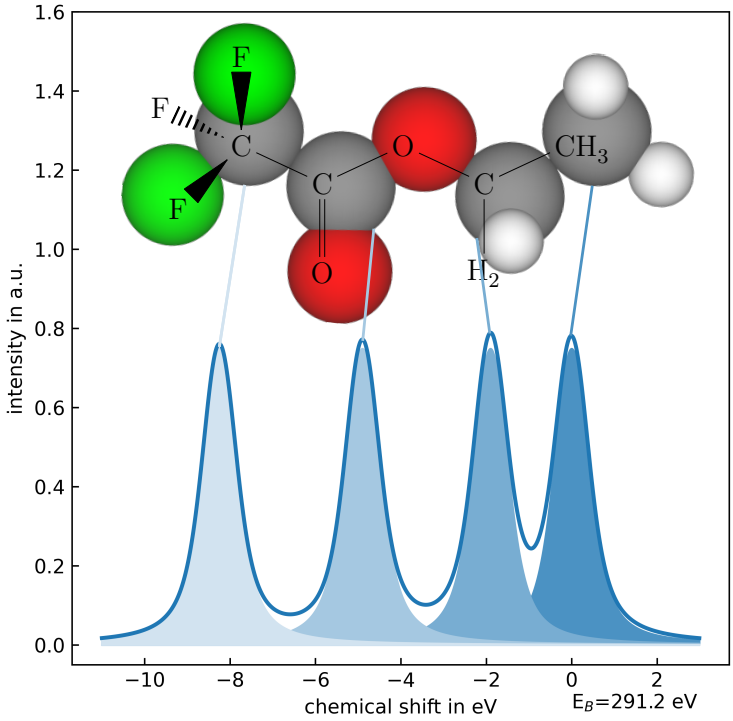

Figure 3.9: Schematic XPS spectrum of ethyl trifluoroacetate, reproduced from [123]. Each peak of the C 1s spectrum is chemically shifted due to the increasing electronegativity of hydrogen, oxygen, and fluorine.

centered at the respective energies taken from [123]. In the spectrum, four chemically shifted components resulting from different chemical environments of the carbon atoms are clearly visible. The relative area of each component in respect to the total intensity of the C 1s spectrum is 25% since there are four carbon atoms in every ethyl trifluoroacetate molecule.

For a quantitative analysis, a peak fitting procedure is carried out for all photoemission spectra in order to precisely determine peak intensities and different chemical bonding environments. The UNIFIT 2017 software package [124] is used since it offers a variety of in-depth XPS analysis procedures, such as applying fit-functions and different background subtractions. A convolution of Doniach-Sunjic and Gauss-functions is applied to all photoelectron spectra [122]. With this line-shape and a Tougaard background, the asymmetric shape of transition metals and metalized elements are well described [125]. Also, for adsorbed molecular spectra, an asymmetric line-shape is common [126].

Synchrotron radiation

The XPS measurements are performed at the light source DELTA which is an electron storage ring in Dortmund. There, experiments with synchrotron radiation can be performed at several beamlines [127]. DELTA is divided into three sections, the schematic structure is shown in figure 3.10. In the linear accelerator (LINAC) and the booster synchrotron (BoDo), electrons from an electron gun are accelerated up to 1.5 GeV. They are then injected into the DELTA storage ring, where they are stored for several hours and emit synchrotron radiation at several beamlines. The different beamlines are equipped with dipole deflection magnets, undulators, or wigglers [128].

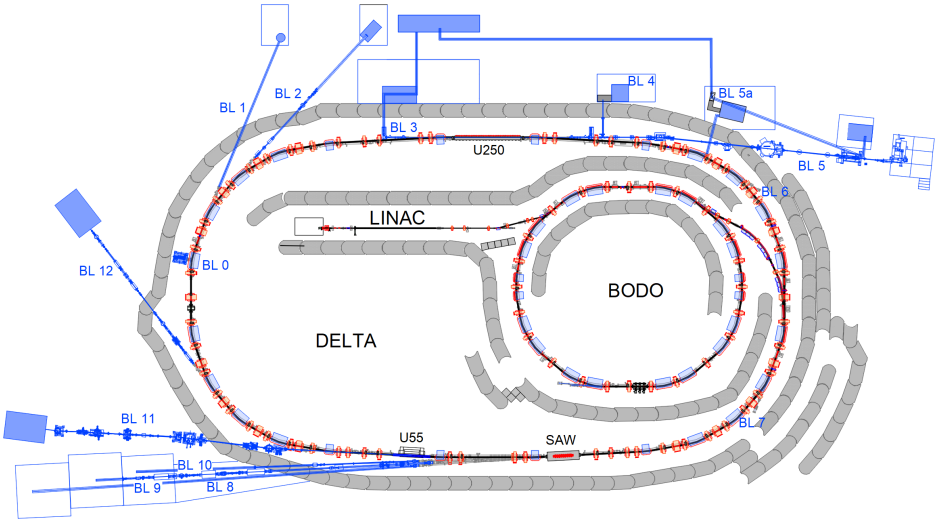

Figure 3.10: A scheme of the DELTA electron storage ring [127]. The experiments presented here are performed at beamline 11 (BL 11), located on the lower left side of the figure.

For the XPS experiments conducted in this work, the plane-grid monochromator beamline 11 is used with the U55 permanent magnet undulator as the radiation source. The U55 consists of an alternating pattern of magnetic north and south poles that force the electrons to follow a sinusoidal path, resulting in linear polarization of the beamline. Depending on the slit width between the undulator poles, the beamline provides photon energies in the range of $h\nu = 55\,\text{eV}$ to $1500\,\text{eV}$ and an energy resolution of $E/\Delta E = 10000$, which can be achieved throughout the energy range. The focused spot size at the sample is $70\,\mu\text{m} \times 30\,\mu\text{m}$ and a typical flux at $h\nu = 400\,\text{eV}$ and $E/\Delta E = 2000$ is about 4×10^{12} photons/s [129]. The kinetic energy of the photoelectrons is measured by an electron spectrometer with a spherical sector analyzer with high precision. After passing through the analyzer, the number of electrons is counted by nine channeltrons that amplify the incoming electrons by several orders of magnitude. The energy spectrum is then recorded by the computer.

3.4 Density functional theory

Finally, a brief introduction to density functional theory (DFT) is given as a complementary method. DFT is a theory describing the electronic structure of many-body systems using functionals. Moreover, DFT-simulations are a computational way to perform an experiment to estimate the structure of a sample system. Therefore, any system of molecules and or solids can be viewed as an ensemble of electrons and nuclei which interact according to electrostatics and quantum mechanics [130]. Hence, these systems can be described by the Schrödinger equation, here shown in the time independent form:

$$\hat{H}|\,\Psi\rangle = [\hat{T}_\mathrm{n} + \hat{T}_\mathrm{e} + \hat{V}_\mathrm{nn} + \hat{V}_\mathrm{ee} + \hat{V}_\mathrm{ne}]\,|\,\Psi\rangle = E|\,\Psi\rangle \tag{3.21}$$

where $\hat{H}$ is the Hamiltonian, E the total energy and Ψ the state vector of the quantum system. The Hamilton operator can be written as the sum of the kinetic energy operator $\hat{T}$ and the potential energy operator $\hat{V}$. The index of each operator represents the nuclei (n) or the electrons (e), and their respective interaction. The calculation of this equation for many nuclei and electrons is complex due to their interactions, hence approximations are necessary. One possible method to calculate these many-electron systems is based on the Born-Oppenheimer approximation, which assumes that the wave functions of the nuclei and electrons can be treated separately, based on the fact that the nuclei are much heavier than the electrons. Therefore, $\hat{T}_\mathrm{n}$ and $\hat{V}_\mathrm{nn}$ can be removed from the Hamiltonian. Furthermore, the equation is transferred to a center of mass system. Since each electron is described by three independent coordinates and depending on the grid, the amount of values needed to store the wave function for an n-electron system increases exponentially.

The theorem of Hohenberg and Kohn can be used to decrease the computational resources and to study the electronic structure of these many-electron systems. It shows, that total energy of a system is completely described by the electron density $\rho(\vec{r})$ of the ground state [131]. With this approach, the properties of many-electron systems can be determined by using energy functionals which have a minimum at $E_\mathrm{min} = E[\rho(\vec{r}_\mathrm{ground})]$. This energy functional is not known a priori. A method developed by Kohn and Sham to solve this problem is to split the kinetic energy term of the functional into two parts, an exact solution for non-interacting particles and a small correction for the kinetic electron correlation [132]. This exchange correlation functional E_xc is the only part that is not known analytically and therefore has to be derived. To solve this problem, various DFT approaches are available that evaluate the electronic structure by different functionals. With these considerations, a cell of a material with n electrons can be studied as a set of n one-electron Schrödinger-like equations, also known as Kohn-Sham (KS) equations [132].

These equations are typically solved numerically in a self-consistent approach, starting from an initial estimate of the electron density. Solving the KS equations then generates a new electron density and thus new KS equations. This iterative procedure is continued until convergence is achieved. A flowchart visualizing this process is shown in figure 3.11.

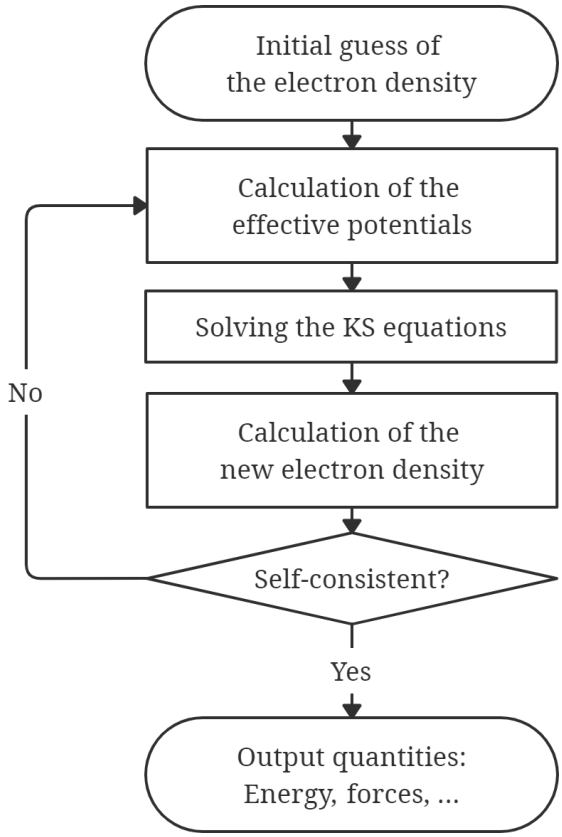

Figure 3.11: Schematic diagram of a self-consistent algorithm to solve the Kohn-Sham (KS) equations. Adapted from [130].

Various methods and ready-made simulation packages are available for solving the Kohn-Sham equations in a self-consistent way. And since an inorganic-organic interface consists of two very different components, the inorganic substrate and the organic adsorbate, the approximations employed have to be adapted to them. In particular, both components show differences in their electronic states, the localization of their valence electron density and their chemical bonds [133]. In addition, long-range dispersion forces are not well described by most functionals and therefore must be treated separately, as they are essential for the description of inorganic-organic interfaces. Here, the long range dispersion forces are accounted for via the TS^{surf} correction [134]. The DFT simulations shown here utilize the FHI-aims package, an all-electron full-potential density functional theory code [135].

Chapter 4

Experimental setup

To perform surface sensitive measurements ultra-high vacuum (UHV) conditions are necessary. This provides minimum of contamination during the study of the surface adsorption of molecules. Therefore, all experiments are carried out in UHV-chambers. Furthermore, a clean and highly ordered surface is necessary as well as highly purified molecules for the deposition process. A brief motivation and description of the UHV chambers and preparation methods is presented in the following sections.

4.1 Ultra-high vacuum

To avoid contamination of the sample during the measurement, the collision rate of gas particles per unit of time and area should be very low. As described in chapter 2.2 the rate of gas molecules colliding with a surface unit area per time is calculated with the formula 2.1 and depends on the residual gas pressure and temperature. As an example at room temperature and a pressure of $p = 1 \times 10^{-9}$ mbar nitrogen N_2, a full nitrogen monolayer is formed in about one hour on each surface. Assuming that the sticking coefficient is 1 and that a monolayer has a surface density of 1×10^{19} molecules/m^2 [55]. Therefore, the residual gas pressure in a UHV chamber should ideally be lower. Normally, UHV means that the sample is subjected to a pressure of less than 1×10^{-8} mbar. The base pressure of the vacuum chambers used in this work is better than 2×10^{-10} mbar. To achieve UHV, the apparatus must be baked out to remove water impurities from the ambient air. Therefore, the experiments are performed in stainless steel or mu-metal chambers that can be heated up to 230 °C. However, some components can only tolerate lower temperatures, so a typical bakeout temperature is about 150 °C.

4.2 Vacuum chambers

Each experiment is located in a vacuum chamber with similar components. To reduce the pressure inside the chambers backing pumps, turbomolecular pumps, ion getter pumps and titanium sublimation pumps are used to remove the residual gas. For the sample preparation, a heating station, a sputter gun, and an evaporator are necessary. The different experimental setups are presented in the following.

4.2.1 VT-STM chamber

The main parts of the experiments are carried out at the variable temperature scanning tunneling microscope (VT-STM)-chamber located at the TU Dortmund Experimental Physics I lab. This setup is shown in figure 4.1 and is divided into two chambers separated by a valve. One is the preparation chamber on the left side and the other one is the measuring section on the right side with the VT-STM. Both chambers are equipped with independent pumping stages to ensure parallel operation. A turbomolecular pump is connected to the preparation chamber and an ion getter pump with a titanium sublimation pump is connected to the STM part. While the separation valve is open, samples can be transferred between both chambers with a sample transfer located on the left side of figure 4.1.

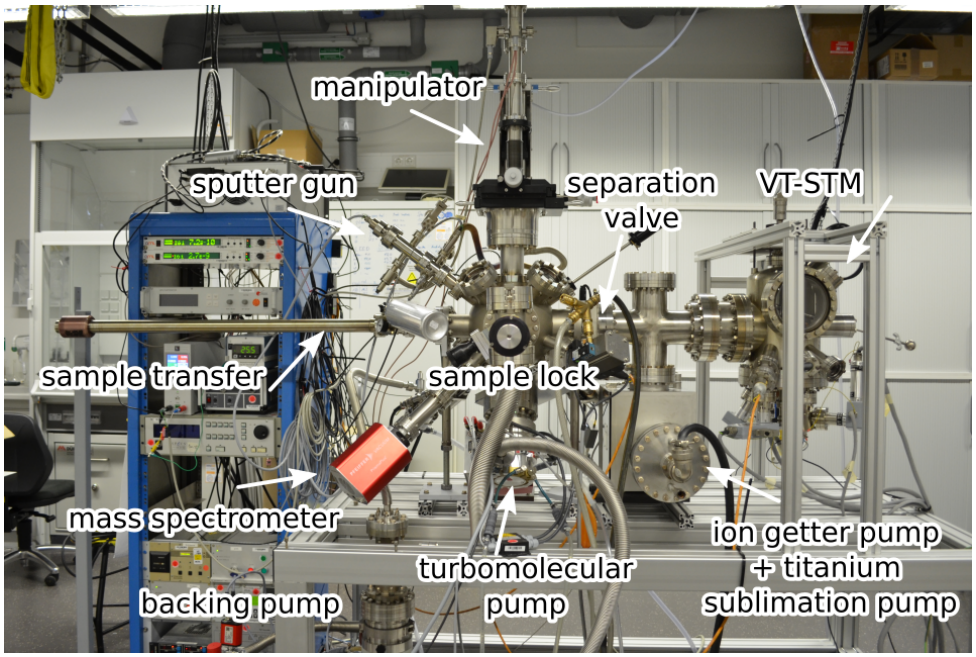

Figure 4.1: The VT-STM chamber in the laboratory facility of the Experimental Physics I group of the TU Dortmund University. On the left side is the preparation chamber, separated by a valve from the STM measuring part on the right side. Photography by J. A. Hochhaus.

The VT-STM allows to examine samples in a temperature range of 25 K to 1000 K. For this purpose, the measuring tip is kept at room temperature and the sample can be cooled or heated so that theoretically temperature-dependent effects can be investigated. Cooling is provided by a liquid helium (LHe) flow cryostat which can also be operated with liquid nitrogen (LN_2). In practice, temperature changes increase the noise level, making it difficult to study these effects. In order to minimize vibration, the STM is built into an eddy current brake and an air damping system is attached to the experiment table.

In addition, the turbomolecular pump is connected to another separation valve and can thus be switched off to minimize vibrations during STM measurements. Therefore, the chamber is only pumped by the vibration-free ion getter pump during the measurement.

In the preparation chamber, a *TRANSAX* manipulator with resistive and direct current sample heating up to 1300 K is available. Additionally, the samples can be cooled down to 160 K and analyzed with a LEED system located at the back of the preparation chamber shown in figure 4.1. Moreover, the chemical composition of the samples can be investigated using AES, which is integrated into the LEED system. Furthermore, the preparation chamber is equipped with a sample lock system, allowing the simultaneous insertion of up to three samples. Samples can be cleaned in situ with a *IQE12/38* ion source from *SPECS* and coated by molecular-beam epitaxy (MBE) or physical vapor deposition (PVD) with different evaporators. The evaporator flange is located between the LEED system and the ion source to ensure that the LEED system is not accidentally coated. Furthermore, the evaporator flange is equipped with a manual valve that allows evaporator changes without breaking the vacuum. Re-evacuation is achieved via a flange connection to the sample lock system with its pumping stages. In addition, a *QO 40A1* quartz crystal microbalance (QCM) from *PREVAC* is mounted on the other side of the LEED system to monitor the deposition process. Furthermore, the residual gas can be analyzed by a *PrismaPlus* quadrupole mass spectrometer (QMS) from *Pfeiffer Vacuum*.

Manipulator

In the course of this project a new 5-axis dual bellow *TRANSAX* manipulator was commissioned by *VACGEN* to improve the handling and preparation of UHV samples in the VT-STM chamber. It allows reproducible sample positioning with a z-travel of 150 mm and a radial travel of ± 12.5 mm in the xy-plane with an accuracy of 0.5 µm. Two independent rotational axis are available, one primary rotation with $\Theta = \pm 180°$ around the z-axis, and the secondary rotation with $\Phi = \pm 120°$ around the sample normal axis.

The manipulator has a DN100CF base flange and the default sample position of $z = 100$ mm is designed to be in the center of a UHV chamber with radius 10 inch (254 mm) in order to maximize compatibility. As shown in figure 4.1, the *TRANSAX* manipulator is mounted on top of the spherical preparation chamber. The preparation chamber has a radius of 5 inch, hence a 5 inch (127 mm) extension tube is mounted between chamber and manipulator. In figure 4.2 (a) the *TRANSAX*-manipulator is shown before first use. An additional feature is that two extension tubes between the feedthrough chamber and the bellow of the z slide are present. The upper tube can be replaced by a differentially pumped rotary

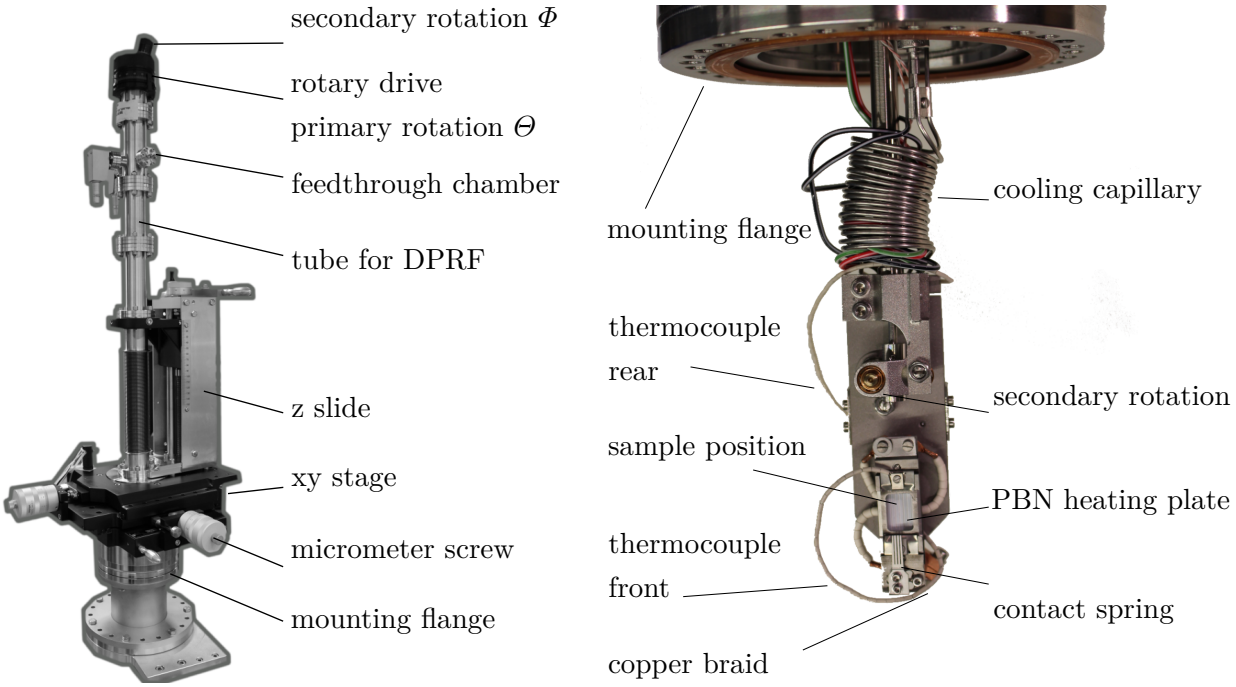

(a) *TRANSAX* manipulator.

(b) Manipulator head with sample station.

Figure 4.2: *TRANSAX* manipulator. (a) full view of the atmospheric side of the manipulator. (b) front view of the manipulator head with sample position on top of the PBN heating plate.

feedthrough (DPRF) with an overall height of 104 mm. This creates the possibility for endless rotation along the z-axis not limited by the connections in situ. The lower tube ensures this unrestricted rotation with the z-stroke retracted.

The sample station located at the manipulator head is shown in figure 4.2 (b). There, samples could be analyzed and prepared on an omicron flag style sample plate in the temperature range from 160 K to 1300 K. Cooling is provided by a flow of cold nitrogen gas through the cooling capillary, which is connected to the sample holder by a copper braid. Elevated temperatures are achieved via resistive heating or direct current heating. Resistive heating can be provided by the integrated pyrolytic boron nitride (PBN) plate directly under the sample position. Direct current heating through the sample can be achieved via the contact spring. The sample temperature is measured by two N-type thermocouples calibrated by the manufacturer, one at the front and one at the rear of the sample station. Additionally, the temperature is monitored by a *IGA 6/23* pyrometer, which allows to reproduce preparation temperatures at different chambers. The type N thermocouples have a very low permeability, which ensures little to no effects on the LEED measurements. Details about the explicit sample preparation are provided in chapter 5.

4.2.2 DELTA chamber

Another experimental setup is located at beamline 11 of the DELTA electron storage ring of the TU Dortmund University center for synchrotron radiation. This setup consists of a large main UHV chamber made of mu-metal, which contains the preparation and measuring equipment as well as an additional sample lock. The chamber is the workstation of beamline 11 and thus connected to the synchrotron, allowing monochromatic synchrotron photons to be focused on the sample through the connecting flange. The electron analyzer is a *CLAM IV* electron spectrometer from *VG Microtech*. Moreover, a powerful 5-axis manipulator is attached to the chamber which is motorized and provides endless rotation in polar (Φ) and azimuthal (Θ) rotation and sufficient linear movement in x-, y-, and z-direction. Thus, any point on the hemisphere above the sample surface can be analyzed. Therefore, this chamber provides the possibility of XPS and x-ray photoelectron diffraction (XPD) measurements. In addition to sample movement and rotation, three contacting

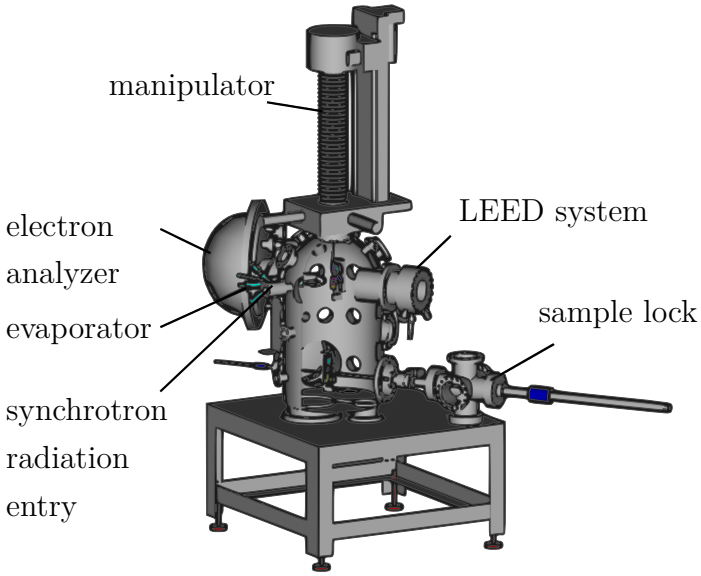

Figure 4.3: Technical drawing of the beamline 11 UHV chamber located at the DELTA electron storage ring of the TU Dortmund University center for synchrotron radiation [136].

options are provided via sliding contacts for a special three-layer sample holder. These contacts allow sample heating via resistive or direct current heating. For resistive heating, a tungsten filament is mounted inside the sample holder right under the sample. With direct current heating, the sample is mounted between two half shells that conduct the current through the sample. The sample temperature is monitored during preparation by a *IGA 6/23* pyrometer. A sputter gun, evaporator flange, and LEED system are also attached to enable the sample preparation. The base pressure is better than 2×10^{-11} mbar.

4.2.3 Nano-Spintronics-Cluster-Tool

A further series of measurements is conducted at the Nano-Spintronics-Cluster-Tool (NSCT) of the Peter Grünberg Institute for Electronic Properties (PGI-6) located at the Jülich Research Centre. The NSCT is shown in figure 4.4 and combines a multitude of complementary analytical methods in one UHV environment. The NSCT can be divided into two main parts each consisting of different UHV chambers. One part is the *Gemini* chamber which accommodates a high-resolution scanning electron microscope (SEM) with an electron spin polarized detector (SEMPA) and a focused ion beam (FIB) unit for defined surface etching.

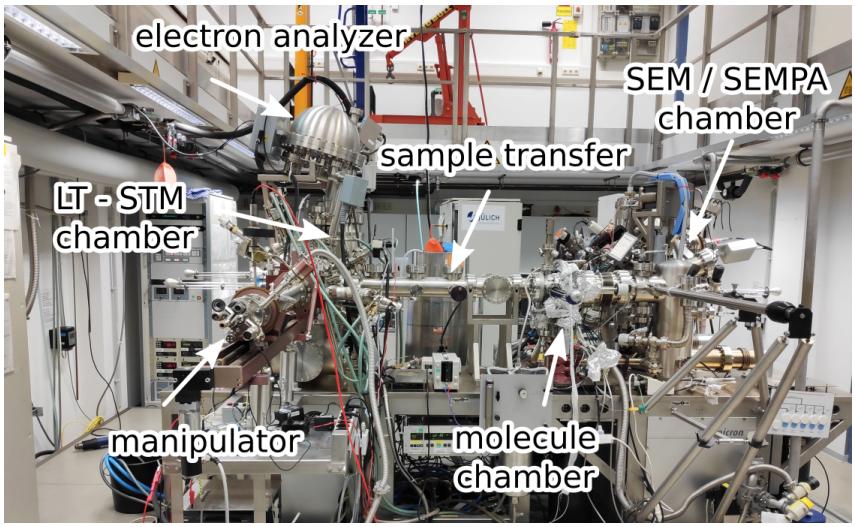

Figure 4.4: Nano-spinelectronic cluster tool of the Peter Grünberg Institute for Electronic Properties *(PGI-6)* located at the Jülich Research Centre.

The other part consists of a preparation chamber, an additional molecule evaporation chamber, and a STM chamber which is connected to the preparation chamber. A sputter gun, several evaporators, a heating station in the manipulator and a separate heating station are available for sample preparation. A LEED system, a X-ray tube, and an electron analyzer for AES and XPS are available for further sample analysis. The STM chamber accommodates a low temperature scanning tunneling microscope (LT-STM) from *Omicron* used for this work. The LT-STM offers the possibility to investigate samples cooled down to about 4 K. This reduces thermal noise and increases the measurement stability, which also increases the resolution. Cooling is accomplished with a LHe bath cryostat, which has a shielding filled with LN_2. The STM is operated with an electrochemically etched tungsten tip which is processed in situ by electron bombardment, repeated voltage pulses, and controlled sample crashes, dependent on the tip condition. The results obtained at this facility are presented in chapter 7.

Chapter 5

Sample preparation

This chapter presents the standard preparation process of a dense monolayer formation of caffeine molecules on a Au(111) single crystal surface. For this reason, the chapter is divided into two parts, starting with the Au(111) substrate preparation, followed by the caffeine adsorbate deposition.

5.1 Substrate preparation

The preparation of the sample system is performed in-situ in each chamber. The Au(111) substrate is obtained from *MaTecK* with a purity of 99.999 %. Figure 5.1 shows a depiction of a Au(111) crystal on a typical flag style sample plate. The metal crystals are mounted with two clamping bars, which are fastened to the base plate with four M1.2 slotted screws. The screws and sample plate are typically made of austenitic stainless steel or molybdenum to resist high temperatures and reduce potential magnetic interference.

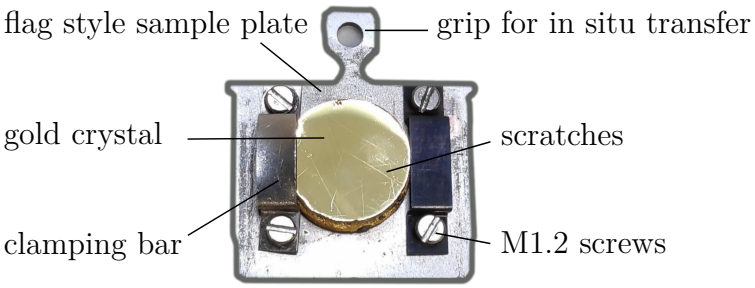

Figure 5.1: Depiction of a gold crystal mounted on a flag style sample plate. Slight scratches due to the polish process are visible.

In order to prepare a clean, reconstructed single-crystal metal surface, typically repeated sputtering and annealing cycles are performed. For the Au(111) crystal, a standard cycle includes 15 min sputtering and 40 min annealing. This varies for different elements or crystal surface orientations. Since several cycles are necessary to obtain a well-ordered sample, the preparation process is automated via a self-written *LabView* program. The program was further developed by J. A. Hochhaus in his bachelor thesis [137]. For the sputtering process, the *IQE 12/38* ion source with 5.0 argon gas is used. The Ar^+ ions are focused on the sample with a kinetic energy of $E_{kin} = 800\,eV$ and an angle of incidence of $\Theta = 45°$ for $\sim 10\,min$. The argon background pressure is about $5 \times 10^{-7}\,mbar$ which

corresponds to an ion current of about $\sim 25\,\mu A$ measured at the sputter gun. The sputtering process is followed by an annealing step in which the sample is heated up to $T \sim 700\,°C$ by resistive heating.

To estimate the sample temperature a *IGA 6/23* pyrometer with an emissivity of 5 % - the lowest adjustable setting - is used, which is calibrated by a reference measurement with a K-type thermocouple spot-welded to a test gold crystal. For the *TRANSAX* manipulator the supplied N-type thermocouples are calibrated by the manufacturer and are then matched with the pyrometer results. A further analysis of preparation parameters for different gold crystals at the VT-STM chamber was performed in the bachelor thesis of J. A. Hochhaus [137] and a further analysis of the *TRANSAX* manipulator preparation parameters was conducted in the bachelor thesis of S. Hilgers [138]. These results are used to obtain highly ordered substrate crystals.

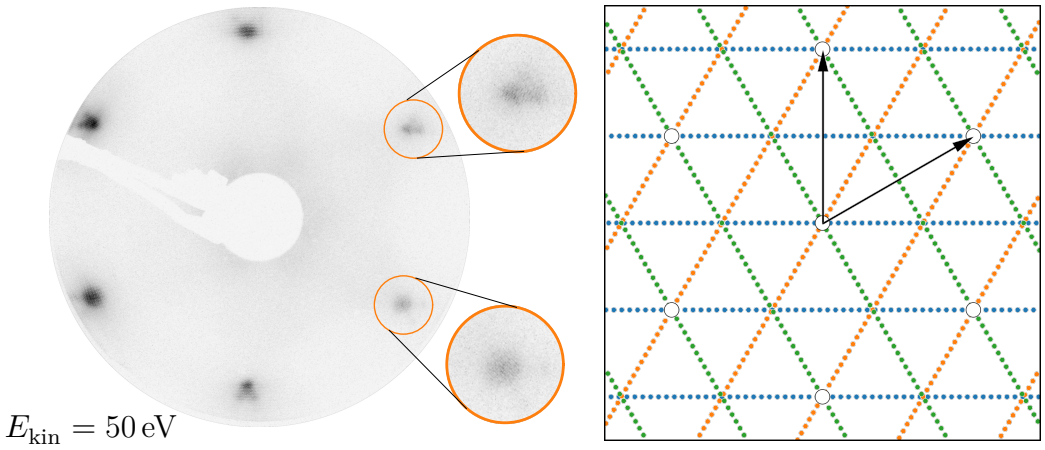

(a) LEED image of clean Au(111).

(b) LEEDpat simulation of Au(111) [118].

Figure 5.2: Clean Au(111) surface with $(22 \times \sqrt{3})R30°$ reconstruction visible. (a) LEED measurement of a clean substrate. Splitting of the first order bulk diffraction spots is visible due to surface reconstruction. (b) Simulated LEED pattern showing theoretically possible reconstruction spots.

To ensure successful preparation of the Au(111) surface, its surface periodicity is typically checked with a LEED measurement. One example of a successful substrate preparation is shown in figure 5.2 (a). The LEED image shows six main spots of the quasi-hexagonal Au(111) surface with fine structure visible around each spot. These spots are an indication of a successful preparation as they result from the long range $(22 \times \sqrt{3})R30°$ 'herringbone' reconstruction. In comparison, figure 5.2 (b) shows all possible spot positions of the $(22 \times \sqrt{3})R30°$ reconstruction in respect to the threefold main spots of the Au(111) substrate represented with LEEDpat [118, 139].

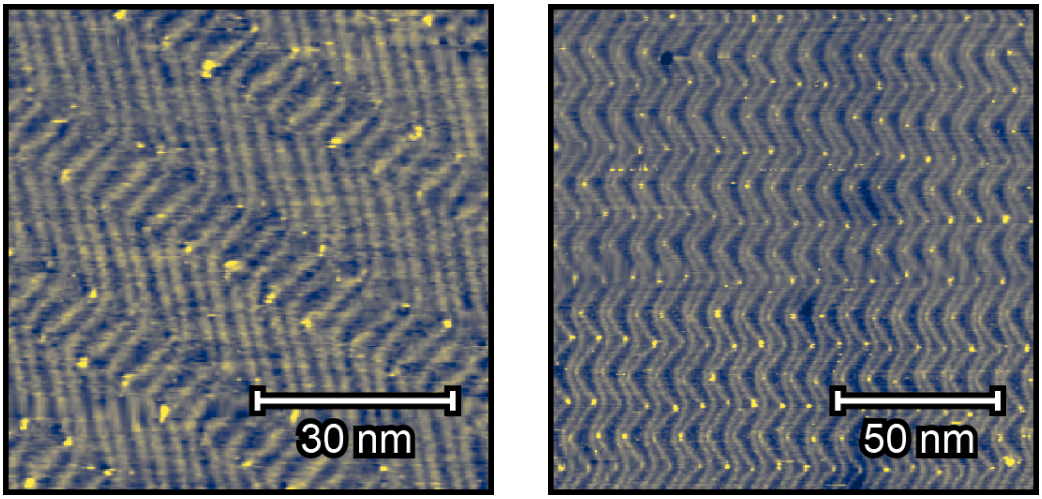

(a) RT STM - clean Au(111) surface (b) LT STM - clean Au(111) surface

Figure 5.3: STM images of pristine and reconstructed Au(111) surfaces measured at room temperature (5.3 (a)) and at 4 K (5.3 (b)). (a) (97×97 nm, 100 pA, -0.7 V). (b) (150×150 nm, 80 pA, 0.5 V).

With the successful LEED experiment indicating a clean and well reconstructed surface, STM measurements on the clean Au(111) are conducted to validate these results. In figure 5.3 two STM images obtained at two different chambers are shown. In both measurements the long range periodicity is demonstrated. The experiment at room temperature is shown in figure 5.3 (a) and at low temperatures in figure 5.3 (b), respectively. The 'herringbone' domains alternating by 120° are clearly visible, as described in chapter 2.3.2. Moreover, the resolution and noise level are better for the low temperature measurement, showing the strength of a LT-STM. In the next section, the preparation of thin caffeine molecule layers on the gold substrate is discussed.

5.2 Caffeine deposition

Evaporating organic molecules in UHV requires the evaporating substance in sufficient purity, a suitable evaporator, and a controlled evaporation process. Anhydrous caffeine powder with a purity $> 99\,\%$ is commercially available and is purchased from *Sigma-Aldrich* which is used in this study. The utilized evaporator is a triple Knudsen cell evaporator from *KENTAX*, which was designed by C. Seidel especially for organic substances [140].

The Knudsen cell is shown in figure 5.4 and consists of three independent evaporation positions. Every position can accommodate one quartz glass crucible with a typical filling of 10 mg of organic powder and is temperature controlled in the range from 30 °C to

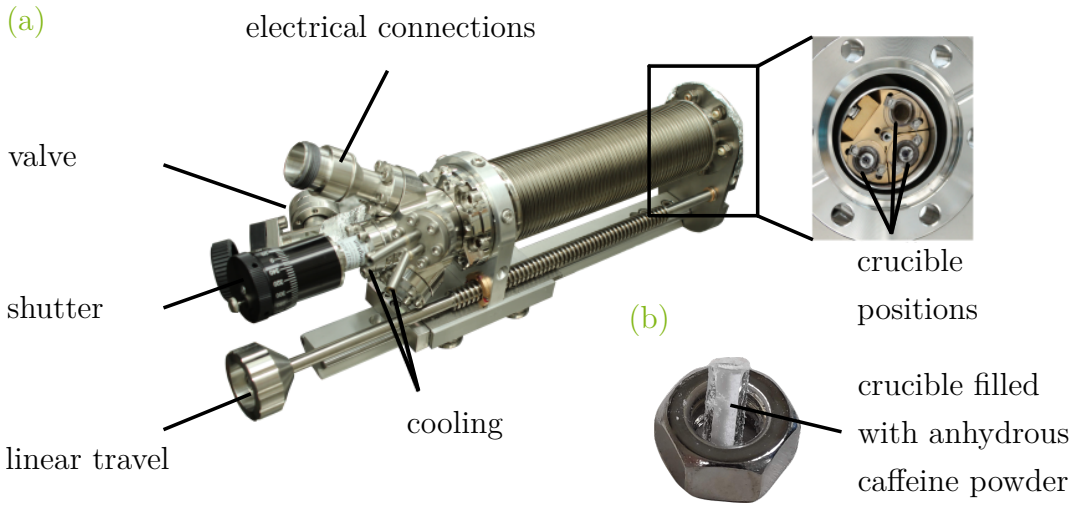

Figure 5.4: Representation of a three cell UHV evaporator for organic substances designed by *KENTAX* [140]. Image adopted from [141].

650 °C. The entire evaporator is water-cooled to thermally decouple the three independent evaporation crucibles. The integrated shutter plate allows to define the start and end point of the deposition process as well as the use of any possible combination of the three evaporation positions. The evaporator can be connected to an external pump station via the valve and has a linear travel of 180 mm.

In order to analyze the caffeine evaporation process a quartz crystal microbalance (QCM) is utilized. In principle, a QCM works via the eigenfrequency change of the thickness shear mode of a quartz crystal resonator by adding mass through adsorbate deposition. Due to the piezo electric effect, the quartz crystal (SiO_2) is excited to acoustic resonance with an external electric oscillator. The resonance frequency depends on the direction and thickness of the crystal cut, which in this case is an AT-cut with 400 µm thickness and an initial resonance frequency f_0 of around 6 MHz. The film thickness is then calculated with the Sauerbrey equation in first approximation by the change of frequency Δf, which is proportional to the adsorbed mass Δm [142]:

$$\Delta f = -\frac{2f_0^2}{\rho_q v_{tr} A}\Delta m \tag{5.1}$$

Hereby, the quartz density ρ_q, the transversal wave velocity v_{tr}, and the quartz crystal surface area A are used. To determine the film thickness d via $d = \Delta m \cdot (A \cdot \rho_{ads})^{-1}$, the density of the adsorbed material ρ_{ads} is required. The density depends strongly on the structure, therefore the density of a crystalline caffeine film is assumed to be equal the density of the caffeine high-temperature α-phase, $\rho_\alpha = 1.45\,\mathrm{kg/m^3} = \rho_{ads}$ [47]. This assumption is based on the structure found later in chapter 6. A monolayer (ML) height is

approximated to be one half of the height of the α-phase unit cell with $h_{\text{mono}} = \frac{c}{2} = 3.45\,\text{Å}$, which consists of two different layers of caffeine molecules, as shown in figure 2.3 (c) [47].

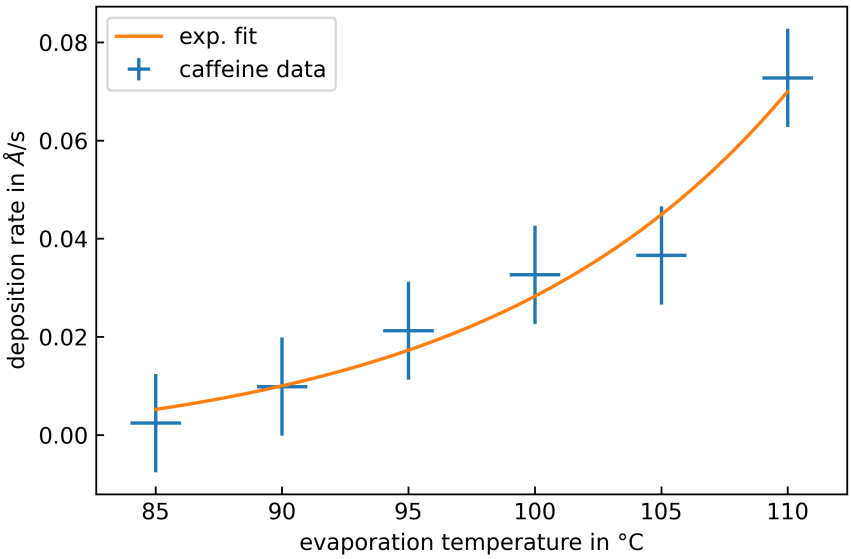

Figure 5.5: Measured deposition rate with the QCM as a function of the applied evaporation temperature in a distance of 254 mm. Reproduced from [143].

The used *QO 40A1* QCM is combined with a *TM14* thickness monitor as an oscillator, both purchased from *PREVAC*. Throughout the measurement the crystal resonance frequency is recorded with an accuracy of 0.01 Hz. The base pressure of the UHV chamber is below 5×10^{-10} mbar. As a first step the caffeine powder is carefully degased at a temperature of 70 °C to remove remaining impurities. At a pressure of 1×10^{-8} mbar, a temperature of 85 °C, and a distance of 254 mm between the evaporator and the QCM, first rates of caffeine deposition are measured as shown in figure 5.5. The uncertainty of the temperature is about ± 1 K and for the deposition rate of about ± 0.01 Å/s. An exponential increase of the deposition rate as a function of the evaporation temperature is observed. Since the sublimation temperature of caffeine molecules in UHV is relatively low, the bakeout temperature of the evaporator should not exceed 70 °C. In order to obtain a stable and reproducible preparation, an evaporation temperature of 100 °C is chosen for the further preparations. At this temperature a deposition rate of ~ 0.03 Å/s is achieved, resulting in a coverage of one monolayer after ~ 120 s with a thickness of ~ 3.45 Å. The caffeine sublimation process and film thickness determination with QCM is studied in collaboration with A. Wittrock, who published further details in his bachelor thesis [143].

In order to demonstrate that intact caffeine molecules are deposited on the crystal the sublimation process is checked by analyzing the residual gas with a QMS with electron

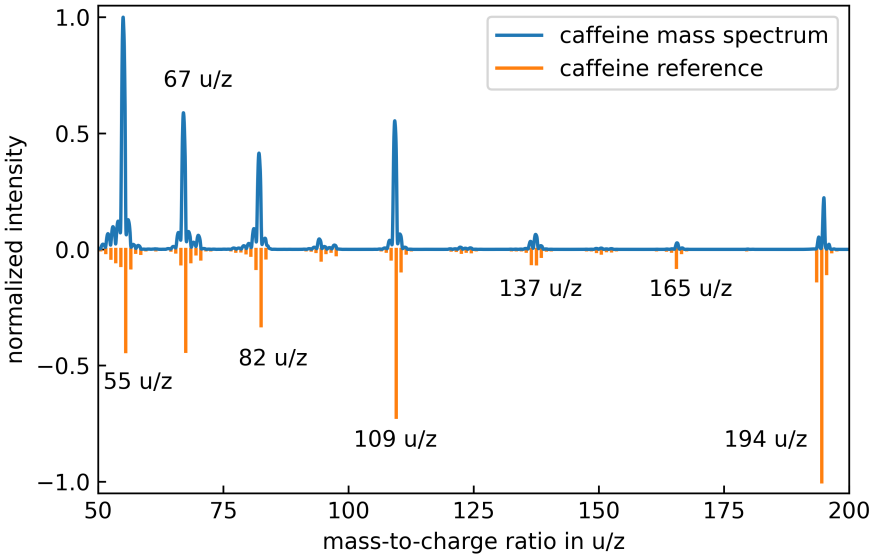

Figure 5.6: A mass spectrum of the residual gas during evaporation of caffeine molecules is presented in the upper part of the plot. The normalized ion current is depicted. In the lower part the intensity ratios of a caffeine reference spectrum is shown [144]. Both spectra are normalized with the highest intensity.

ionization. Excerpts from a typical mass spectrum during caffeine evaporation are shown in the upper part of figure 5.6. There, the ion current normalized in respect to the maximum is shown. In the lower part the intensity ratios of a reference mass spectrum data set from National Institute of Standards and Technology (NIST) are shown [144]. The characteristic caffeine cracking pattern is well reproduced, including the peak at 194 u/z, indicating intact caffeine molecules. The difference in the relative ion currents of the measured cracking pattern in comparison to the intensity ratios of the reference spectrum might be due to the lack of calibration of the used spectrometer. The ion current has to be calculated with sensitivity factors for different elements and atomic mass units to obtain the relative intensities. For residual gas analysis the measured ion current of the quadrupole mass spectrometer is sufficient, as calibration is expensive and time intensive. Furthermore, quadrupole mass spectrometers underestimate the number of particles of higher mass due to the stabilization condition. Moreover, different ionization energies lead to different cracking patterns [145].

Additionally, several studies using low pressure sublimation of caffeine show no decomposition of caffeine molecules during sublimation at temperatures between 135 °C to 155 °C [49, 146, 147]. Thus, the deposited molecules are expected to be intact on the surface and are analyzed in more detail in the next chapter.

Chapter 6

Room temperature measurements

This chapter presents the study of the self-assembly of caffeine molecules on the clean Au(111) surface at room temperature. Therefore, the chapter is divided into three sections. First, the deposition and formation of an ordered caffeine film on the gold surface is studied with STM in section 6.1. There, the caffeine monolayer is prepared as described in the previous chapter. In section 6.2, the ordered dense monolayer formation is investigated in more detail using STM, LEED, and DFT. Furthermore, a structural model based on the data shown is proposed in collaboration with the group of Prof. Dr. Oliver T. Hofmann and Andreas Jeindl. The proposed structure is then tested with XPS measurements of the monolayer system in the following section 6.3. The results presented in this chapter are published in the article *Structural investigation of caffeine monolayers on Au(111)* in Phys. Rev. B **101**, 245414 (2020) [148].

6.1 Coverage dependence

In order to analyze the caffeine growth on Au(111), the surface is investigated with STM after deposition. This section is divided into two parts. First, the focus is on the coverage dependent structural formation of caffeine. The second part deals with the temperature dependent assembly of caffeine in the monolayer regime.

After deposition

Investigating the formation of caffeine molecules on Au(111) after deposition without subsequent surface treatment, two growth conditions of caffeine molecules on Au(111) are found at room temperature. Figure 6.1 shows two STM images of a gold surface immediately after the deposition of different amounts of caffeine molecules. About 0.3 ML caffeine coverage in figure 6.1 (a) and about 1.3 ML in figure 6.1 (b) are deposited. This illustrates both present growth regimes, a low and a high coverage regime.

In the low coverage regime unordered caffeine molecule clusters as well as line-shaped structures are present at the substrate step edges. This indicates that the adsorption initially starts at the gold step edges as expected due to the increased reactivity at these edges [149]. Additionally, these assemblies are difficult to measure with a room temperature

STM since the interaction between the molecules and the tip are relatively high and several molecules are dragged across the surface during the measurement. The low coverage regime ranges from about 0.1 ML to 0.5 ML caffeine coverage and is represented by an example of 0.3 ML in figure 6.1 (a).

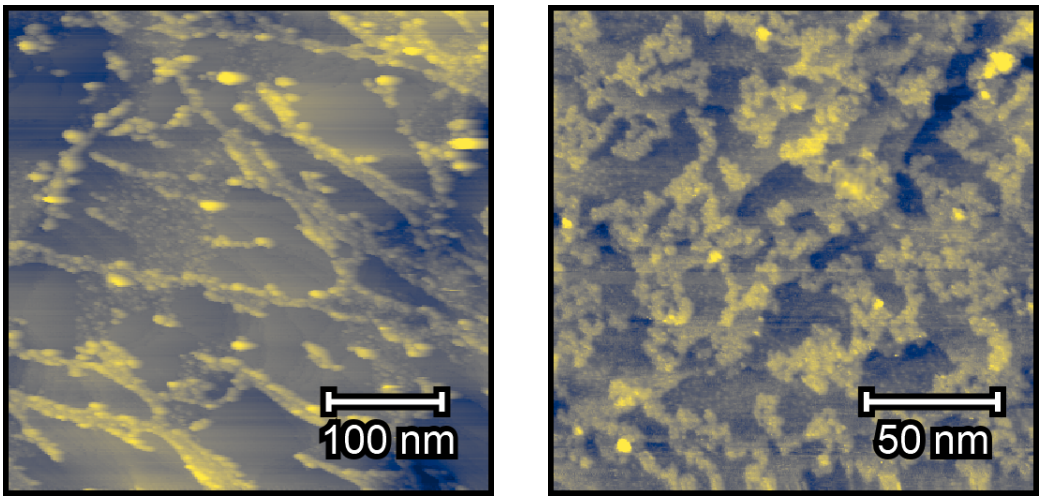

(a) ∼0.3 ML **(b)** ∼1.3 ML

Figure 6.1: STM images of Caffeine adsorption on Au(111) with different coverage of evaporated caffeine on top at room temperature. (a) Low coverage regime with ∼0.3 ML caffeine located at the surface step edges. (500 × 500 nm, 49 pA, −0.8 V). (b) High coverage regime with ∼1.3 ML caffeine aligned in clustered networks on the surface. (180 × 180 nm, 50 pA, −0.8 V).

The second structural regime was found for a caffeine coverage in the range of 0.7 monolayers to 1.8 monolayers. There, the caffeine molecules form random and not well-defined networks. Different peak heights are measured at the clustered arms with varying intermediate distances. Therefore, these networks are called amorphous layers or organic glass [150]. Figure 6.1 (b) shows an STM image representing the high coverage growth regime with 1.3 ML coverage.

regime	coverage	film condition
low	0.1 to 0.5 ML	step edge lines
high	0.7 to 1.8 ML	amorphous

Table 6.1: Growth regime of caffeine on Au(111) at room temperature as a function of coverage.

In summary, a continuous growth process with a low and a high coverage regime is observed. Initially, caffeine lines grow at substrate step edges, which successively develop into flat networks with increasing coverage. A comparison of both regimes is shown

in table 6.1. Further investigations on these disordered structures are omitted, since stable high-resolution images of these lines and networks are not achieved with STM at room temperature. Moreover, the structures change during the measuring process due to relatively strong molecule/tip interactions compared to molecule/molecule or molecule/surface interactions. Thus, the measuring process leads to a displacement of individual molecules and might interfere with the results. As a consequence, no self-assembled caffeine molecules were found at low coverage at room temperature. In chapter 7 a further analysis of submonolayer coverage at low temperatures is provided, as some of the mentioned difficulties at room temperature can be neglected there.

Substrate annealing

This section focuses on obtaining an ordered caffeine monolayer film on the Au(111) surface. The previous results show that the deposition of $\sim 1.3\,\mathrm{ML}$ caffeine at room temperature leads to the formation of networks of molecular clusters on the surface. The idea is to anneal these networks to induce sufficient mobility that the caffeine molecules form an ordered film [60]. Figure 6.2 shows a measurement series of caffeine molecule surface formations as a function of annealing temperature. Each sample was cleaned prior to deposition with repeated Ar^+-ion sputtering and annealing cycles. The caffeine deposition is performed as described above to obtain a coverage of slightly more than one monolayer. Each measurement is performed after a 10 min annealing step at the indicated temperature after the caffeine deposition. The indicated temperatures are derived from a calibration measurement with a K-type thermocouple spot-welded to a test gold crystal.

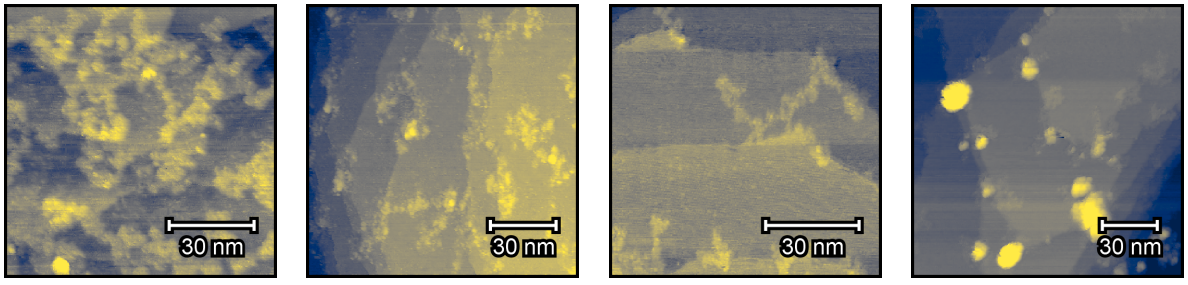

(a) $\sim 60\,^{\circ}\mathrm{C}$ **(b)** $\sim 70\,^{\circ}\mathrm{C}$ **(c)** $\sim 80\,^{\circ}\mathrm{C}$ **(d)** $\sim 100\,^{\circ}\mathrm{C}$

Figure 6.2: Surface assembly of $\sim 1.3\,\mathrm{ML}$ caffeine molecules on Au(111) with different annealing temperatures after deposition measured with the VT-STM. Each sample was heated by resistive heating for 10 min and is labeled with the respective temperature. (a) (50 pA, −0.8 V). (b) (35 pA, −0.8 V). (c) (36 pA, −0.8 V). (d) (36 pA, −0.8 V).

Figure 6.2 shows a series of STM images, sorted by temperature. All images are obtained in constant current mode. The first image 6.2 (a) shows the surface of the sample, which is

annealed at $\sim 60\,°C$ for 10 min after deposition. Clusters of caffeine molecules are visible, which are not ordered due to a lack of mobility. This is also confirmed by the strong similarity to the measurement in figure 6.1 (b), where the sample was not annealed after deposition. In figure 6.2 (b) the temperature is increased to $\sim 70\,°C$. This results in a less distorted coverage, with more clusters and fewer networks. Furthermore, there are flat and even areas between the large assemblies where the surface is covered with caffeine molecules. A distinctive pattern is not found, and no periodic order are visible in the LEED pattern. An annealing temperature of $\sim 80\,°C$ allows the caffeine molecules to arrange themselves in a regular, periodic pattern. This is depicted in figure 6.2 (c) and can be recognized by a fine pattern on the visible terraces. Additionally, some networks are still present. A different sample with the same preparation parameters is presented in figure 6.3, which is studied in more detail later. In figure 6.2 (d) the annealing temperature is set to $\sim 100\,°C$. There are only few molecular aggregations present, which are relatively high and have no ordered phase in between. Due to the relatively high temperature, most of the molecules were likely released from the surface.

In summary, an annealing temperature of $\sim 80\,°C$ and a coverage of ~ 1.3 ML is sufficient to create an ordered film on the gold surface. At this coverage the STM images show a homogeneous, ordered molecular film with some caffeine islands on top, as shown in figure 6.3. In the following, a detailed analysis of this ordered phase is presented. The preparation of well-ordered caffeine films could also be achieved by slowly cooling down the gold crystal from 700 °C to room temperature with a cooling rate of $\Delta T \sim 20\,K/min$, at a background pressure of 1×10^{-8} mbar caffeine gas. Moreover, the QCM measurements of evaporated caffeine indicate a decreasing film thickness after stopping the deposition process. This indicates a self limiting adsorption process, which is common for physisorbed organic films [60, 151].

6.2 Dense monolayer formation

In this section the previously found ordered caffeine film is analyzed by means of STM,LEED, and DFT. Hence, this section is divided into three parts, one for each method, respectively. Initially, the real space images of the ordered film taken with STM are examined more closely and an estimate of the lattice vectors is given. After that, this analysis is validated with the LEED method and a structural model of the surface is proposed. Finally, the results are checked with DFT and a geometric optimization of the surface model is performed. The resulting structure is then described in more detail.

6.2.1 Investigation with RT-STM

With the results of the previous section, it is possible to obtain an ordered caffeine film on a Au(111) crystal in a reproducible fashion. Using the found preparation parameters a sample with 1.3 ML caffeine coverage, annealed for 10 min at 80 °C is investigated in more detail. An overview image of this sample in figure 6.3 (a) shows homogeneously covered substrate terraces with some caffeine islands on top. The 'herringbone' reconstruction of the substrate is still visible through the adsorbate film. An additional measurement showing a close-up of figure 6.3 (a) is depicted in figure 6.3 (b). Utilizing the gold surface reconstruction, the crystal directions can be identified as marked in figure 6.3 (b). The area of the gold bridge positions are slightly increased and therefore are clearly visible in the STM measurement. As described earlier and shown in figure 2.7 the substrate domain is oriented along the $[11\bar{2}]$ direction. Noting, that the $(22 \times \sqrt{3})R30°$ rotates by 120° and thus the $[11\bar{2}]$ direction corresponds to the directions $[1\bar{2}1]$, $[\bar{2}11]$, and their inverse. In this work, the substrate axis of these three, which points most clearly upwards, is defined as the $[11\bar{2}]$ direction, therefore all rotated axis are labeled accordingly. Hence the defined axis in figure 6.3 (b) is the $[1\bar{2}1]$ direction.

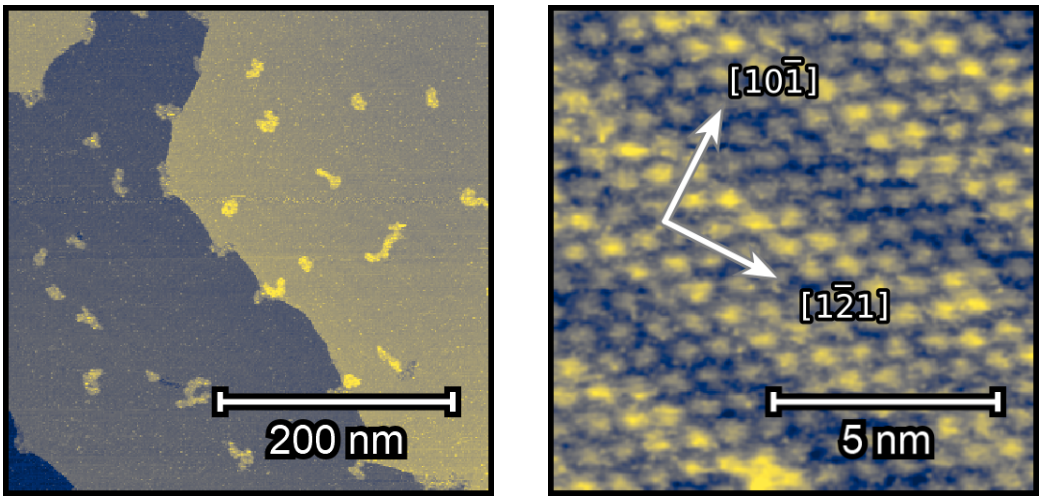

(a) ~ 1.3 ML / ~ 80 °C for 10 min **(b)** close-up of 6.3 (a)

Figure 6.3: STM images of caffeine adsorbed on Au(111). (a) After heating the substrate at 80 °C for 10 min the caffeine film of ~1.3 ML coverage is found homogeneous with some islands on top (500 × 500 nm, 10 pA, −2.0 V). (b) Close-up view of the surface with hexagonal caffeine monolayer formation on Au(111) (36 × 36 nm, 17 pA, −1.0 V).

The ordered film is present evenly across the entire sample surface. A further measurement presented in figure 6.4 (a) is showing several 'herringbone' substrate domains which are fully covered with caffeine molecules. The 2D-FFT of this measurement revealed six discrete

spots of the dense caffeine monolayer as shown in figure 6.4 (b). Furthermore, in the center of the 2D-FFT the spots of the 'herringbone' reconstruction are visible. Accordingly, the substrate reconstruction has not changed structurally due to the adsorbed caffeine film, so this is an experimental indication of a weak adsorbate-substrate interaction [76].

The caffeine spots in figure 6.4 (b) are approximately equidistant located from the origin and from each other, revealing a sixfold symmetry and thus a hexagonal caffeine formation on Au(111). In order to confirm this hypothesis and to estimate the lattice constant and the angle between the adsorbate unit cell vectors the PSDF from the gwyddion software package is used. Applying this method to over 100 STM measurements and deriving the lattice constants from each measurement resulted in an averaged nearest neighbor distance of caffeine molecules on the surface of (8.7 ± 0.9) Å with an angle of $(60 \pm 3)°$ between two nearest neighbors. This validates the hypothesis of a hexagonal arrangement of the caffeine molecules. Additionally, an angle of $(10 \pm 3)°$ was observed between the substrate $[1\bar{1}0]$ direction and one caffeine domain direction. With this observation the caffeine domain directions are estimated to be $[41\bar{5}]$, $[5\bar{4}\bar{1}]$, and equivalent directions, which are indicated in figure 6.4 (a).

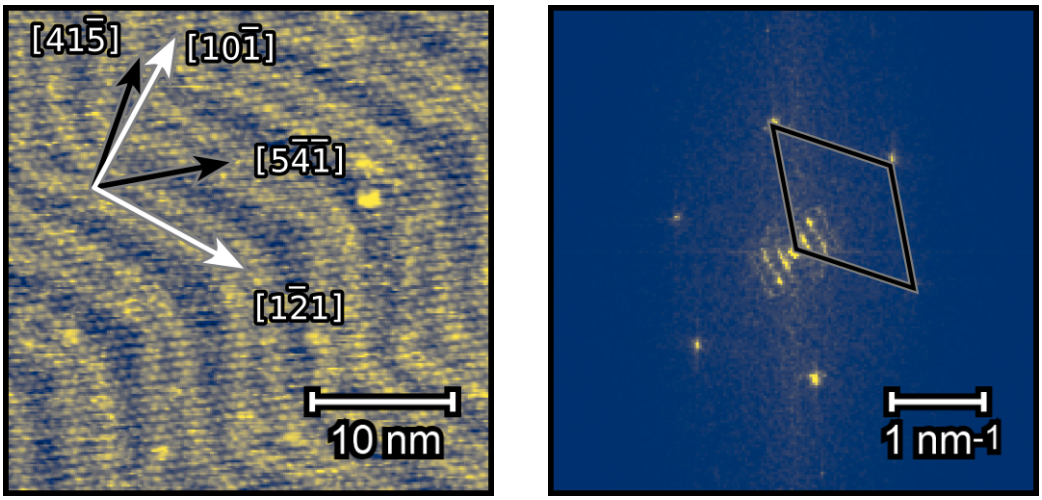

(a) STM measurement **(b)** FFT of figure 6.4 (a)

Figure 6.4: (a) STM image of a caffeine monolayer on Au(111). An angle of $(10 \pm 3)°$ was observed between the substrate $[10\bar{1}]$ direction and the caffeine $[41\bar{5}]$ direction. (19×19 nm, 16 pA, -1.0 V). (b) Fast Fourier transform corresponding to (a) showing six spots and the corresponding FFT pattern of the Au(111) herringbone reconstruction.

Moreover, two distinct hexagonal domains of caffeine molecules rotated by $\sim 20°$ were found on the Au(111) surface. However, the angle towards the Au$[1\bar{1}0]$ direction remains about $\pm 10°$ for both domains. Therefore, the two domains are possibly mirrored along the

Au[1$\bar{1}$0] direction. For the two mirrored caffeine domains, two different domain boundaries were found.

In figure 6.5 (a) the two mirrored domains separated by a substrate step-edge are shown. Furthermore, one hexagonal axis of each domain is indicated with a gray or black line, respectively. Additionally, in figure 6.5 (b) the result of a FFT applied to the data of figure 6.5 (a) is displayed. The FFT clearly reveals 12 spots corresponding to the two hexagonal caffeine domains. The rotation angle between both domains averaged over several STM images is $(20 \pm 3)°$. Domain boundaries at substrate step-edges are common and have been found, for example, for self assembled monolayers of alkanethiols [152].

In addition, domain boundaries were also found on the same substrate terrace as shown in figure 6.5 (c). There, the dividing line between both domains is marked with a semi-transparent white area. A white and a black line are drawn as orientation marker indicating one of the hexagonal axes of each domain. Hereby, the black one is aligned with the hexagonal lattice of the domain shown on the left, and likewise the white line for the domain on the right side. Additionally, a hexagonal grid is marked on top of a small area of each domain to visualize all domain axes and one unit cell of the grid is highlighted. Domain borders on the same terrace show no sharp edges and some minor defects are visible. The shape of these borders is likely an indication of high mobility of the molecules at room temperature. Moreover, it is possible that this second type of domain boundary is a twin boundary, which could be induced due to the chiral growth of the caffeine domains [66, 153]. Therefore, an analysis of the caffeine molecule on-surface chirality follows in section 6.2.3. In addition, figure 6.5 (d) shows the FFT of figure 6.5 (c), which also reproduces the 12 point pattern of both domains.

It should be noted that all STM measurements at room temperature are subject of slight shear and distortion due to piezo effects [154]. Therefore, the experimental uncertainty depends largely on the measured shear of approximately 3°, so every angle measurement is connoted with this uncertainty, since their statistical uncertainty is much smaller. To validate the measured lattice constant and angles additional LEED measurements are presented in the next section.

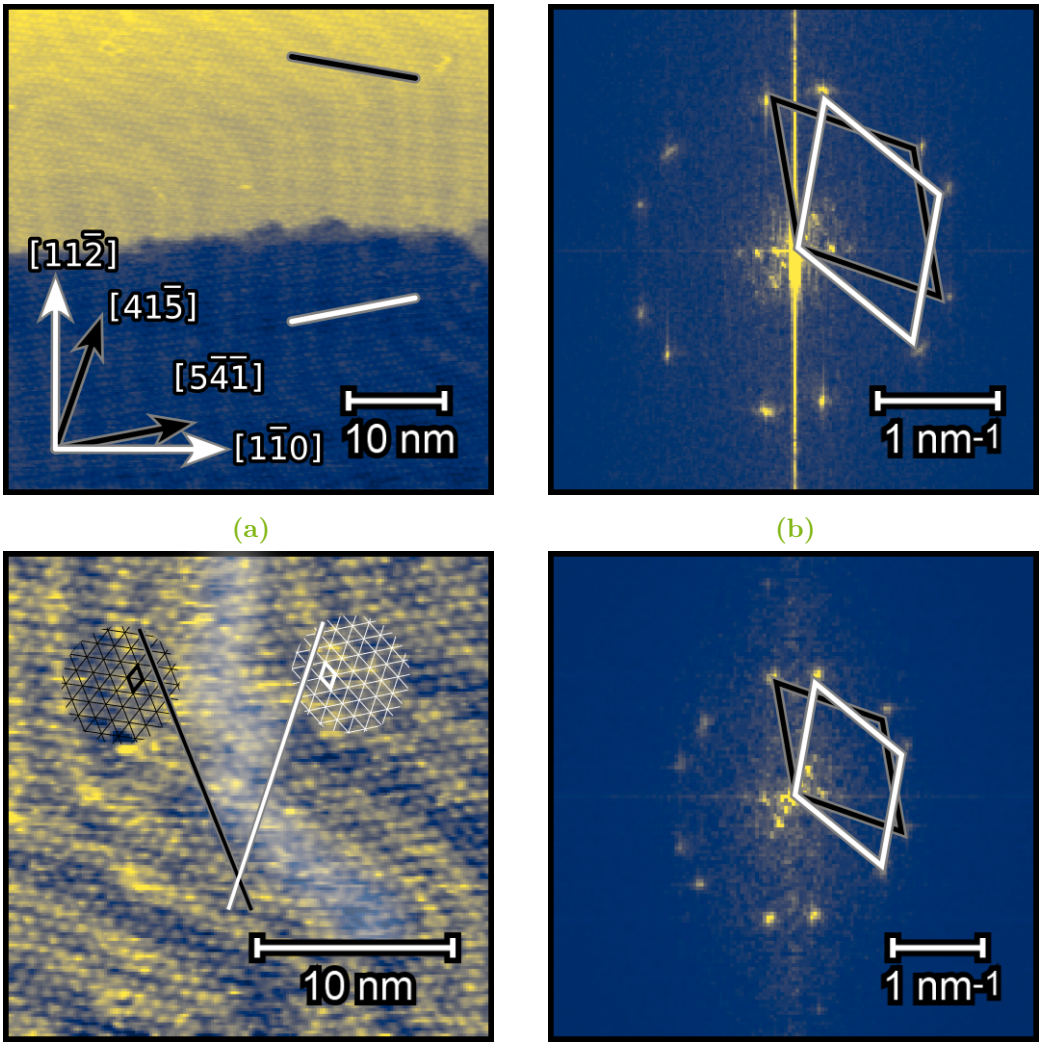

(a) (b)

(c) (d)

Figure 6.5: Representation of two types of domain boundaries present in dense caffeine monolayers on Au(111). (a) STM image of a caffeine monolayer on Au(111) with both mirrored film domains separated by a substrate step-edge (19×19 nm, 16 pA, -1.0 V). (b) Fast Fourier transform corresponding to (a) showing twelve spots. (c) Domain border of a dense caffeine monolayer on the same substrate terrace (28×28 nm, 17 pA, -1.0 V). (d) Fast Fourier transform corresponding to (c) showing twelve spots.

6.2.2 LEED analysis

The LEED measurements are complementary to STM and obtain a k-space image of the real space periodicities measured with STM. Furthermore, LEED measurements are rather fast compared to STM measurements. Therefore, they are conducted to verify the successful preparation and gather more insights of the system.

In figure 6.6 two LEED measurements of the sample after successful caffeine monolayer preparation are shown. In figure 6.6 (a) the expected twelve spots of the caffeine monolayer are present, measured at a kinetic energy of $E_{kin} = 20\,eV$. Thus, the LEED measurements confirm the monolayer growth in a hexagonal pattern and that the two distinct domains are rotated about 20°, indicating that these two domains are predominantly present at the surface. As shown in figure 6.6 (b), the Au(111) substrate spots are still visible and intact at $E_{kin} = 55\,eV$ despite the adsorbate layer on top. The intensity of the Au LEED spots significantly decreases due to the additional caffeine monolayer on top and overall the background noise increases. Moreover, the LEED spots of the caffeine monolayer vanish for electron energies over $\sim 30\,eV$ and hence are not visible in figure 6.6 (b). Since Au(111) spots are first visible on the screen above $\sim 50\,eV$, it was not feasible to take an image of Au and caffeine spots at the same time.

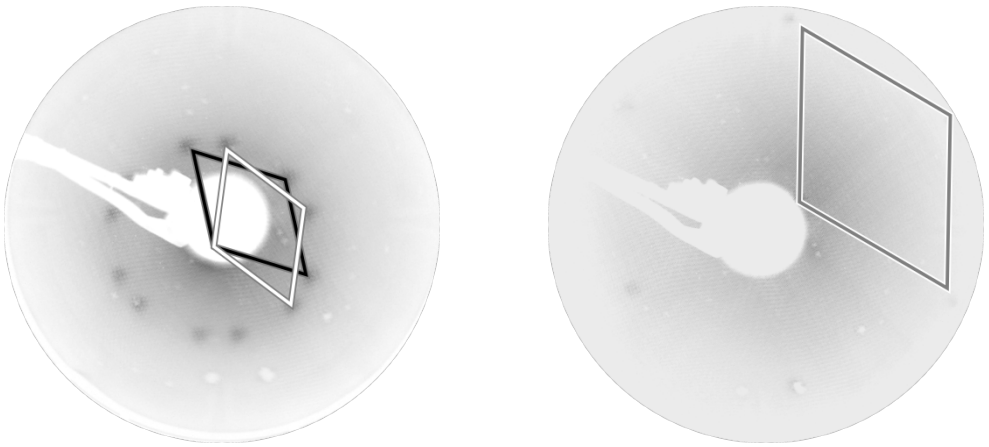

(a) $E_{kin} = 20\,eV$ **(b)** $E_{kin} = 55\,eV$

Figure 6.6: LEED images of caffeine molecules adsorbed in a periodic arrangement on Au(111). In 6.6 (a) the twelve spot adsorbate diffraction pattern is visible indicating two mirrored hexagonal domains. In 6.6 (b) the diffraction pattern of the gold substrate is barely visible since the caffeine monolayer is on top, thus the spot intensity decreases significantly. Noting, that the sample was slightly moved between both measurements.

It should be added that there are several difficulties within the LEED measurement of organic films. The intensity of the adsorbate spots decreases while the sample is irradiated

with electrons within several seconds. This phenomenon presumably occurs because the electron beam damages the caffeine molecule assembly due to the weak adsorbate/adsorbate and adsorbate/substrate interactions. Higher electron energies lead to a faster decrease of the spot intensity. Thus, the LEED experiments to check the sample preparation were performed at a single low electron energy, around 20 eV, to reduce the risk of beam damage on the sample. Noting, that LEED measurements at such low kinetic energies are particularly susceptible to interference from electromagnetic fields. In order to obtain LEED images at several kinetic energies, the sample was moved in the x-y plane, since the focused electron beam is smaller than 1 mm in diameter. Thus, every image was taken at an undamaged sample area. An additional problem that could occur is that the caffeine molecules, which are present in the residual gas of the UHV chamber after the evaporation, can be trapped inside the electron gun of the LEED system and block the electron beam. Degassing the LEED filament for several hours solves this issue.

Since substrate and adsorbate diffraction spots cannot be measured at the same electron energy in LEED, the measurements are performed at different energies but with the same experimental parameters and are thus still comparable. The images are taken at a fixed sample - LEED screen distance and a fixed camera position and therefore it is possible to compare images in one series in terms of relative distances and angles measured in these images. Excerpts of one LEED measurement series are shown in figure 6.7. The LEED series reveals a rotation angle of the two distinct caffeine domains of $(11.0 \pm 0.8)°$ towards the Au $[1\bar{1}0]$ direction, measured across several LEED images at different energies. This result confirms the STM measurements of $(10 \pm 3)°$ between each domain and the Au $[1\bar{1}0]$ direction.

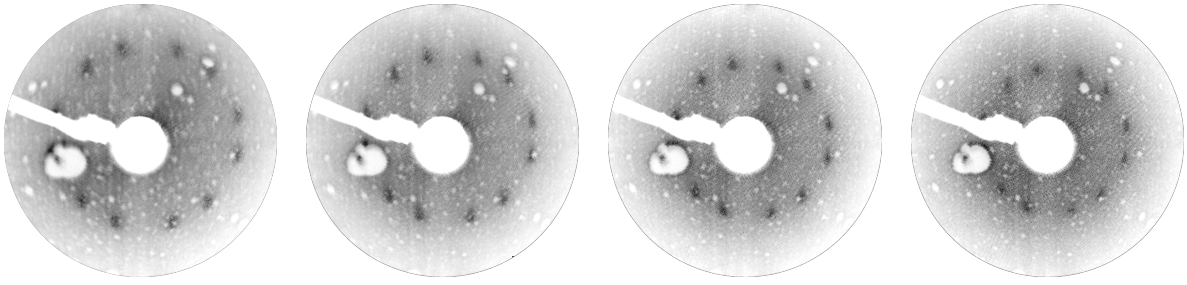

(a) $E_{kin} = 14\,eV$ **(b)** $E_{kin} = 16\,eV$ **(c)** $E_{kin} = 18\,eV$ **(d)** $E_{kin} = 20\,eV$

Figure 6.7: Excerpts of one LEED series of the caffeine monolayer formation on Au(111) with kinetic electron energies from 14 eV to 20 eV. The spot intensity variation towards higher kinetic energies partly results from different sample positions for single images in order to decrease beam damage effects.

In order to access the lattice constant of the adsorbate film with LEED, the following technique described by Lackinger *et al.* for coronene on Ag(111) is applied [155]. For

this method, an alternative expression of the Laue equation is used, which describes the constructive diffraction at atomic layers. With a lattice constant a, the diffraction order n, the probing wavelength λ and the observing angle Θ, the expression is:

$$a \sin(\Theta) = n\lambda. \tag{6.1}$$

The sample is probed with electrons, therefore the de Broglie wavelength is used:

$$\lambda = \frac{h}{\sqrt{2m_e E_{kin}}}. \tag{6.2}$$

The diffraction angles are made visible at the LEED screen and therefore are measured as a distance which is calculated with trigonometry to $s = R \sin(\Theta)$, where R is the screen radius. Expanding this expression with the Laue equation and the de Broglie wavelength, the following result for the measured length s on the screen is:

$$s = \frac{1}{a} \cdot \frac{hR}{\sqrt{2m_e}} \cdot \frac{1}{\sqrt{E_{kin}}} \tag{6.3}$$

Therefore, the relative distance of every spot towards the (0 , 0)-spot in relation to the screen diameter is plotted in one image against $1/\sqrt{E_{kin}}$. This can be modeled with a line through origin with the slope m which is defined via the specific lattice constant a. The quotient of two different slopes is in the same proportion as its lattice constants:

$$\frac{m_{adsorbate}}{m_{substrate}} = \frac{a_{substrate}}{a_{adsorbate}} \tag{6.4}$$

Using sequences of LEED measurements like to the one in figure 6.7, the relative distances are measured and plotted in figure 6.8. This is performed for the adsorbate spots as well as for the substrate spots. With a linear regression and the known substrate lattice constant of $a_{Au} = 2.884\,\text{Å}$ [156], a caffeine nearest neighbor distance of $(8.6 \pm 0.3)\,\text{Å}$ is obtained from the LEED patterns. This result is in perfect agreement to the nearest neighbor distance of $(8.7 \pm 0.9)\,\text{Å}$ measured with STM. Therefore, the measured nearest neighbor distance of $(8.6 \pm 0.3)\,\text{Å}$ and a rotation of $(11.0 \pm 0.8)°$ towards the Au $[1\bar{1}0]$ direction lead to a quasi-hexagonal superlattice which can be described with the matrix $\left(\begin{smallmatrix} 3.3 \pm 0.3 & 0.66 \pm 0.06 \\ 2.6 \pm 0.3 & 3.3 \pm 0.3 \end{smallmatrix}\right)$ and its mirror-symmetric counterpart $\left(\begin{smallmatrix} 3.3 \pm 0.3 & 2.6 \pm 0.3 \\ 0.66 \pm 0.06 & 3.3 \pm 0.3 \end{smallmatrix}\right)$ with the gold basis vectors of the unreconstructed gold surface shown in figure 6.9 (b).

Using these results a first structural model can be proposed, which is shown in figure 6.9. For this model the large $(22 \times \sqrt{3})R30°$ substrate reconstruction is neglected. This assumption

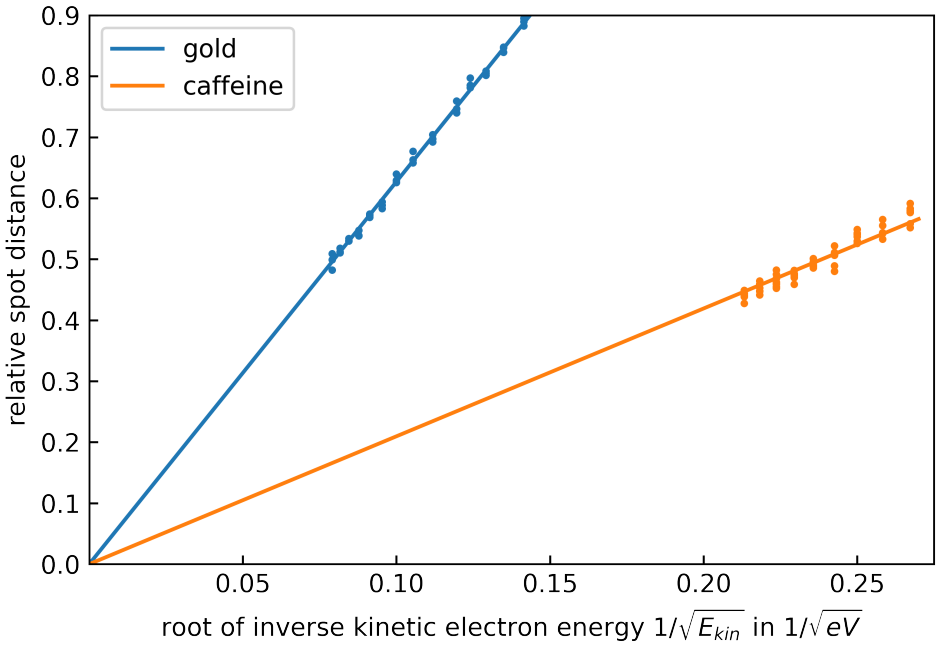

Figure 6.8: Linear regression of relative LEED spot distances of gold and caffeine diffraction pattern measured across a sequence of LEED measurements similar to figure 6.7.

is based on the observation, that no strong influence of the substrate reconstruction on the caffeine monolayer was found in the STM measurements. Furthermore, the substrate is compressed by around 4 % in one direction and therefore the influence of the gold surface reconstruction should be small. In addition, this assumption is well documented in literature for organic films as it decreases the computation time significantly [53, 157]. Simulating the molecular surface structure with the LEEDpat package, an approximation in fractional numbers is found with the higher-order commensurate matrix $\left(\begin{smallmatrix} 10/3 & 2/3 \\ 8/3 & 10/3 \end{smallmatrix}\right)$- and its corresponding mirrored $\left(\begin{smallmatrix} 10/3 & 8/3 \\ 2/3 & 10/3 \end{smallmatrix}\right)$-structure. Additional, this structure can be described in Wood notation, as a $\left({}^{2}/_{3}\sqrt{21} \times {}^{2}/_{3}\sqrt{21}\right)R{\pm}10.9°$-superstructure. This superstructure with a single molecule in the unit cell is depicted in blue in figure 6.9.

Since the fractions can be expanded towards an integer epitaxy-matrix, it is possible to describe the surface structure as a commensurate structure. Expanding the matrix results in a cell that is three times larger with potentially three uniquely aligned molecules on top of the Au(111) surface. These superlattices are described by the epitaxy-matrix $\left(\begin{smallmatrix} 6 & 4 \\ 2 & 6 \end{smallmatrix}\right)$- and its mirrored $\left(\begin{smallmatrix} 6 & 2 \\ 4 & 6 \end{smallmatrix}\right)$- matrix, or as a $\left(2\sqrt{7} \times 2\sqrt{7}\right)R{\pm}19.1°$-superstructure in Wood notation. These unit cells are also hexagonal with a lattice constant of 15.2 Å and contain three molecules. This structural model is represented in orange in figure 6.9.

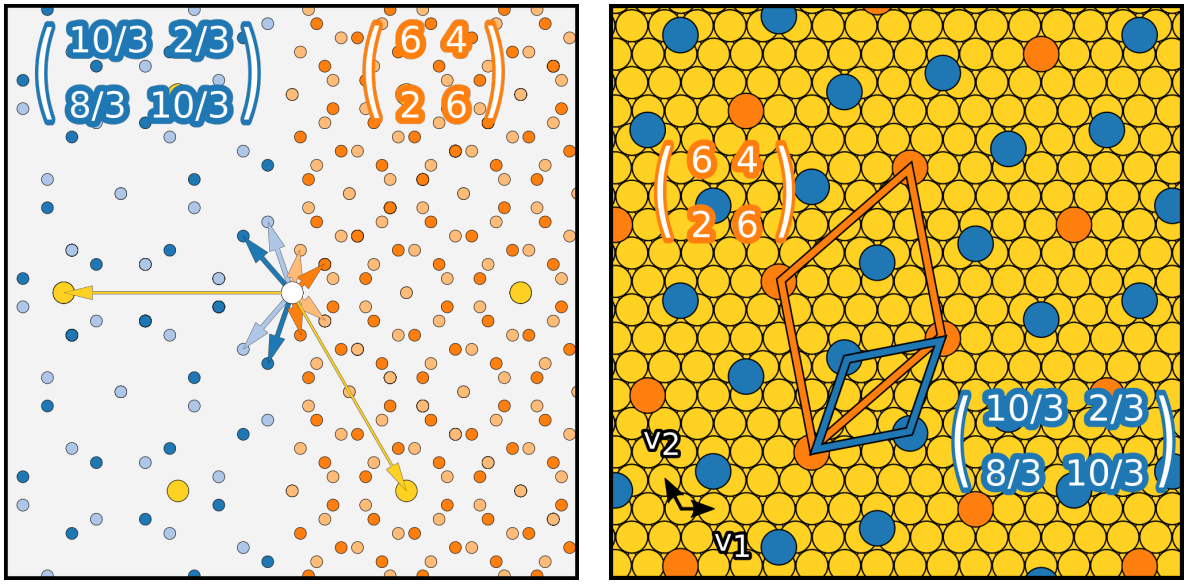

(a) (b)

Figure 6.9: (a) LEEDpat simulation of two possible superstructures. On the left the simulated LEED pattern of a one molecular $\begin{pmatrix} 10/3 & 2/3 \\ 8/3 & 10/3 \end{pmatrix}$-superstructure is printed in dark blue and its mirrored domain in light blue. On the right a three molecular $\begin{pmatrix} 6 & 4 \\ 2 & 6 \end{pmatrix}$-superstructure is printed in dark orange and its mirrored domain in light orange. The Au(111) substrate LEED pattern is printed in yellow color. (b) Real space structural model of one domain of caffeine molecules on Au(111). The one molecular superstructure is printed in blue and the three molecular unit cell is printed in orange, each unit cell is shown in its respective color. The Au substrate is depicted in yellow.

Figure 6.9 provides a comparison between the models of both described structures. The LEEDpat simulations are shown in figure 6.9 (a) and the real space surface models are shown in figure 6.9 (b). The simulated LEED pattern in figure 6.9 (a) is dived into two parts. The left half shows a superposition of both domains of the single molecular superstructure represented with blue circles. The two distinct patterns for each domain are indicated by two shades of blue, a light and a dark one. For the right part its commensurate counterpart with three times the unit cell size is used for the simulation. It is represented with orange circles in different shades, a dark and a light one, for each domain sub-pattern. The substrate Au(111) diffraction pattern is depicted in yellow. All basis vectors are displayed in the corresponding color. In the resulting simulation pattern all spot positions of the single molecular structure are reproduced in the three molecular pattern. This is due to the larger unit cell, which results in more diffraction spots with decreased distances between individual spots. Note, that the LEEDpat simulation only calculates the positions of possible diffraction spots. No information about spot intensities is obtained from this method.

Furthermore, in figure 6.9 (b) a real space surface model of one domain is depicted with single caffeine molecules represented in blue and orange, and the substrate gold atoms in yellow. The cell of the single molecular $\begin{pmatrix} 10/3 & 2/3 \\ 8/3 & 10/3 \end{pmatrix}$-superstructure is marked in blue and the three-molecule $\begin{pmatrix} 6 & 4 \\ 2 & 6 \end{pmatrix}$ unit cell in orange. The molecule positions which are indicated in orange are also molecule positions of the blue pattern and vice versa. The orange ones describe the periodicity of the larger three molecular commensurate unit cell. Both superstructures have the same density of caffeine molecules on the surface. This model shows that all molecular positions on the surface are described by both superstructures. The main difference is that in the single molecule unit cell, each molecule is aligned in one distinct orientation in a higher-order commensurable cell, and in the three molecule unit cell, three different molecular positions are allowed in a commensurable cell. It should be added that the adsorbate positions with respect to the gold surface, shown here as a on top, fcc hollow, and hcp hollow position are not necessarily true, since the model only represents the underlying periodicity.

As previously shown in figure 6.6 (a), the LEED measurements yield only twelve spots corresponding to the LEEDpat simulation of the single molecule unit cell. Therefore, the LEED measurements indicate that this surface structure is more likely to be present on the surface than the commensurable three molecular cell, which would result in more visible diffraction spots in the LEED pattern. Since the STM measurements do not clearly resolve the orientation of single molecules, and slight background noise is present in the LEED measurements, a further method is used to determine the surface structure in detail.

6.2.3 DFT calculations

To gain further insight into the monolayer formation, the surface structure of caffeine on Au(111) is investigated using DFT. The DFT study is gratefully conducted by Andreas Jeindl and Prof. Dr. Oliver T. Hofmann from the Graz University of Technology. The calculations are performed on the Vienna Scientific Cluster (VSC) with the funding of the Austrian Science Fund (FWF): P28631-N36 and Y1157.

A starting point for the analysis with ab-initio simulations is the observation, that the 'herringbone' reconstruction of the gold substrate is undisturbed under the caffeine monolayer, and therefore the interaction between the caffeine adsorbate and the gold substrate is sufficiently weak. Hence, the adsorbate/substrate interaction is neglected in the first part of the DFT investigation. Furthermore, the XPS data presented in section 6.3, also show that no measurable chemical interactions are present, further strengthening this assumption. Therefore, the system is studied in a two step procedure. First, the caffeine

molecules are modeled in a free-standing monolayer without substrate interactions to gain insight into the molecule-molecule interaction. These molecule-molecule interactions are investigated by mapping the chemical interactions between pairs of molecules in the free-standing monolayer. In the second step, the full molecule-substrate system is simulated using the results from the free-standing analysis to investigate the whole monolayer system. The DFT calculations are performed using the FHI-aims package [135]. The default basis set of the FHI-aims package and the exchange-correlation functional PBE are used [158]. Long-range dispersion is included via the TS^{surf} correction [134]. For more technical details about the simulation see [148].

Free-standing caffeine monolayer

Constructing the hypothetical monolayer of caffeine molecules, the geometry of an isolated caffeine molecule is optimized with the FHI-aims package and then the quasi-planar molecule is aligned parallel to the surface orientation. The assumption of flatly aligned molecules is based on the model of high temperature α-phase caffeine crystals [47], which is also used for the QCM layer thickness determination. Moreover, theoretical analysis for quasi-planar achiral molecules predict that this type of molecules align in a hexagonal planar phase [50]. For the calculation, one molecule is fixed in the center of the xy-plane, and then the interaction energy between the fixed molecule and a second molecule aligned flatly in the same plane is calculated. A suitable discretization for this calculation is used to limit the computational time. Hence, a hexagonal grid with 1/4th of the minimal Au-Au distance, $a_{\text{grid}} = 0.738\,\text{Å}$ is used for the translation of single molecules. To model different rotations, the second molecule is rotated in steps of 30° around the central pyrimidine ring, starting with the same alignment as the fixed molecule in the center. Since the caffeine molecule can adsorb on the surface in two mirror-symmetric ways, the calculation is performed in a homochiral and a heterochiral way, with both molecules in the same and mirror-symmetric orientations, respectively.

The interaction energies between two caffeine molecules without the substrate are derived from the described calculation and are shown in figure 6.10. The homo- and heterochiral alignments are represented in 6.10 (a) and 6.10 (b), respectively. An attractive and repulsive interaction of the molecule pair is represented by blue and red color, respectively. The diverging colormap representing the different energies is shown on the right side. In the center of each plot the fixed caffeine molecule, which remains in that specific orientation during the calculation, is shown. Within the molecule, carbon atoms are indicated in gray, nitrogen atoms in blue, oxygen atoms in red, and hydrogen atoms in white. At every point on the hexagonal lattice, the second molecule is rotated with respect to the

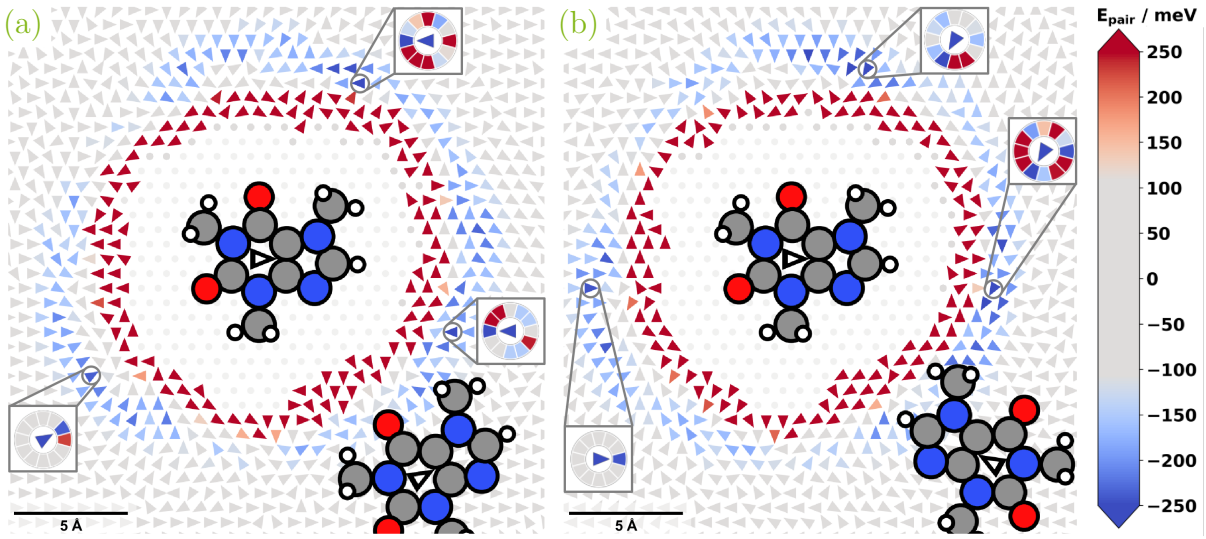

Figure 6.10: Discretized pairwise interactions of caffeine molecules in a free-standing monolayer in two chiral arrangements (a) and (b). In the bottom right corner of both plots the in-plane geometry of a molecule, relative to the centered fixed molecule, is shown with the corresponding arrow in the center of the pyrimidine ring. The arrows represent the energetically most favorable in-plane rotation of the second caffeine molecule at each respective location. The insets visualize the interaction energies for all different rotations at the energetically most favorable positions in each of the three energetically favorable areas. (a) Pair interaction energy for a homochiral alignment. (b) Pair interaction energy results for heterochiral caffeine molecules [148].

fixed molecule in the center and the interaction energy between this pair of molecules is calculated. The results show the orientation with the lowest interaction energy with a colored arrow indicating the most favorable orientation of the second molecule at that lattice point. The arrow color represents the interaction energy. For further understanding, the three lowest interaction energies in each plot are marked with a circle of colored segments. Each segment color represents the interaction energy for each discrete molecular rotation in increments of 30°. The arrow inside the circle points in the most favorable direction and has the color of the smallest interaction energy. Thereby, the orientation of the arrow with respect to the caffeine molecule is indicated by the corresponding arrow in the center of the pyrimidine ring of the molecules shown at the bottom of each figure.

These computational results show that caffeine molecules in a homochiral orientation have three distinct regions where the interaction is beneficial. These three regions are highlighted by the previously described three insets of the most favorable alignments in figure 6.10 (a). In none of these regions it is energetically favorable to align the molecules parallel to each other. Rather, it is energetically more favorable to form an antiparallel or slightly rotated alignment to each other. Therefore, it seems unlikely to achieve a

monolayer alignment with a single molecule per unit cell, where all molecules are oriented equally.

The analysis is similar when both molecules have the opposite chirality on the surface. The most energetically favorable interactions are shown once again via the circular insets. They show that the molecules in the most energetically favorable arrangements are again rotated relative to each other, as shown in figure 6.10 (b). An exception is the region on the left side of figure 6.10 (b). There a parallel orientation of the mirrored molecules is favorable. This could describe 1D lines of caffeine molecules consisting of at least two alternating prochiral molecules per unit cell. This alignment would not construct a full 2D homochiral surface structure. Therefore, it seems unlikely that caffeine molecules form a ordered monolayer formation with a single molecular unit cell, where all molecules have the same alignment and chirality.

Caffeine monolayer on the Au(111) surface

The DFT results of a hypothetical freestanding monolayer show that a single-molecule unit cell is energetically not favorable. Therefore, the commensurable three molecule structure is further investigated as a full caffeine monolayer on Au(111). Noting, that the caffeine molecules are allowed to arrange themselves equally in the simulation of the dense monolayer on the substrate. Therefore, the homochiral single molecular unit cell is part of the simulation design. The approach is to find the most energetically favorable caffeine arrangement within the given supercell. To achieve this goal, ideas of the structure-search algorithm SAMPLE developed by L. Hörmann *et al.* are utilized [159].

The monolayer film is modeled with the smallest superlattice, which is commensurable with the Au(111) substrate. This and also the mirrored superlattice were introduced before and represented in figure 6.9. These superlattices are the $\left(\begin{smallmatrix}6 & 4\\ 2 & 6\end{smallmatrix}\right)$- and its mirrored $\left(\begin{smallmatrix}6 & 2\\ 4 & 6\end{smallmatrix}\right)$-superlattice, or $\left(2\sqrt{7}\times 2\sqrt{7}\right)R{\pm}19.1°$ in Wood notation. These unit cells preserve hexagonal symmetry, have a lattice constant of 15.2 Å with respect to an unreconstructed Au(111)-surface, and contain three molecules. All possible structures with three caffeine molecules fitting into the unit cell are calculated within the described discretization. Using the previously calculated interaction energies of the free-standing monolayer in the gas phase, the relative energies for all of these possible structures are determined. From this, these structures are ranked in terms of relative energy and the most energetically favorable structure is identified. This structure manages best to balance repulsion by tight packing and attraction due to favorable intermolecular interactions. Therefore, this structure is geometry optimized and presented in figure 6.11. Within the caffeine molecule, carbon

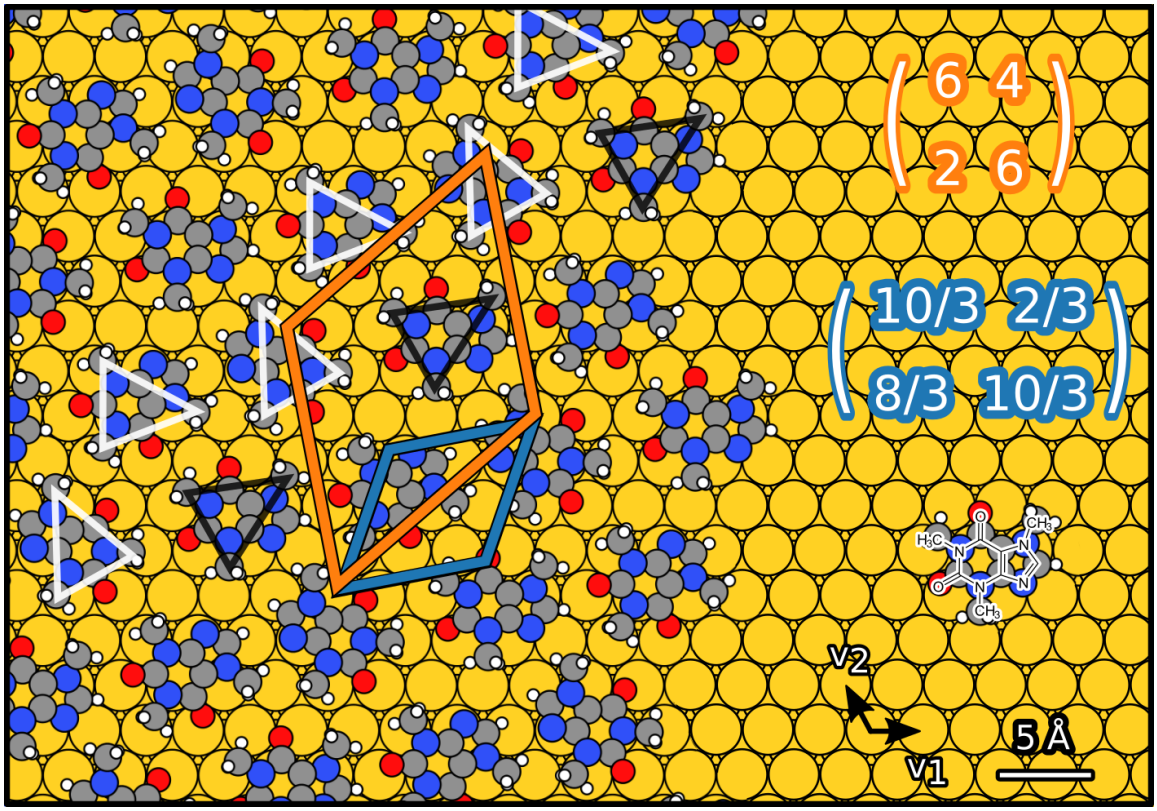

Figure 6.11: Geometry-optimized monolayer of caffeine molecules with three molecules in a $\left(\begin{smallmatrix}6 & 4\\ 2 & 6\end{smallmatrix}\right)$-superstructure on Au(111). The three molecules in a unit cell are aligned in the structure that yields the best energy per area. The three molecular orientations are marked by black and white triangles indicating the different on-surface chirality and orientations. The substrate surface basis vectors v_1 and v_2 are indicated. To display the different atom sizes the used radii are 1.2 times the respective covalent radii [160].

atoms are indicated in gray, nitrogen atoms in blue, oxygen atoms in red, and hydrogen atoms in white. The gold substrate atoms are colored in yellow. The surface basis vectors of the gold substrate v_1 and v_2 are indicated on the right. Additionally, the chemical structure of a single caffeine molecule is shown on the right as an overlay to connect the two representations.

The geometry optimization of the selected structure, which is shown in figure 6.11, reveals an adsorption energy of about $-1.1\,\mathrm{eV}$ per caffeine molecule. This energy is within the expected range for physisorption of molecules of this size [53, 157]. Note that due to the tight-packing constraint the energetically most favorable pairs are not necessarily part of the best densely packed structure as the energy of a full monolayer is minimized. Furthermore, the found structure is a heterochiral arrangement of caffeine molecules, which exhibit the most energetically favorable structure. The ratio of the two chiralities of

caffeine molecules on the surface is 1:2 and vice versa for the mirrored domain. Therefore, each domain exhibits a non-racemic arrangement. The three molecular orientations are indicated by black and white triangles, showing the two different chiralities on the surface and the different orientations of the molecules. In addition, the single molecular and the three molecular unit cells are shown in blue and orange, respectively. Moreover, the structure did not change significantly during the geometry optimization, which supports the applicability of the two-step approach. For more details, the full simulation results are available for free via the NOMAD database at [161].

Kinetic diffraction simulation

Since the monolayer simulation is in favor of the three-molecule unit cell and the LEED results are not, a further analysis is needed. The three times larger unit cell should show additional spots in the LEED pattern as indicated in figure 6.9. In order to find an explanation, a diffraction simulation based on the proposed three molecular unit cell is presented in this section.

The kinetic diffraction simulation allows to simulate the diffraction pattern of a given geometry. Specifically, the location and intensity of the peaks are calculated using the square of the structure factors which is:

$$n_{\vec{G}} = \sum_{\text{atoms}} f_{\text{atom}}(\vec{G}) \times \exp\left(-i\vec{G}\vec{r}\right) \tag{6.5}$$

where $\vec{G}$ and $\vec{r}$ are the reciprocal lattice vectors of the crystal and the location of the atoms in the unit cell, respectively. Furthermore, the atomic form factors are calculated with

$$f_{\text{atom}}(\vec{G}) = \sum_{i=1}^{n} a_i \exp\left(-b_i \left(\frac{\vec{G}}{4\pi}\right)^2\right) \tag{6.6}$$

where a_i and b_i are taken from [162].

In this simulation, the geometry of the proposed three molecular unit cell shown in figure 6.11 is used and modeled as a free-standing monolayer thus neglecting the substrate. The resulting diffraction pattern is shown in figure 6.12 (c). There, the intensity of each spot is indicated with green circles and the size of the peaks represents the calculated diffraction intensity. The simulation shows that despite the unit cell being three times larger, the additional spots have a much lower intensity than the spots of the nearest neighbor pattern. Hence, the first-order spots for the $\left(\begin{smallmatrix} 6 & 4 \\ 2 & 6 \end{smallmatrix}\right)$-structure are weaker with an intensity ratio of about $1 : 33$ compared to the strong spots corresponding to the first order

of a $\begin{pmatrix} 10/3 & 2/3 \\ 8/3 & 10/3 \end{pmatrix}$-cell. Therefore, the diffraction simulation suggests that the periodicity of the surface structure follows the primitive cell, rather than the three-molecule super cell. For better comparison, a LEED image is shown in figure 6.12 (a) and in figure 6.12 (b) the simulated pattern is printed on top of the LEED image.

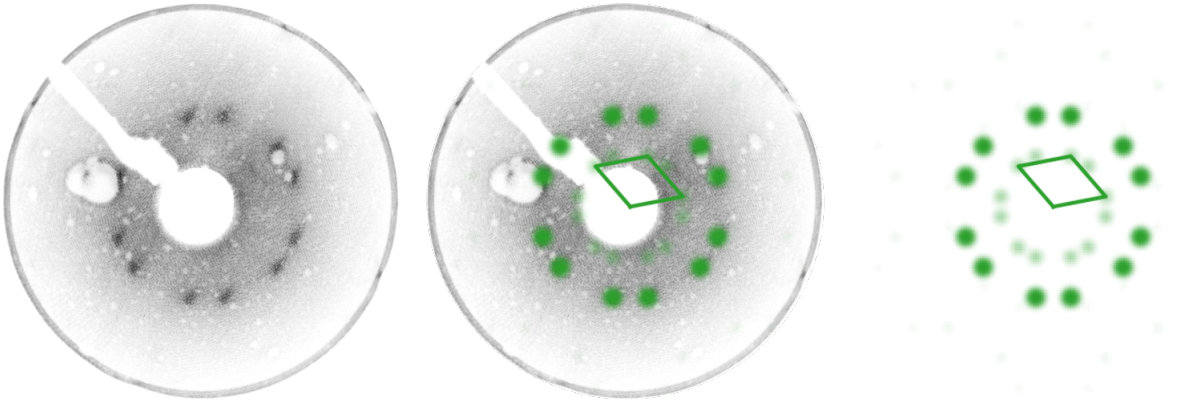

(a) LEED image: $E_{kin} = 20\,eV$. **(b)** Superposition of (a) and (c). **(c)** Simulated pattern.

Figure 6.12: Representation of the kinetic diffraction simulation of the three molecular structure shown in figure 6.11 in comparison with a measured LEED pattern. (a) LEED pattern of caffeine/Au(111) at $E_{kin} = 20\,eV$. (b) The calculated intensity is plotted in green on top of the measured LEED pattern shown in (a). (c) The intensity of the calculated diffraction patterns shown alone in green.

It should be noted that this kinetic diffraction simulation is not a LEED simulation because it neglects multiple scattering and substrate gold atoms. Therefore, the electron kinetic energy does not change the intensity ratio. Nevertheless, the result is a good approximation and shows that the intensity of the three molecular spots is significantly reduced. Within the measurement apparatus used, this difference is not resolvable due to background noise, beam damage, and possible interference charges. Especially, since the caffeine film LEED pattern is only detectable below $E_{kin} = 30\,eV$.

Therefore, the hypothesis of a three-molecule unit cell is in agreement with the LEED results within the limits of the measurement equipment. In addition, it is not excluded that the unit cell could be much larger. The simulation estimated the most favorable alignment inside the given three molecule unit cell. If the molecules in the dense monolayer are aligned in more crystallographic orientations and form a larger higher-order commensurable unit cell, the simulation could have found a different structure. However, this assumption is outside the scope of the used techniques. The here reported structure is the smallest higher-order commensurable unit cell consistent with the experimental LEED and STM data.

The hypothesis with three molecules per unit cell is also consistent with previous studies of caffeine in the high-temperature polymorph α-phase [20, 47]. Derollez *et al.* proposed a structure for α-caffeine in a trigonal bulk crystal involving a dynamically disordered relationship of caffeine molecules in an R3c space group unit cell. The estimated parameters of the trigonal unit cell are $a = 14.94\,\text{Å}$ and $c = 6.90\,\text{Å}$ [47]. Their proposed lattice constant is in excellent agreement with the estimate of the three molecular lattice constant of $a' = 15.2\,\text{Å}$. In the unit cell, they assumed two quasi-hexagonal layers of caffeine molecules with a height difference of $\pm c/6$ for alternating molecules in one layer. This height difference is not expected for a monolayer and no evidence was found in the presented measurements. The previously estimated molecule nearest-neighbor distance of $(8.6 \pm 0.3)\,\text{Å}$ suggested by the STM and LEED data is in agreement with the three-molecule unit cell model, since there is a uniform distribution of molecules within the unit cell. In order to test the proposed unit cell with a complementary method, XPS measurements of the system are conducted and presented in the next section. The results are compared with the energy states calculated within the DFT calculations as they yield information about the electronic structure.

6.3 Core-level photoemission spectroscopy

XPS measurements at DELTA are performed in order to study the surface and intermolecular interactions. Furthermore, they allow to compare experimental data of the C 1s, N 1s, and O 1s core-levels with the calculated energies of the DFT simulation in order to validate the proposed structure of a weakly interacting caffeine monolayer. In the first section of this part, the sample preparation is documented with survey spectra and LEED patterns. Then, the Au 4f orbital spectra are presented in more detail to compare the pristine surface and the adsorbed caffeine monolayer film. Thereafter, the core-level energies of the unit cell atoms estimated from DFT are presented, which are compared with the experimental high-resolution C 1s, N 1s, and O 1s spectra.

6.3.1 Sample preparation

To conduct photoemission experiments a Au(111) crystal is prepared at the UHV chamber located at the DELTA facility as described in section 5.1. The preparation of the clean Au(111) surface is verified by a XP survey spectrum at $h\nu = 650\,\mathrm{eV}$ with an emission angle of $\Theta = 60°$. The spectrum is shown in figure 6.13 (a) and reveals that no carbon, oxygen, or nitrogen contamination are present. Prominently, the Au 4f and Au 3d signals are visible

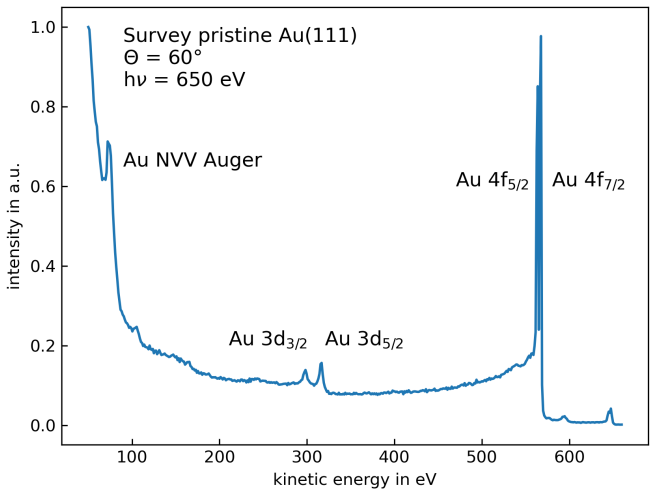

(a) Survey $h\nu = 650\,\mathrm{eV}$, $\Theta = 60°$.

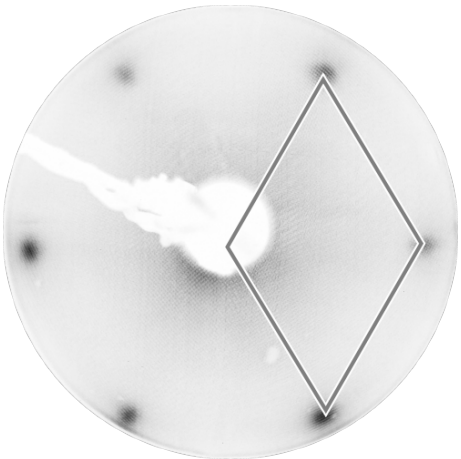

(b) $E_{\mathrm{kin}} = 55\,\mathrm{eV}$.

Figure 6.13: Documentation of the preparation of clean Au(111). (a) The survey spectrum at an emission angle of 60° shows no sample contamination and the expected gold signals are visible. (b) The LEED image shows successful reconstruction of the sample surface.

as well as the Au NVV Auger transition at $E_{\text{kin}} = 70\,\text{eV}$ [163]. Furthermore, the Au(111) surface reconstruction is checked with a LEED measurement shown in figure 6.13 (b).

After the substrate preparation the caffeine monolayer on top is prepared as described in section 5.2. The survey spectrum in figure 6.14 (a) and the well reproduced LEED pattern in figure 6.14 (b) reveal a successful monolayer preparation. The survey shows the distinct peaks of the C 1s, N 1s, and O 1s signals indicating the successful deposition of a monolayer film. The priority during the DELTA shifts is to achieve optimal XPS results. Therefore, to minimize beam damage effects in the XPS signals the LEED pattern is measured after several XPS measurements which could explain some of the noise. Furthermore, this indicates that the monolayer film does not disintegrate completely due to the synchrotron radiation beam. Noting, that the synchrotron beam spot is smaller than $100\,\mu\text{m} \times 30\,\mu\text{m}$ [129] and the LEED spot size is roughly smaller than 1 mm in diameter. Hence, the LEED measurement averages over a much larger area than the XPS experiment.

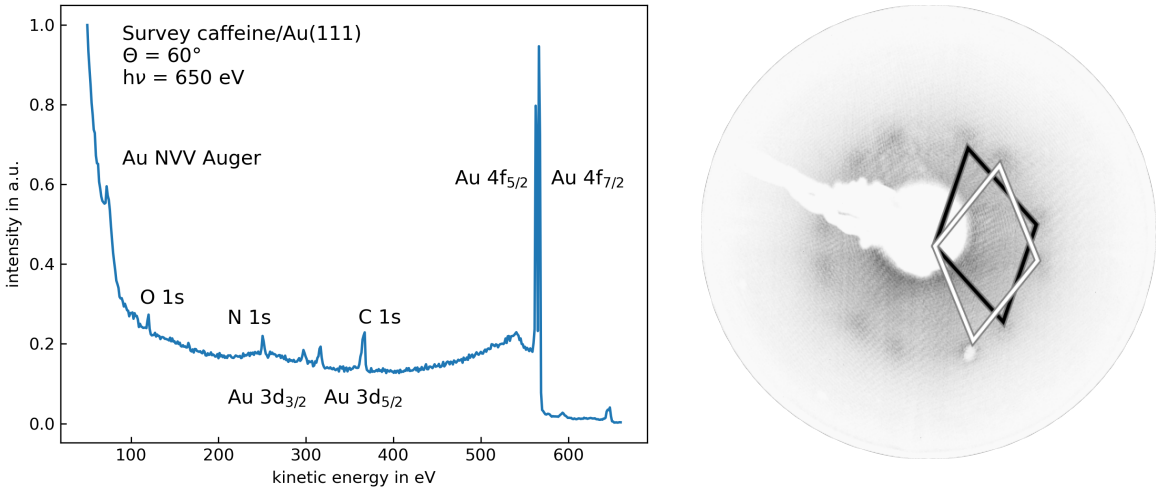

(a) Survey $h\nu = 650\,\text{eV}$, $\Theta = 60°$.

(b) $E_{\text{kin}} = 20\,\text{eV}$.

Figure 6.14: Documentation of the preparation of the caffeine monolayer on Au(111). (a) The survey spectrum at an emission angle of 60° shows all expected signals from the caffeine molecules (O 1s, N 1s, C 1s) and the gold signals were also visible. (b) The LEED image shows all twelve spots of the dense caffeine monolayer and thus a successful preparation.

6.3.2 High-resolution Au 4f spectra

In a further analysis, the Au 4f orbital is studied in more detail. The high-resolution spectra of this orbital is measured with an exciting photon energy of $h\nu = 340\,\mathrm{eV}$ and is shown in figure 6.15. The left side of the figure shows the spectra of the pristine Au(111) surface and the right side with caffeine on top. The spectra shown on top are measured at an emission angle of 0° and on the bottom at 60°. All Au 4f signals are fitted by applying a convolution of a Doniach-Sunjic, a Gaussian-function, and a Tougaard background. The 4f signal consists of a doublet representing the spin-orbit splitting into Au $4f_{5/2}$ and Au $4f_{7/2}$ states with an area ratio of 3:4 and an energy difference of $\Delta E_{\mathrm{SOC}} = 3.67\,\mathrm{eV}$ [164]. Each signal consists of two doublet components. The two components are attributed to two chemical environments as these affect the binding energy of the individual atoms. One component is attributed to the bulk signal, shown here in dark green, while the surface component is represented in light green. The surface core-level shift between these two components is estimated to be $\Delta E_{\mathrm{S}} = 0.31\,\mathrm{eV}$ towards a higher kinetic energy for the surface component which is in excellent agreement with literature [165, 166]. The bulk $4f_{7/2}$ component is recorded at a kinetic energy of $E_{\mathrm{kin}} = 251.88\,\mathrm{eV}$ in all measurements.

The normal emission Au 4f signals of the clean Au(111) and the caffeine/Au(111) sample are compared in figure 6.15(a) and (b), respectively. The background level increases without a significant change in the kinetic energies of the 4f electron states. The full width at half maximum (FWHM) for the normal emission peaks is in the range of $\Delta E = 0.53{-}0.54\,\mathrm{eV}$ with an asymmetry factor of 0.031 and 0.04 for the clean and the caffeine covered sample, respectively, which is in accordance to literature [167]. The peak area of the surface component changes from 37.2% to 39.5% for the clean and caffeine monolayer surface, respectively. The more surface sensitive measurement recorded at $\Theta = 60°$ are shown in figure 6.15 (c) and (d). For these peaks FWHM is in the range of $\Delta E = 0.55{-}0.57\,\mathrm{eV}$ with an asymmetry factor of 0.043 and 0.065 for the clean and the caffeine covered sample, respectively. The surface component of the clean sample amounts to 43.6% of the total signal area, while for the monolayer sample a surface component of 43.5% was found. The difference in the surface component values is not significant. The surface sensitive measurement shows the expected increase of the surface component of about 15% due to the decreased information depth. A slight increase of the peak asymmetry due to the impact of the molecular film, and no additional component is detected in the signal.

Additionally, the measured Au 4f spectra can be used to roughly calculate the adsorbate layer thickness with a simple approximation. For this method described in [168] the normalized counts of a substrate signal I, in this case the Au 4f signal, is estimated for the clean surface and for the one with the adsorbate on top. Thus, the absolute counts of

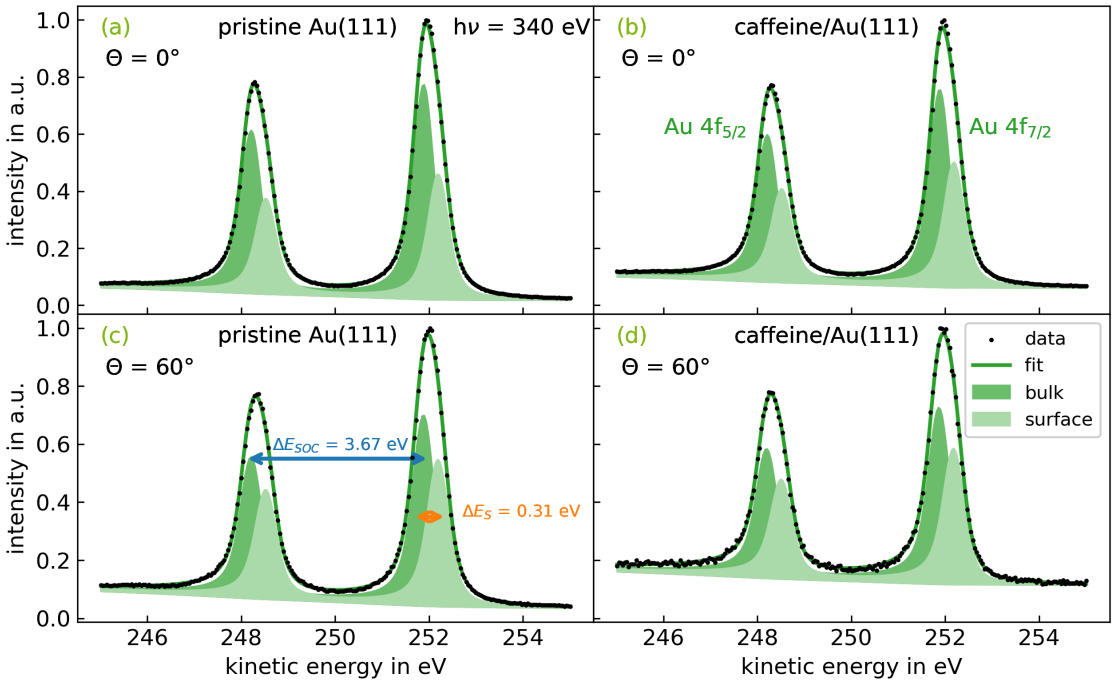

Figure 6.15: Au 4f core-level XP spectra before (left) and after caffeine deposition (right), recorded at a photon energy of $h\nu = 340\,\text{eV}$ and emission angles of $\Theta = 0°$ (top) and $\Theta = 60°$ (bottom). The dark green component corresponds to the bulk signal and the surface component is represented in light green.

the Au 4f signal are divided by the number of measurement sweeps and the logged beam current to obtain the normalized counts I. With this information, the emission angle Θ, and the IMFP of the adsorbate λ_{ads} the film thickness can be calculated via [121]:

$$I_{\text{clean},\Theta} = I_{\text{adsorbate},\Theta} \exp\left(-\frac{d_\Theta}{\lambda_{\text{ads}} \cos\Theta}\right) \tag{6.7}$$

An approximation of the IMFP of electrons with a kinetic energy of $E_{\text{kin}} \approx 250\,\text{eV}$ in caffeine is roughly estimated to be $\lambda_{ads} \approx 10.5\,\text{Å}$. This is the IMFP of electrons with $E_{\text{kin}} \approx 250\,\text{eV}$ in adenine layers which are similar to caffeine and the IMFP in organic molecules does not differ much in this energy range [169]. With these rough estimations the thickness of the caffeine monolayer film is estimated to $d_{0°} \approx 3.5\,\text{Å}$ and $d_{60°} \approx 4.5\,\text{Å}$. As the monolayer height is approximated with 3.45 Å this results in a coverage of 1 ML to 1.3 ML, which is consistent with the layer thickness determined by QCM in 5.2 and STM in 6.2.1. Noting, that this method of film thickness determination is prone to errors in the order of ±50 % [170]. Nevertheless, it shows the reproducible preparation method.

In conclusion, the kinetic energy of the gold core electron levels does not shift with the deposition of caffeine molecules and no new components are visible in the Au signals. Consequently, no strong chemical bonding between the caffeine molecules and the gold surface atoms could be documented. Noting, that an effect should be small since there are about 3 caffeine molecules per 28 Au surface atoms. Therefore, more weight is on the surface sensitive measurement at an emission angle of 60°, and again no change in the Au 4f signal is visible. Moreover, the monolayer thickness of the prepared sample is perfectly reproduced. The next sections focus on the analysis of the caffeine monolayer and thus on the spectra of the carbon, nitrogen, and oxygen atoms present in the caffeine molecule, respectively. Additionally, the core-level energies retrieved from the DFT simulation are presented and compared with the experimental results.

6.3.3 Adsorbate core-levels

All information associated with the analysis of the core-level energies are presented here. Starting with the results of the simulated core-level energies obtained by DFT. Thereafter, these energies are compared with the experimentally obtained high-resolution XPS measurements.

Simulated core-level energies

In this section, the estimated core-level energies are presented. Since the core-level energies of all atoms in the unit cell are estimated as part of the performed DFT simulation, it is possible to compare them with the experimental results. Due to the fact that the unit cell consists of three molecules in different orientations, the binding energies of equivalent atoms within a caffeine molecule differ slightly and are therefore grouped into chemically related components. For this purpose, the groups are formed from three estimated core-level energies, which are then assigned to one atom of a single caffeine molecule. The assignment is based on the XPS results published by Plekan *et al.* [171] of caffeine molecules in gas phase, and the assumption that molecule-molecule interactions do not change the core-level energies substantially. Thus, the assignment to individual atoms is given to increase interpretability and may be incorrect for energy levels that are close to each other. The classification and all core energy levels are shown in table 6.2. The atom labels are consistent with figure 6.16. The assignment to measurable components is represented by separating horizontal lines and is quite stable with difference energies above 0.5 eV between the most extreme energy levels of the individual components in the carbon signal. In comparison, the energy differences of the energy levels associated with an atom are

Table 6.2: Core-level energies and averaged core-level energies (mean) of the adsorbate simulation for the C 1s, N 1s, and O 1s core-levels given in eV. The reference energy of the simulation is the vacuum level, which is 4.50 eV above the Fermi level. All core-levels in one segment, which are separated by a horizontal line, are averaged and the mean value is given in the next column. The atom labels are consistent with figure 6.16 and 2.1

C 1s	core-level / eV	mean / eV	N 1s	core-level / eV	mean / eV	O 1s	core-level / eV	mean / eV
	-270.50			-381.99			-511.20	
C10	-270.56		N9	-382.00	-382.05	O13	-511.27	-511.25
	-270.73			-382.15			-511.28	
	-270.86			-383.40			-511.30	
C12	-270.94		N1	-383.46	-383.46	O11	-511.31	-511.33
	-270.97	Comp. A		-383.51			-511.39	
	-271.01	-270.96		-383.62				
C5	-271.05		N3	-383.67	-383.66			
	-271.10			-383.69				
	-271.24			-384.02				
C14	-271.27		N7	-384.02	-384.06			
	-271.31			-384.13				
	-271.95							
C8	-272.01							
	-272.13	Comp. B						
	-272.15	-272.11						
C4	-272.16							
	-272.23							
	-273.07	Comp. C						
C6	-273.09	-273.09						
	-273.10							
	-273.61	Comp. D						
C2	-273.68	-273.69						
	-273.76							

below 0.3 eV. For nitrogen the difference of the energy levels is smaller but significant and for oxygen it is not possible to really distinguish between the two different atoms in the simulation and neither in the experiment as shown later. Hence, there the assignment is only given to illustrate the used method. Additionally, all core-levels assigned to one component, which are separated by a horizontal line, are averaged and the mean value is given in the next column for a further comparison to the experimental data.

In order to obtain a spectrum of the here presented energy levels, each energy position is visualized by a Voigt-profile at that energy with respective Gaussian- and Lorentzian-parameters in accordance with the experiment. Thus, the resulting simulation spectrum is a superposition of all simulated molecular core-levels. The experimental XPS measurements are compared with the molecular core-levels of the initial-state approximation. This assumes that the relative core-level eigenvalue shifts of the undisturbed system correspond to the relative XPS peak shifts. Moreover, surface effects are assumed to act on all atoms in

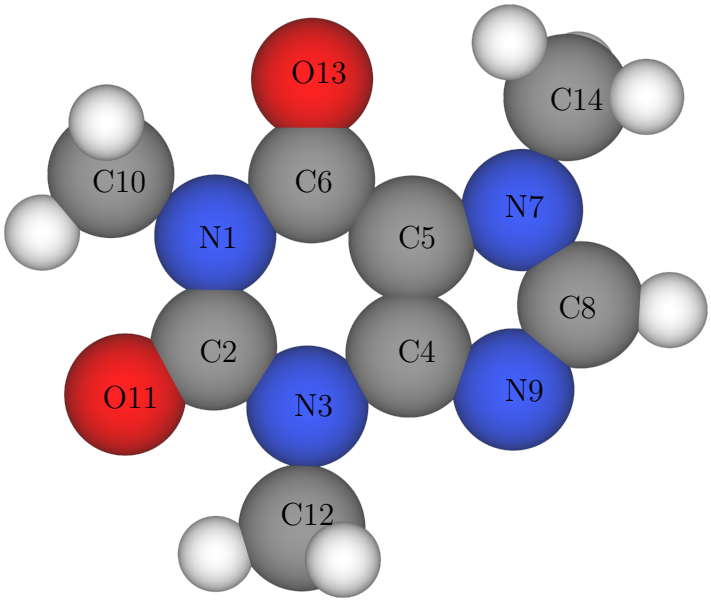

Figure 6.16: Recap of the figure 2.1 for a better comparison with the XPS results. Molecular structure of caffeine ($C_8H_{10}N_4O_2$) and assignment of numbers to atoms within the molecule. Carbon (C) atoms are shown in gray, nitrogen (N) in blue, oxygen (O) in red, and hydrogen (H) in white.

the same way. To compensate for differences in the measured work function and the vacuum level of the simulation, the energy average of the component with the highest energy is aligned with the measured component with the highest kinetic energy. This method also allows an easy and fast comparison of relative shifts of single components [172].

High-resolution C 1s spectrum

The spectrum of the carbon C 1s orbital, which consists of several components is shown in the upper part of figure 6.17. The spectrum is recorded with a photon energy of $h\nu = 340\,\text{eV}$ at normal emission. In order to minimize beam damage effects, the shown spectrum is a superposition of ten measurement sweeps, and each sweep is obtained from a slightly different position of the sample surface. Thus, the manipulator is moved 100 µm for each sweep, which is sufficient to measure a new sample area [129]. The measurement time constant was set to 900 ms for each step and the spectrum is obtained with a step width of 0.041 eV. The pass energy of the spectrometer is set to 5.85 eV.

A fitting procedure is applied to the measured spectrum using a Tougard background, which is subtracted from the data for better comparisons. Five components are sufficient to reproduce the line shape as measured. In addition, the simulation results show that

four components could be identified and separated as described previously, and are shown in the lower part of the figure 6.17. Each component in the simulation spectrum shows the superposition of the core-level energies broadened with Voigt-profiles associated with each component. Therefore, the line shape of the four simulated components may differ from individual Voigt profiles centered on the mean energy. Nevertheless, the components are in accordance with the experiment.

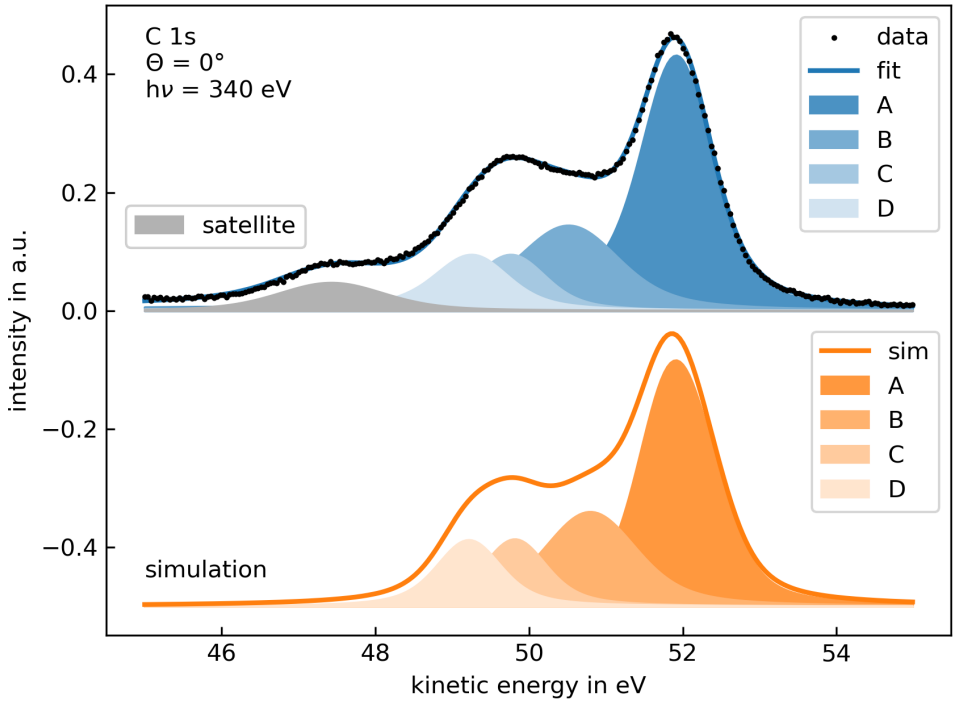

Figure 6.17: C 1s core-level XPS of caffeine on Au(111) recorded at a photon energy of $h\nu = 340\,\text{eV}$ and at an emission angle of $\Theta = 0°$. In the bottom panel, the simulated XP spectrum of the caffeine monolayer is shown. The assignment of the carbon atoms to the components A, B, C, and D is shown in table 6.3.

The fitting results for each peak are presented in table 6.3. There, the kinetic energies, peak area ratios, FWHM, and asymmetry factors α are shown. Furthermore, a short recap of the associated simulation components and their respective relative energies is given, as well as the assignment to single atoms of the caffeine molecule.

The main component of the carbon C 1s orbital is here referred to as A and represents four of the eight carbon atoms in the caffeine molecules. It is located at a kinetic energy of $E_{\text{kin}} = 51.94\,\text{eV}$ with $\Delta E = 1.1\,\text{eV}$ FWHM, an asymmetry factor of $\alpha = 0.05$. The peak area ratio is about 50 %, which is consistent with the assignment within the molecule.

Three of the four carbon atoms - C10, C12, C14 - are located in the three methyl groups of trimethylxanthine. The fourth - C5 - is located in the middle of the molecule and is bonded to two carbon atoms and one nitrogen atom. Plekan *et al.* [171] showed that these four energy levels are very close to each other and they were not separable in both DFT simulations and measurement. In addition, the effects of beam damage were mostly visible in a decreased intensity of this component. One possible explanation is that the methyl groups are susceptible to beam damage and then sublime from the surface [173, 174].

Table 6.3: Energies of the C 1s signal components of the XPS experiment in comparison with the averaged adsorbate simulation results. The reference energy of the simulation is the vacuum level, which itself is 4.50 eV above the Fermi level. Discrepancies in relative kinetic energy may be due to rounding errors.

		Experiment				Simulation	
Orbital	Component	kin. energy / eV	area / %	FWHM / eV	α	rel. kin. energy / eV	Atoms
C 1s	A	51.94	49	1.1	0.05	-270.96	C5,10,12,14
$h\nu = 340\,\text{eV}$	B	-1.39	23	1.6	0.05	-1.14	C4,8
	C	-2.15	10	1.1	0.05	-2.12	C6
	D	-2.66	11	1.2	0.05	-2.72	C2
	$\pi \rightarrow \pi^*$	-4.51	7	1.7	0.07		

Component B has a kinetic energy lower than component A by $\Delta E = -1.39\,\text{eV}$. This component is assigned to carbon atoms C4 and C8, both of which are bonded to two nitrogen atoms. Furthermore, C4 is bonded to another carbon atom C5 and C8 is bonded to a hydrogen atom. The calculated difference between the peaks of component A and B is 0.25 eV lower than in the experiment. In addition, the FWHM found for this component is increased by 0.5 eV compared to the other C 1s components. It is possible that the energy difference between the two atoms, or the six atoms in the unit cell, is larger than expected and more evenly distributed in this energy range. Another possibility is that the interactions of C8 with oxygen atoms of other caffeine molecules have an effect on this component and broaden these energy levels [172]. Independent components for each atom do not yield a significantly better fit, and the energy difference calculated in the simulation for C4 and C8 did not justify separation into two components and is therefore omitted.

Furthermore, the components C and D are assigned to the carbon atoms C6 and C2, respectively. Both atoms are double bonded to an oxygen atom, C2 is additionally single bonded to two nitrogen atoms and C6 is additionally single bonded to a nitrogen and a carbon atom. The calculated energy differences of components C and D with respect to A agree within 0.1 eV with the experimental analysis. Both components accounts for about 10 % of the measured signal which is in perfect accordance with the simulation.

One component could not be explained by the DFT simulation which is found at significantly lower kinetic energies. In the fitting procedure this component is found at $\Delta E_{\pi\to\pi^*} = -4.51\,\mathrm{eV}$ relative to component A with a FWHM of 1.7 eV an asymmetry of $\alpha = 0.07$, and an amount of 7% of the complete signal. This satellite peak is associated with a $\pi \to \pi^*$-transition which is common in organic adsorbate XPS [175, 176]. In several studies the HOMO/LUMO gap of freestanding caffeine is found to be in the range of 3.37 eV to 3.93 eV [30, 177, 178]. Additionally, the adsorption of a molecule on a metal surface influences and broadens its orbitals by direct coupling to the electronic states of the substrate and also electronic coupling of different molecular states through the surface which could increase the measured gap [179, 180]. Moreover, in cocrystallization like the caffeine−glutaric acid cocrystals the HOMO-LUMO gap increases to ∼5.1 eV [181]. Since the measured excited state is relatively broad and was found at $\Delta E_{\pi\to\pi^*} = -4.51\,\mathrm{eV}$ lower kinetic energy than component A, it could be a superposition of the mentioned effects.

High-resolution N 1s spectrum

The analysis of the N 1s orbital is equivalent to the C 1s. To account for lower beam intensities at higher photon energies the spectrum is obtained with a step width of 0.123 eV and the pass energy of the spectrometer is set to 11.71 eV.

The N 1s signal recorded at a photon energy of $h\nu = 500\,\mathrm{eV}$ is displayed in figure 6.18. The spectrum consists of four components, corresponding to the four nitrogen atoms of the molecule. Each component amounts to ∼25% of the signal area, with a FWHM of ∼1.4 eV, and an asymmetry factor of $\alpha \sim 0.02$. The N9-component is found at a kinetic energy of 97.33 eV, while N1, N3, and N7 are shifted by $\Delta E_{\mathrm{N1}} = -1.21\,\mathrm{eV}$, $\Delta E_{\mathrm{N3}} = -1.89\,\mathrm{eV}$, and $\Delta E_{\mathrm{N7}} = -2.26\,\mathrm{eV}$ towards lower binding energies, respectively. The details are shown in table 6.4. In comparison to gas-phase caffeine, the FWHM values are increased as expected [182]. The comparison of the experimental data to the simulation shows a well reproduced line shape and overall good agreement.

The energy difference between the simulated components N1, N3, and N7 is smaller than the measured experimental difference between those components. The signals of N1 and N7 are separated by 0.60 eV in the simulated data and by 1.05 eV in the experiment. This could explain the increased width of component B in the C 1s signal since the C4 and C8 atoms are bonded with the N3/N9 and N7/N9 atoms, respectively. Moreover, no further exited state is detectable in the N 1s signal which might be attributed to the overall decreased intensity.

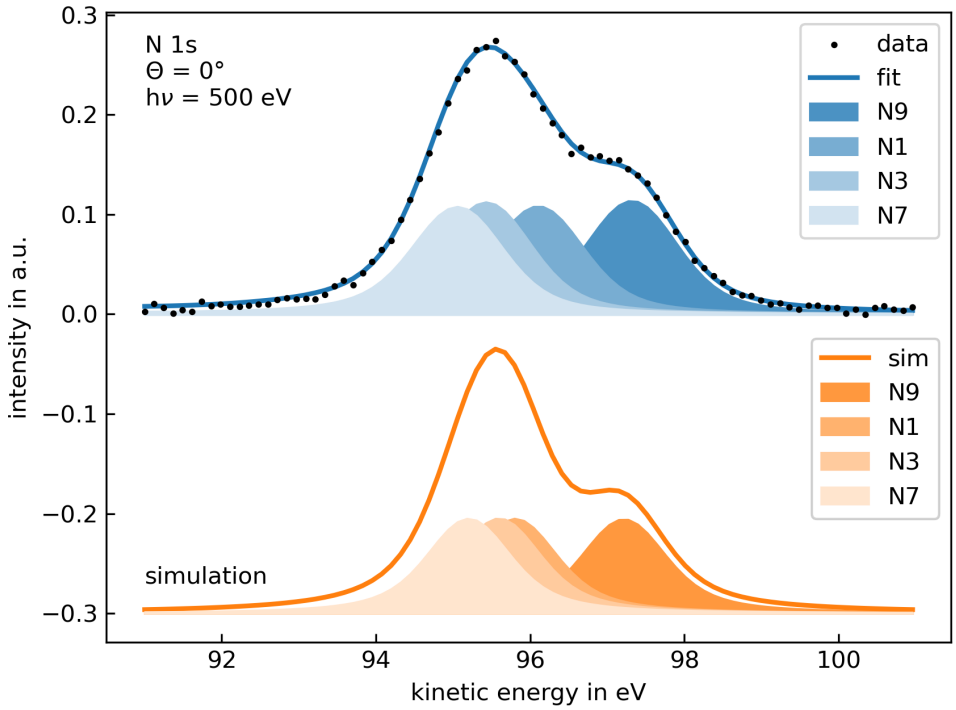

Figure 6.18: N 1s core-level XPS of caffeine on Au(111) recorded at a photon energy of $h\nu = 500\,\text{eV}$ and at an emission angle of $\Theta = 0°$. The simulated XP spectrum of the caffeine monolayer is shown in the bottom panel.

Table 6.4: Energies of the N 1s signal components of the XPS experiment in comparison with the averaged adsorbate simulation results. The reference energy of the simulation is the vacuum level, 4.50 eV above the Fermi level. Deviations in relative kinetic energy may be due to rounding errors.

		Experiment				Simulation	
Orbital	Component	kin. energy / eV	area / %	FWHM / eV	α	rel. kin. energy / eV	Atoms
N 1s	N9	97.33	26	1.42	0.02	-382.05	N9
$h\nu = 500\,\text{eV}$	N1	-1.21	25	1.41	0.02	-1.41	N1
	N3	-1.89	25	1.41	0.02	-1.62	N3
	N7	-2.26	24	1.41	0.02	-2.01	N7

High-resolution O 1s spectrum

Additionally, the oxygen O 1s signal is recorded at a photon energy of $h\nu = 650\,\text{eV}$, as shown in figure 6.19. The spectrum is obtained with a step width of 0.123 eV and the pass energy of the spectrometer is set to 11.71 eV.

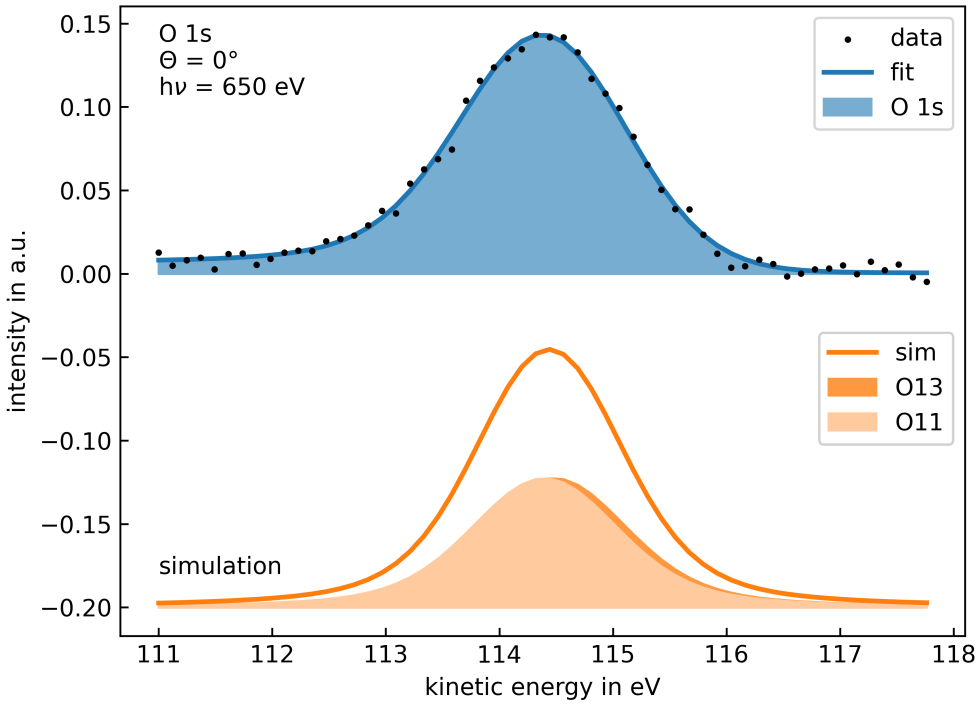

Figure 6.19: O 1s core-level XPS of caffeine on Au(111) recorded at a photon energy of $h\nu = 650\,\text{eV}$ and at an emission angle of $\Theta = 0°$. The bottom panel shows the simulated XP spectrum of the caffeine monolayer.

The individual signals of the two oxygen atoms could not be resolved separately in the spectrum, so that only one component is observed. This component is located at a kinetic energy of $E_{\text{kin}} = 114.44\,\text{eV}$ with $\Delta E = 1.8\,\text{eV}$ FWHM, and an asymmetry factor of $\alpha = 0.08$. The details are shown in tabular 6.5. Moreover, the energy difference between the two calculated components in the simulation is small with $\Delta E_{\text{O11}} = -0.08\,\text{eV}$ and therefore is not expected to be resolved in the experiment. Moreover, no effect of different bonding environments, such as hydrogen bonds or Watson-Crick bonds is visible [183, 184].

Table 6.5: Energies of the O 1s signal components of the XPS experiment in comparison with the averaged adsorbate simulation results. The reference energy of the simulation is the vacuum level, which itself is 4.50 eV above the Fermi level. Deviations in relative kinetic energy may be due to rounding errors.

		Experiment	Simulation		
Orbital	Component	kin. energy / eV	relative kin. energy / eV	mean core-level / eV	Atoms
O 1s		114.44	—	-511.25	O13
$h\nu = 650\,\text{eV}$		—	-0.08	-511.33	O11

Concluding, that the XP spectra of adsorbed caffeine agree well with previous XPS results of caffeine molecules in the gas phase from Plekan *et al.* [171], and with the calculated molecular core-level energies of the DFT simulation. Accordingly, the XPS analysis shows that a physisorbed caffeine layer is present on Au(111) without covalent bonding to the substrate. This result is also indicated by the previous STM and LEED experiments.

The experimental XPS analysis shown cannot distinguish between different molecular unit cells and thus could not prove or disprove the three-molecular unit cell. However, STM, LEED and DFT, show strong evidence for a three-molecular unit cell at room temperature in a heterochiral arrangement. To further investigate the caffeine formation on Au(111) an additional structural investigation at low temperature is performed in the next chapter. There, the analysis of the dense monolayer is reproduced. Furthermore, the focus is on the investigation of submonolayer coverage and chiral structures of caffeine.

Chapter 7

Low temperature measurements

The group around PD. Dr. Daniel E. Bürgler and Dr. Frank Matthes at the Peter Grünberg Institute for Electronic Properties (PGI-6) located at the Jülich Research Centre gratefully provided measurement time at their nano-spinelectronic cluster tool (NSCT). The experimental setup is shown in section 4.2.3 and it is equipped with a low temperature STM from *Omicron*. Therefore, in this chapter the caffeine formation on gold is investigated at a different thermodynamic state at 4 K and with a potentially better resolution.

In order to conduct the analysis, this chapter is divided into two parts. First the preparation of the dense caffeine monolayer formation is reproduced and checked with LEED and STM. This data is compared with the room temperature results to ensure a reproducible sample preparation. The resolution improved significantly and intra-molecular features become visible in the STM measurements and are discussed in that section. At low temperatures the STM investigation of submonolayer coverage is feasible due to less interaction between the tip and the adsorbate molecules. Therefore, results of these measurements are presented in the second part 7.2. Moreover, formations of small locally chiral alignments of caffeine molecules are found and presented there.

7.1 Dense monolayer formation

With the support from Dr. Frank Matthes the preparation of a Au(111) crystal and the caffeine molecule evaporation is reproduced at the NSCT. The preparation parameters are near to identical to the ones shown in chapter 5 and used at the TU Dortmund University facilities.

7.1.1 Sample preparation

The generously provided Au(111) crystal is cleaned with repeated cycles of Ar^+ sputtering with a kinetic energy of $E_{kin} = 800\,eV$ and at an incidence angle of $\Theta = 45°$, followed by annealing at $T \sim 700\,°C$. The annealing period is extended to 70 min and the successful preparation of the Au(111) crystal is documented by the LEED image in figure 7.1 (a) at an kinetic electron energy of 50 eV. In addition, STM measurements of the clean surface have been presented in chapter 5.1 in figure 5.3, which also show the successful

preparation. For the caffeine deposition an evaporator is provided and the caffeine powder is carefully degassed at $\sim 70\,°C$. The evaporation is performed in the molecular deposition chamber with an filament current of 0.15 A which corresponds to a measured temperature of $T \sim 100\,°C$. The background pressure in the molecular deposition chamber raised from 1×10^{-9} mbar to 1×10^{-6} mbar prior to the deposition step. Sample preparation is performed like described in chapter 5.2 and a full monolayer coverage is achieved with a deposition time of $\sim 120\,s$. For smaller coverage shorter deposition times are used. After deposition, the samples are annealed at $\sim 80\,°C$ for 10 min to increase the mobility for an assembly process.

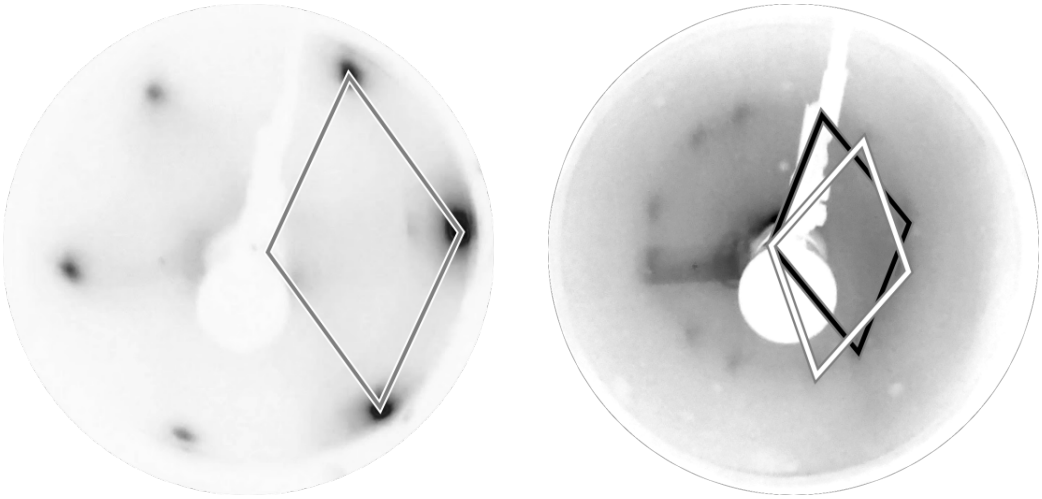

(a) $E_{kin} = 50\,eV$ - Pristine Au(111) **(b)** $E_{kin} = 15\,eV$ - Caffeine/Au(111)

Figure 7.1: Measured LEED pattern at the NSCT. (a) shows the clean substrate Au(111) crystal and (b) shows the successfully prepared caffeine monolayer film on the gold substrate.

In figure 7.2 (a) a large scale STM image at 4 K is shown. It shows two domains of dense monolayer caffeine molecules on a single Au(111) terrace and their domain border. This measurement is comparable to a measurement at room temperature shown in figure 6.5, which also reveals a domain border on a terrace. Again, the two mirrored domains are separated by a non-straight line and defects are present near the domain border. The domain border is indicated by a semi-transparent white line and the individual domains are marked with circles of a fine hexagonal net in white and black, respectively. The FFT corresponding to figure 7.2 (a) is shown in figure 7.2 (b). It displays the expected twelve molecular spots for both domains present. The bases are indicated with a individual rhombus in the corresponding color of the marked domains in figure 7.2 (a), white and black. The line-shaped Fourier pattern of the underlying 'herringbone' reconstruction can also be seen in the center of figure 7.2 (b), showing the well-reconstructed Au(111) substrate.

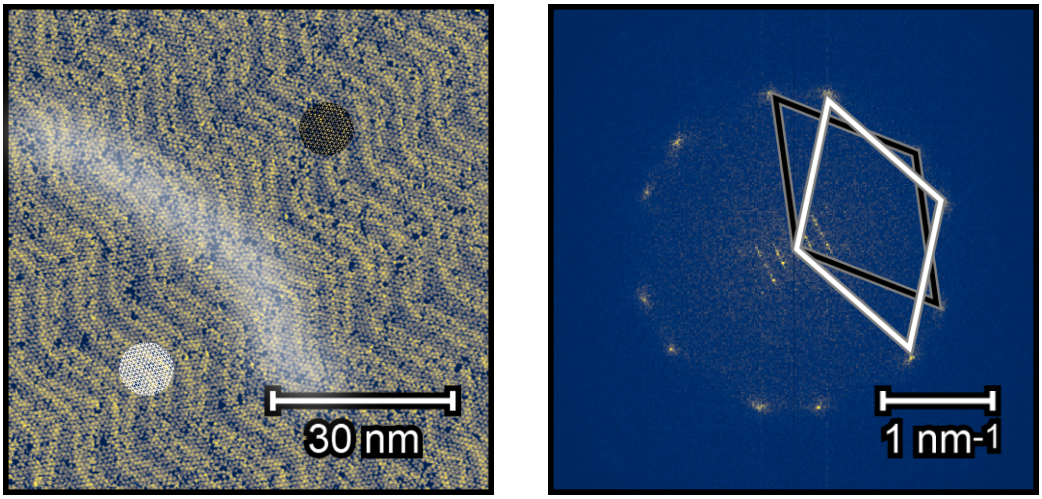

(a) LT STM - two domains of caffeine/Au(111) **(b)** FFT of 7.2 (a)

Figure 7.2: (a) STM image of caffeine monolayer on Au(111) taken at 4 K. Both mirrored domains are present and separated by a semi-transparent white line. (80×80 nm, 100 pA, -0.3 V). (b) Fast-Fourier Transform of (a) with 12 spots visible of the molecular film. In the center the Fourier-pattern of the underlying 'herringbone'-reconstruction is visible.

Both domains are also evenly distributed over the sample surface in the low temperature measurements. The mean nearest neighbor distance of the dense monolayer film across the low temperature measurements is estimated to be $a = (8.3 \pm 0.4)$ Å. This value is in good agreement with the estimates of the room temperature measurements of (8.6 ± 0.3) Å and (8.7 ± 0.9) Å presented previously for LEED and STM, respectively. A decrease in the gold lattice constant in the order of 0.5% is expected when cooling from room temperature to low temperature [185]. Therefore, the monolayer formation of the caffeine molecules is well reproduced at low temperatures compared to the room temperature data shown in chapter 6.

7.1.2 Intra-molecule resolution

The use of LT-STM at lower temperatures, also allows to resolve the intra-molecular structures of caffeine molecules in STM-measurements. In the RT-STM measurements, round, bulb like shapes of individual caffeine molecules were found as shown in chapter 6.2.1. In contrast, a triangular shape is observed with LT-STM. In figure 7.2 (a) the triangular shape can only be presumed, but is more clearly visible in figure 7.3 (a). The triangular shape reproduces the electron density of the three methyl groups of the caffeine (1,3,7-trimethylxanthine) molecule as shown in figure 6.16. This is also consistent with previous STM studies of caffeine molecules on copper and theophylline on Au(111) [186, 187].

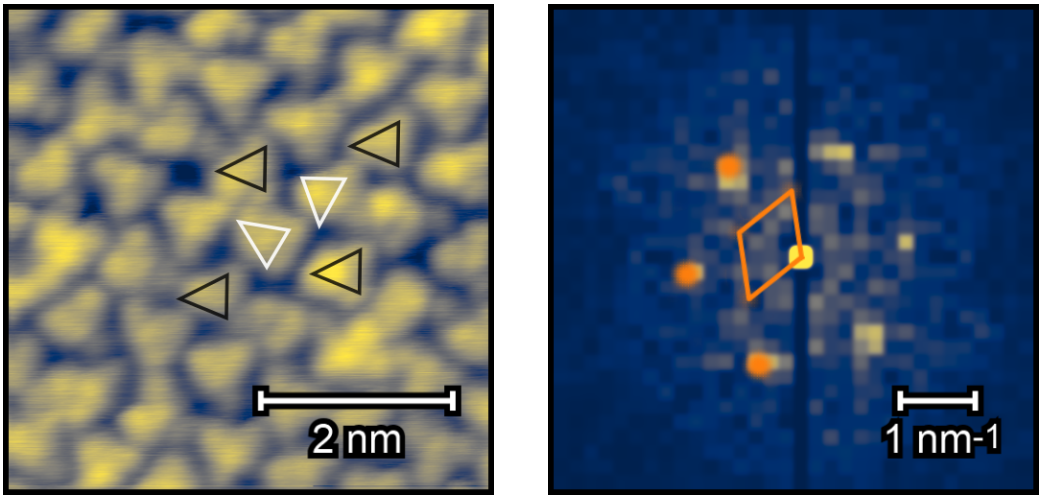

(a) (b)

Figure 7.3: (a) STM image of one domain of caffeine monolayer on Au(111) taken at 4 K. Six triangles marking individual caffeine molecules are indicated as a possible unit cell as proposed for the room temperature structure. (5×5 nm, 50 pA, -1.0 V). (b) Fast-Fourier Transform of (a) to which a weak Gaussian filter is applied. The figure shows the hexagonal pattern of the molecular film. The simulated pattern of the three-molecule unit cell is shown in orange on the left side.

Figure 7.3 (a) shows a high-resolution STM image of the caffeine film at low temperatures. Individual caffeine molecules are visible in a triangular shape. The triangles associated with individual molecules have different side length, which might be used to determine the orientation or chirality of each molecule. Moreover, small circular protrusions are present at the triangle apexes of some caffeine molecules. Possibly, they indicate the methyl groups of a caffeine molecule and they move slightly, as the form of individual molecules differ from each other. The triangular shape is indicated via six triangles aligned in the three-molecular unit cell structure previously proposed for the dense monolayer (see figure 6.11). Black and white triangles indicate a possibly different prochiral alignment of individual molecules. The side lengths of the individual molecules are different and often distorted in addition to the moving methyl groups. Therefore, the assignment of individual molecules to a certain orientation or chirality is somewhat speculative. Moreover, deviations of the caffeine triangular alignment in comparison to the proposed unit cell structure are present in the STM measurement in figure 7.3 (a). These deviations could come from non-equilibrium effects due to a fast cooling process or defects in the local structure. The cooling process was not investigated further, since the STM is cooled first and then the sample is inserted. Therefore, this process was not experimentally accessible. As shown earlier (6.10), the differences in interaction energy between different orientations are small, so local variations due to imperfect preparation are possible.

Figure 7.3 (b) shows an enlarged FFT of figure 7.3 (a). The image is scaled up by linear interpolation to increase the number of pixels, and then a light Gaussian filter is applied to flatten the pixel transitions. In addition, the kinetic diffraction simulation pattern for one domain is shown in orange on the left side. The hexagonal spots of the nearest neighbors are well reproduced. There is more fine structure in the center of the Fourier pattern, possibly there is agreement with the simulated hexagonal diffraction pattern, but not necessarily. Moreover, the result of the kinetic diffraction simulation show that the spot intensity of the inner ring should be very low compared to the nearest neighbor spots [148]. In addition, some molecules are rotated differently than expected, so these defects cause noise that also reduces the intensity of the higher order FFT spots. And some distortion is present, which also might influence the FFT pattern. It should be noted, that this FFT image is produced near the resolution limit, which may cause some defects due to binning errors.

This suggests that the proposed three molecular unit cell may be consistent with the low temperature STM data. However, there is no strong experimental evidence for or against this hypothesis because local effects dominate the orientation of the caffeine molecules in the dense monolayer. Moreover, a dense packing order without a distinct unit cell is possible, such as a glassy state or plastic crystal, which are found in form I caffeine crystals [188]. Due to the low temperature, the mobility of the adsorbed molecules is decreased, hence it is possible that the thermodynamic equilibrium is not achieved. A longer annealing step of the deposited caffeine molecules at a more precisely defined transition temperature could increase the order in the dense monolayer formation. Due to time constraints at the facility, this effect could not be investigated, and the room temperature resolution is not sufficient to investigate this.

7.1.3 Tunneling dependencies

The successful reproduction of the results of the room temperature measurements allowed a detailed analysis of the monolayer film and intra-molecular features. To further utilize the better resolution of the LT-STM and the enhanced stability of the caffeine molecules on the gold surface, a structured analysis of the tunnel parameters is performed in this section. The analysis also helps to minimize the risk of changing tunnel conditions. Moreover, the structure of the molecules in the STM depends on the tunnel parameters [189].

Hence, the caffeine monolayer is investigated at different bias voltages. At first, the application of inverted bias voltage of $-1\,\mathrm{V}$ and $1\,\mathrm{V}$ with a tunnel current setpoint of $100\,\mathrm{pA}$ is shown in figure 7.4. The application of $-1\,\mathrm{V}$ in figure 7.4 (a) exhibits more

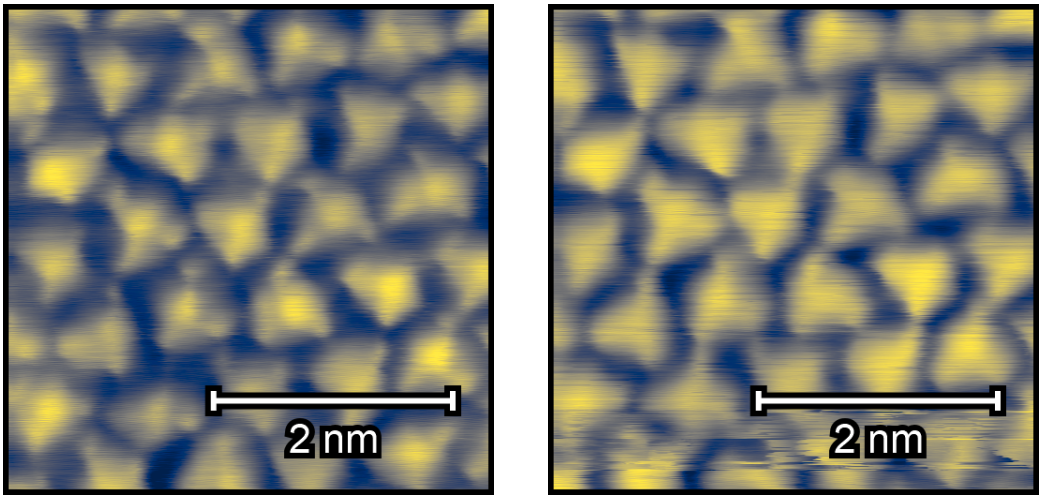

(a) -1 V (b) +1 V

Figure 7.4: Representation of inverting the applied tunnel voltage from (a) −1 V to (b) +1 V. The current setpoint is 100 pA and each measurement has a size of 4×4 nm^2.

substructure of the molecules and an overall noise reduction in comparison with the measurement at +1 V on the right 7.4 (b). This was common throughout the measurements that negative voltages obtained clearer images dependent on the tip condition.

Since a negative bias voltage results in STM images with molecule substructure, a measurement series of different setpoints for the tunneling current is performed and is shown in figure 7.5. To limit the interaction between the molecules and the tunnel tip, the maximum current setpoint is set to 100 pA. The overall shape of the molecules remains the same throughout the series in figure 7.5 - the described triangular shape with detailed protrusions on each corner. This is an indication that the tunneling orbital did not change substantially and that the images in this series are comparable upon further analysis. For very low current setpoints in the range of 10 pA to 30 pA, the images are relatively blurry and therefore are not suitable as a standard set of measurement parameters. For higher current setpoints e.g. 80 pA to 100 pA the noise level increases and defects occur in form of horizontal lines. The range of 40 pA to 70 pA at a bias voltage of −1.0 V shows good results in terms of contrast and noise level present in the STM images.

To quantitatively compare the image quality as a function of tunnel current setpoint the root mean squared roughness (RMS) was calculated with the gwyddion software package [103] and the results are shown in figure 7.6. The RMS is defined as:

$$RMS = \sqrt{\frac{1}{N}\sum_{n=1}^{N}(z_n - \bar{z})^2} \tag{7.1}$$

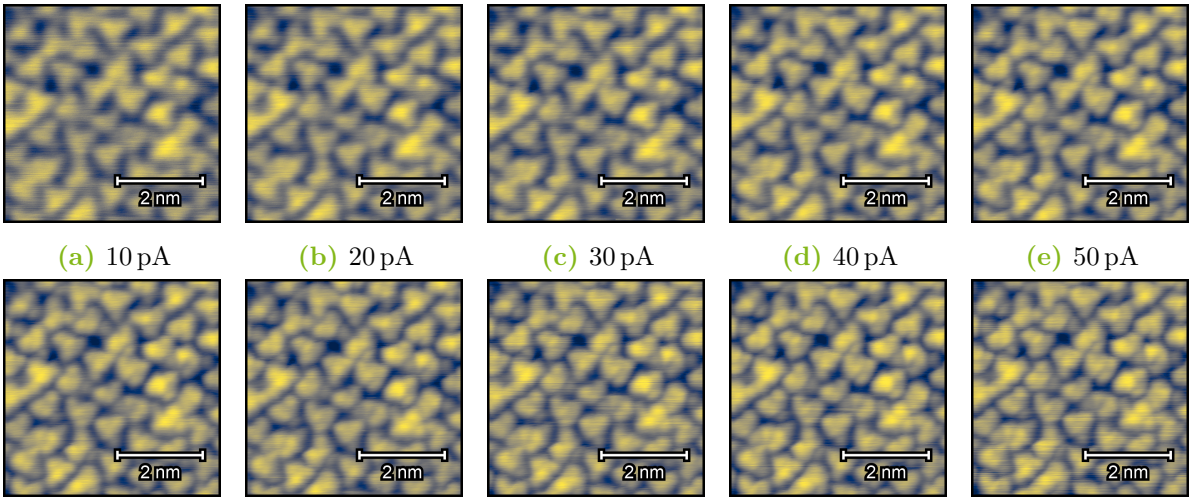

(a) 10 pA **(b)** 20 pA **(c)** 30 pA **(d)** 40 pA **(e)** 50 pA

(f) 60 pA **(g)** 70 pA **(h)** 80 pA **(i)** 90 pA **(j)** 100 pA

Figure 7.5: STM images in a measurement series obtained at one sample position with different current setpoints at a bias voltage of $U_{\text{gap}} = -1.0\,\text{V}$. Image size of each measurement is $5 \times 5\,\text{nm}^2$.

with N as the total number of measurement points - in this case 512×512 - and n as the index of each individual data point. The z-value or height of each pixel is z_n and the mean height is noted as $\bar{z}$. Therefore, the RMS literally describes the root mean square roughness of each STM measurement and is thus an indication of the standard variation of the heights in each STM image. As all filters would impact the roughness, the RMS is calculated for the raw unprocessed data [190].

Figure 7.6 shows the roughness as a function of the current setpoint of the STM. For each current setpoint, one upward and one downward image are recorded with one forward and one backward image, therefore four roughness values are calculated for each current setpoint, one for each stored image. For 50 pA, two full images were recorded, therefore 8 roughness values are depicted. The experimental uncertainty for the RMS in this series is approximately of the order of 1 pm. Overall a near linear increase of roughness in the range of 10 pA to 100 pA is visible in figure 7.6. As described earlier at low current setpoints the contrast is low which makes the measurements look blurry and decreases the roughness. Therefore, an increase in roughness corresponds with an increase in contrast in a specific range. Additionally, high roughness could indicate higher noise, as seen in the range of 80 pA to 100 pA. This increase of noise could also be the result of a slight change of the tunneling condition, as a decrease in roughness from 70 pA to 80 pA is visible. The probability of changes in tip condition is increased at higher current setpoints due to the increased interaction. As a simple explanation, formula 3.9 approximately describes the tunnel current and shows that the tunnel current is exponentially dependent on the

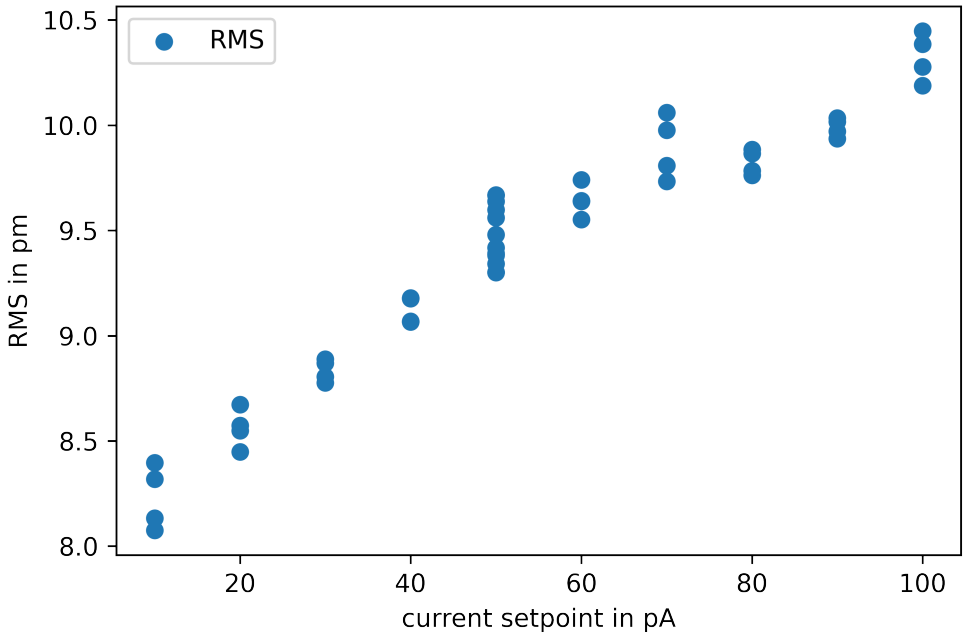

Figure 7.6: Root mean squared surface roughness (RMS) of the measurements series in figure 7.5 as a function of current setpoint at a bias voltage of $U_{\text{gap}} = -1.0\,\text{V}$.

tip-sample distance. Therefore, an increase of the current setpoint decreases the tip-sample distance which leads to more interaction and a bigger overlap of the involved orbitals. Here a smaller tunnel distance also leads to a better resolution which could be caused by a more localized tip orbital [154]. To account for these effects and achieve a stable measurement with sufficient resolution, the current setpoint is set to 50 pA in order to decrease the interaction between the molecules and the tip.

In a next step, the effect of different bias voltages for this constant setpoint current is studied. Therefore, a voltage dependent measurement series is shown in figure 7.7. Overall, the shape of the caffeine molecules visible in the voltage dependent images is similar to the current dependent series in figure 7.5. A slight change in resolution is visible from $-0.3\,\text{V}$ to $+0.5\,\text{V}$ and a drastic change occurs from $+2\,\text{V}$ to $+3\,\text{V}$ which resulted in the loss of inter molecular resolution. Therefore, this series shows the difficulty of obtaining clear and stable measurements while changing the bias voltage. At a bias voltage of $-1.5\,\text{V}$ the molecules appear smaller and the gaps between them are deeper in comparison to the measurement at a bias voltage of $-0.3\,\text{V}$. Additionally, in the range of $-0.7\,\text{V}$ to $-0.3\,\text{V}$ more details inside the molecules become visible and the outer protrusions appear larger. The switch towards positive bias voltage resulted in a drastic change of resolution which

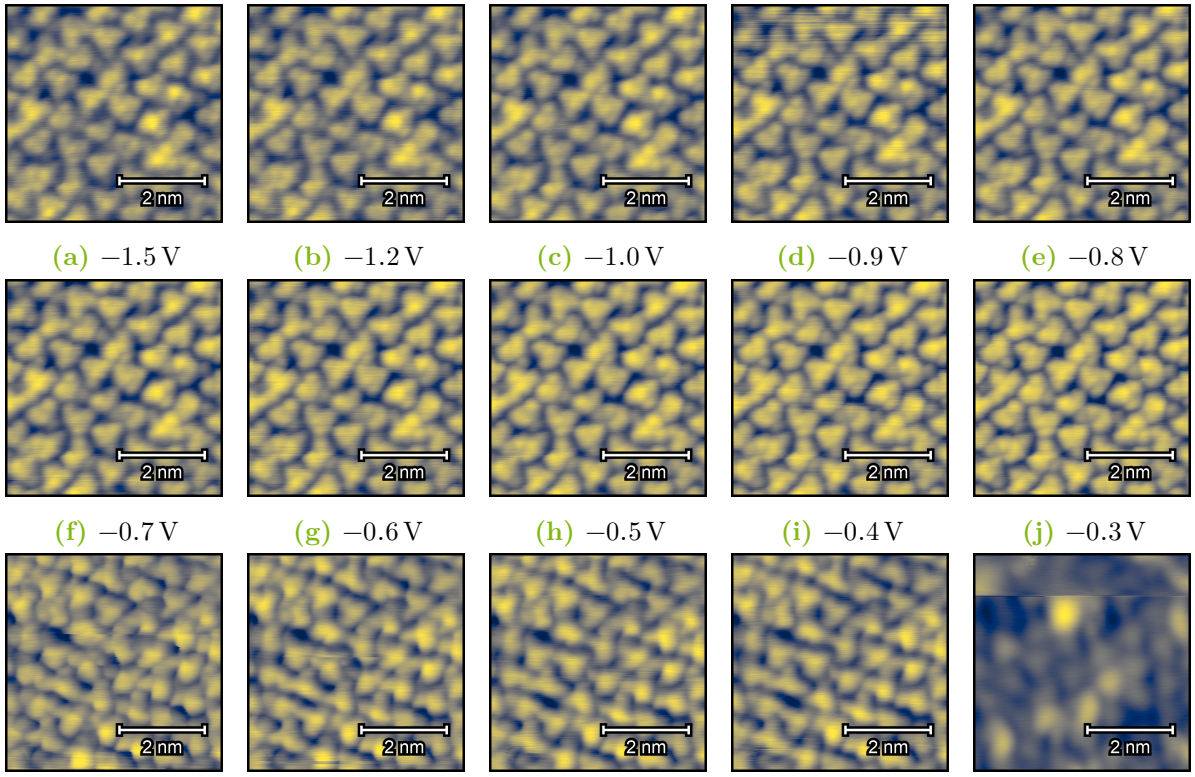

(a) −1.5 V (b) −1.2 V (c) −1.0 V (d) −0.9 V (e) −0.8 V

(f) −0.7 V (g) −0.6 V (h) −0.5 V (i) −0.4 V (j) −0.3 V

(k) +0.5 V (l) +1.0 V (m) +1.5 V (n) +2.0 V (o) +3.0 V

Figure 7.7: Measurement series of STM images at one sample position with increasing bias voltage *U*gap, as indicated, at a current setpoint of $I_{\text{tunnel}} = 50\,\text{pA}$. Each measurement has a size of $5 \times 5\,\text{nm}^2$. The resolution changes depending on the bias voltage. A bias voltage inversion resulted in a resolution change from 7.7 (j) to 7.7 (k). The tip condition from 7.7 (n) to 7.7 (o) changed and the intermolecular resolution was lost.

further changed form +2.0 V to 3.0 V. To compare the images quantitatively the RMS is calculated as before and the results are shown in figure 7.8.

A parabolic increase of the RMS roughness is detectable for negative bias voltages in figure 7.8. This is in accordance to the observed increase in details for smaller absolute bias voltages. For positive bias voltages the roughness decreases slightly due to the change of the tunnel orbital but the overall level of visible molecule substructures decreases significantly. The change of the tunnel orbital is not necessarily a consequence of the change in polarity as shown in figure 7.4 where the shape of the caffeine molecules remain nearly the same while changing the bias polarity. Nevertheless, in the case shown in figure 7.7 the change was caused by the polarity inversion. This happened frequently, so the risk of changing the tip condition when changing polarity is increased, and therefore a complete voltage-dependent measurement series at a stable tunnel condition could not be obtained.

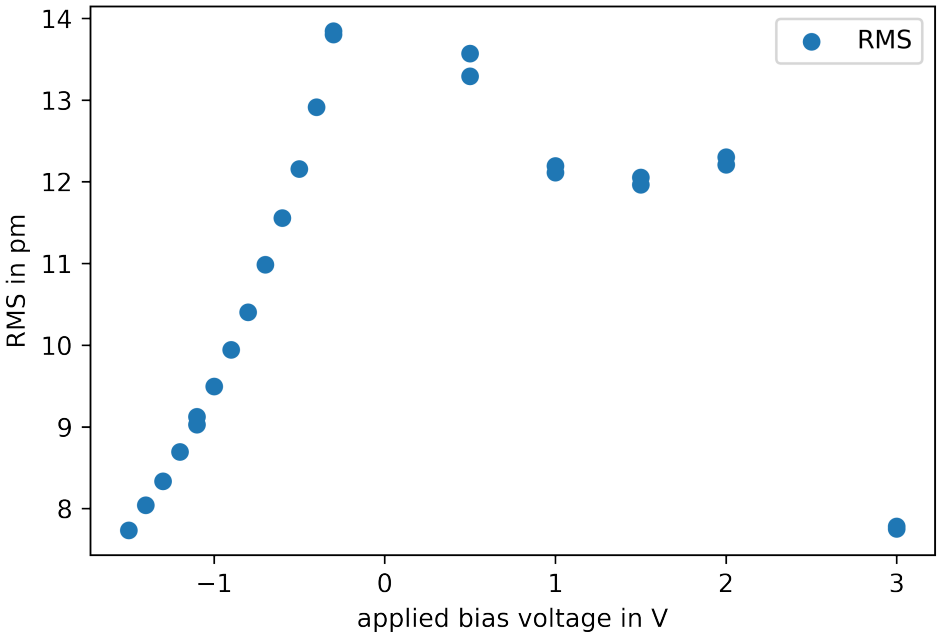

Figure 7.8: Root mean squared surface roughness (RMS) as a function of applied bias voltage at a current setpoint of 50 pA.

Furthermore, this shows the limited expressiveness of the RMS as only a small decrease in roughness from a bias voltage of 0.5 V in comparison to −0.3 V is observed but the visible details decreased significantly. Additionally, the huge decrease in roughness from 2.0 V towards 3.0 V shows that the roughness is no sufficient argument to characterize substructures of molecules in STM measurements which is further discussed by Nečas *et al.* [190] Therefore, the RMS is not an indicator of image quality or resolution, it could only compare images in one series with little variance and no change of the tunnel orbital. Nevertheless, in this limited field of application the RMS is a simple quantification which shows a strong dependence on the varied current setpoint and applied bias voltage in the range of 10 pA to 100 pA and −1.5 V to −0.3 V.

In summary the caffeine molecular monolayer is measurable in both bias polarities. The correlation of substructure resolution STM images and negative biases is shown in this measurement series. Moreover, bias gaps over $\Delta U_{\text{gap}} = 1.5\,\text{V}$ increase the risk of changing the tip condition and thus a change in resolution. Polarity inversion might also affect the resolution, which can leads to an extended period of tip conditioning with voltage pulses or intended sample crashes to regain the resolution [154]. For further measurements a standard bias voltage of −1.0 V at a current setpoint of 50 pA is chosen.

7.2 Submonolayer formation of caffeine molecules

In this section, the focus is on the analysis of coverage below a full dense monolayer of caffeine molecules. Analyzing these coverage is possible due to the decreased molecule mobility at low temperatures. Starting with a comparison of different coverage, followed by a study of distinct caffeine molecule assemblies.

7.2.1 Coverage dependence

Here, the coverage dependence of the caffeine molecule formation on a Au(111) surface is investigated in the sub-monolayer regime with several prepared samples. In order to lower the density of caffeine molecules on the surface the sample preparation scheme stayed the same with reduced deposition time. After deposition, the samples are also annealed at $\sim 80\,°C$ for 10 min to increase the mobility for an assembly process. The coverage is estimated via the height distribution of large scale STM images.

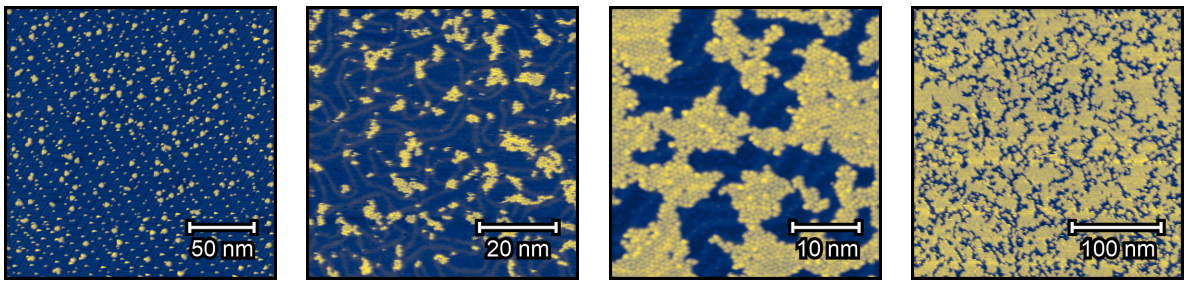

(a) $\sim 0.15\,ML$ **(b)** $\sim 0.25\,ML$ **(c)** $\sim 0.65\,ML$ **(d)** $\sim 0.80\,ML$

Figure 7.9: Coverage dependence of the formation of caffeine molecules on Au(111) measured at 4 K. Increasing coverage from (a) to (d). Small islands evolve towards larger networks. (50 pA, −1 V).

In figure 7.9 four samples at different coverage measured at 4 K are shown in an increasing order. In figure 7.9 (a) it is visible that the molecules start to adsorb at the reactive 'herringbone elbow sides' at a coverage of $\sim 0.15\,ML$. Furthermore, small assemblies of caffeine molecules evolve which are studied in more detail in section 7.2.2. At a coverage of $\sim 0.25\,ML$ shown in figure 7.9 (b) the caffeine assemblies are larger but not as ordered as at $\sim 0.15\,ML$ coverage. This could be an effect of the imperfectly reconstructed gold substrate for this sample, as the visible domain borders of the substrate are not aligned in the usual 'herringbone' structure in figure 7.9 (b). At higher caffeine coverage of $\sim 0.65\,ML$, as shown in figure 7.9 (c), assemblies similar to amorphous networks occur, with some areas comparable to the dense monolayer formation. Moreover, gaps are present between them,

which show the underlying gold substrate. Likewise for a higher coverage of ~ 0.80 ML as shown in figure 7.9 (d). There, the gaps become smaller with increasing coverage, but the overall amorphous network shape remains.

Comparing the coverage dependency of caffeine molecules on Au(111) measured at room temperature and at 4 K, the following points are observed. A line shape ordering at the substrate step edges for low coverage of about 0.3 ML, as found at room temperature in the section 6.1, was not reproduced for low temperatures. Noting that, these lines were found for a sample that was not annealed after deposition, which was not studied at low temperature. Annealed samples with low coverage at room temperature did not yield accessible STM measurements, and were therefore not investigated further.

The coverage just below the full monolayer at low temperature has similarities to the not annealed formation of about 1.3 ML at room temperature. For the annealed monolayer samples measured at room temperature, also some amorphous networks were found for the samples at $\sim 60\,^{\circ}$C and $\sim 70\,^{\circ}$C shown in figure 6.2 (a) and 6.2 (b). These have similarities with the assemblies measured at low temperature in the range of 0.25 ML to 0.65 ML, shown in figure 7.9 (b) and 7.9 (c). These measurements are not truly comparable because the assemblies studied at room temperature are most likely assemblies in the second layer as more caffeine was deposited there.

Concluding, that at low temperature and low coverage distinct islands with some form of order evolve towards larger amorphous networks which than become a dense monolayer formation in two mirrored domains. The comparison of the low and room temperature data is imperfect as submonolayer coverage is not easily accessible with RT-STM. Nevertheless, some similarities in form of amorphous networks are found. The next section focuses on the distinct caffeine island which assemble at low coverage and are only accessible with low temperature STM.

7.2.2 Supramolecular assemblies

Several distinct assemblies of caffeine molecules in submolecular coverage are found. Especially, for the 0.15 ML and 0.25 ML coverage samples a variety of assemblies is present. Presumably, a higher coverage forces the molecules in a dense package, which is very stable also for the room temperature samples. This is observed for the samples with 0.65 ML and 0.80 ML coverage. Furthermore, chiral behavior is found for some of the assemblies at low coverage, which are discussed in section 7.2.3.

Triangular caffeine assemblies

As shown in figure 7.3 (a), individual caffeine molecule appear in a triangular shape in the STM images. Moreover, not only individual molecules are observed as triangles, but the arrangement in larger triangles is also preferred. Figure 7.10 shows several STM images of different triangular caffeine arrangements. The top row with figure 7.10 (a) to 7.10 (c) shows constant current STM images of these caffeine assemblies. And the bottom row with figure 7.10 (d) to 7.10 (f) shows constant height STM measurements. Measurements of supramolecular assemblies in constant height mode show more details in the internal structure of the assembly. Therefore, these measurements are preferred when they are accessible.

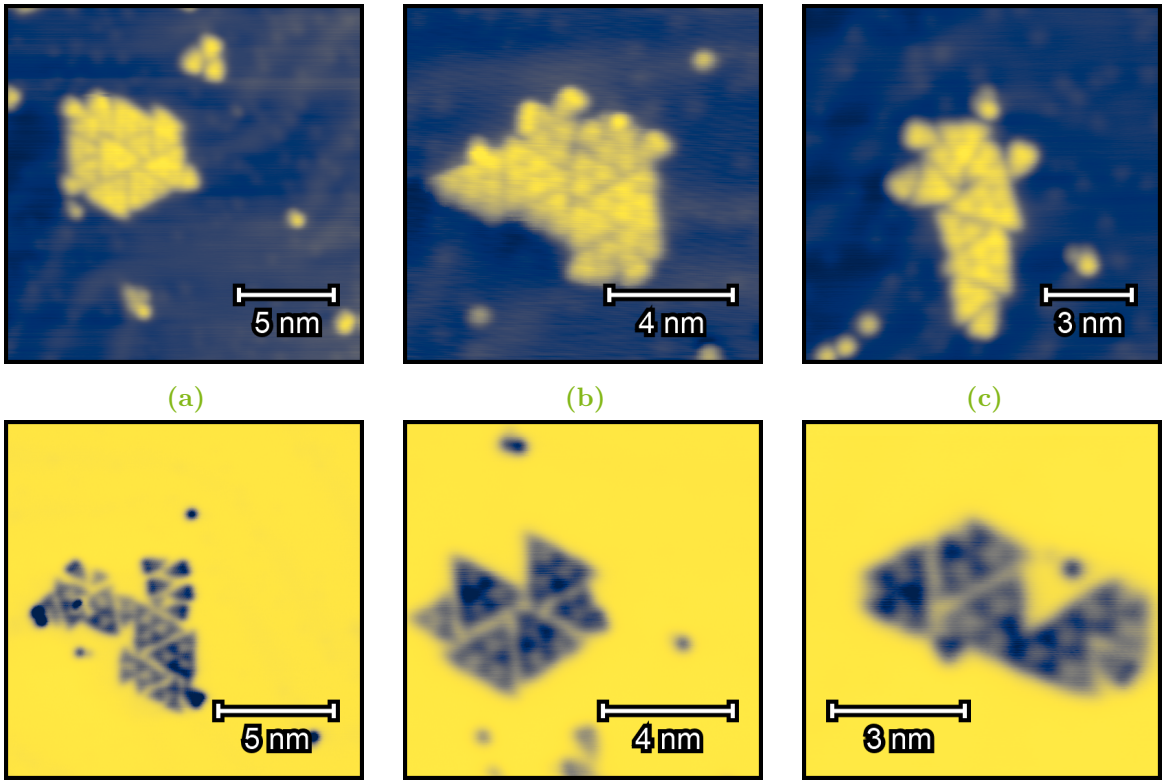

Figure 7.10: STM images of different triangular caffeine arrangements. Two main motifs are found. A small triangle containing three molecules and a larger triangle containing six molecules. (a) - (c) Constant current mode (50 pA, −1 V). (d) - (f) Constant height mode (−1 V).

There are two main motifs in the measurements of supramolecular assemblies. A small triangular unit with three molecules and a larger triangle with six molecules. These triangular building blocks appear in the measurements as self-contained units with small

gap lines between them. In the constant height images, the separation between contained triangle blocks is more visible. It is possible that the molecules form a supramolecular orbital, making them more electronically stable and visible in theSTM measurements [191]. Another possibility is, that the caffeine molecules align with the substrate at mirror twin boundaries, which forces the units one substrate lattice spacing away from each other [153, 192].

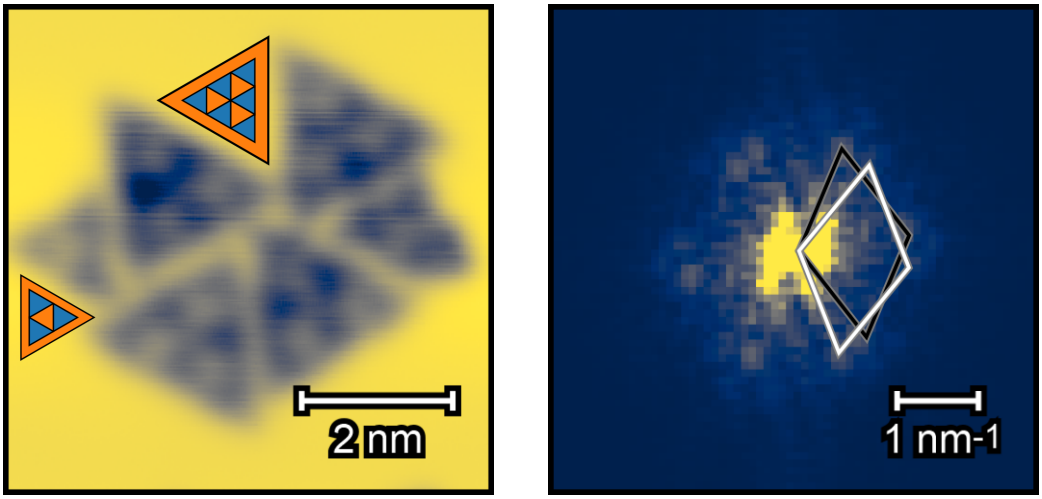

(a) **(b)** FFT of 7.11 (a)

Figure 7.11: (a) Constant height STM image of triangular assemblies of caffeine molecules on Au(111) at (−1 V). A model of a three molecule triangle and a six molecule triangle are displayed. (b) The FFT of (a) revealing twelve weak spots which are attributed to the nearest neighbor molecules.

To examine the constant height measurement in figure 7.10 (e) in more details, it is reproduced in larger in figure 7.11 (a). There are four larger triangles containing six molecules each and two smaller triangles containing three molecules each. The three molecule triangle is oriented in the way that one apex of each caffeine molecular triangle is also the apex of the larger three-molecule triangle. This induces a triangular shaped hole in the center of this unit. A model of this triangle is shown on the left side of figure 7.11 (a). Individual caffeine molecules are represented by a blue triangle.

For the larger six molecule triangle, a row of three caffeine molecules is attached to the side of a three molecule triangle containing its alignment. Therefore, the apexes of the six molecule block consist of individual caffeine molecules with an apex pointing outward. Thus, there are three caffeine molecules in the middle pointing to the center. This inward pointing triangular alignment is characteristic for this building block, which appears darker in the constant height images and therefore is more visible. A model of this triangle is shown on the top of figure 7.11 (a). Figure 7.11 (b) shows the FFT of figure 7.11 (a), which

reveals twelve weak spots. These spots are attributed to the nearest neighbor molecules and are very similar to the before found pattern for the two mirrored domains of the dense monolayer. This strengthens the hypothesis that the separation of the larger triangles could be induced by the substrate. Such mirror twin grain boundaries are i.e. common for molybdenum dichalcogenides [193].

Twelve molecular assembly

Another distinct assembly of caffeine molecules is found for the 0.15 ML coverage. In order to document this, figure 7.12 shows a zoom series of STM measurements at 0.15 ML coverage. Figure 7.12 (a) shows a large scale overview image, revealing single molecules adsorbed at the 'herringbone' elbow sites, as well as many small caffeine assemblies distributed throughout the sample. The next measurement in figure 7.12 (b) shows that theses assemblies have similar shapes and are not necessarily aligned or attached to the substrate elbows. Furthermore, the shape of these assemblies is shown in large in figure 7.12 (c). There, a formation of twelve caffeine molecules can be seen, which at first glance resembles the triangular shapes in the last section with an additional row of molecules. However, one caffeine molecule is missing from each of the tips of the triangle, reducing the number of molecules to twelve from the expected fifteen. In addition, the alignment of the molecules appears to create a hole in the center while maintaining the total number of molecules. This twelve molecule structure appears to be particularly stable, since it is very common at this coverage.

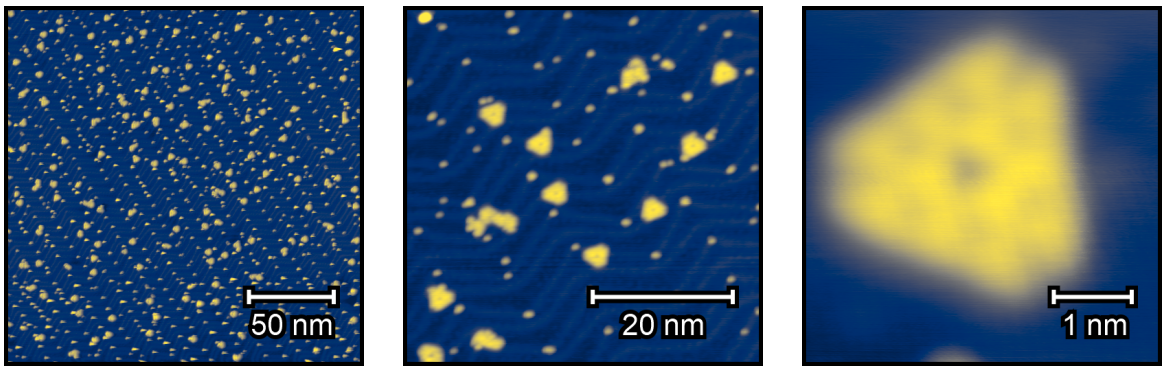

Figure 7.12: STM measurements at a caffeine coverage of 0.15 ML with several distinct assemblies of twelve caffeine molecules in a similar fashion. (a) overview image in a size of 200 × 200 nm. (b) Zoom of (a) in a size of 50 × 50 nm. (c) Close up of one twelve molecular assembly in a size of 5 × 5 nm. (50 pA, −1 V for all)

To investigate this further, the twelve molecule arrangement is measured in three different measurement modes, shown in figure 7.13. Figure 7.13 (a) shows the height differences measured in constant current mode. There, the shape of individual caffeine molecules is not sufficiently resolved, but the domain boundaries of the gold substrate are visible. Figure 7.13 (b) shows changes of the tunnel current in constant height mode with negative bias voltage of $U = -1\,\mathrm{V}$. And figure 7.13 (c) depicts the constant height mode with a positive applied bias voltage of $U = 1\,\mathrm{V}$. Therefore, the colormap of 7.13 (b) is inverted in comparison to 7.13 (c) as it represents the current that is inverted due to polarity inversion. In the constant height measurements, the triangular shape of individual caffeine molecules is more evident and the alignment is better resolved.

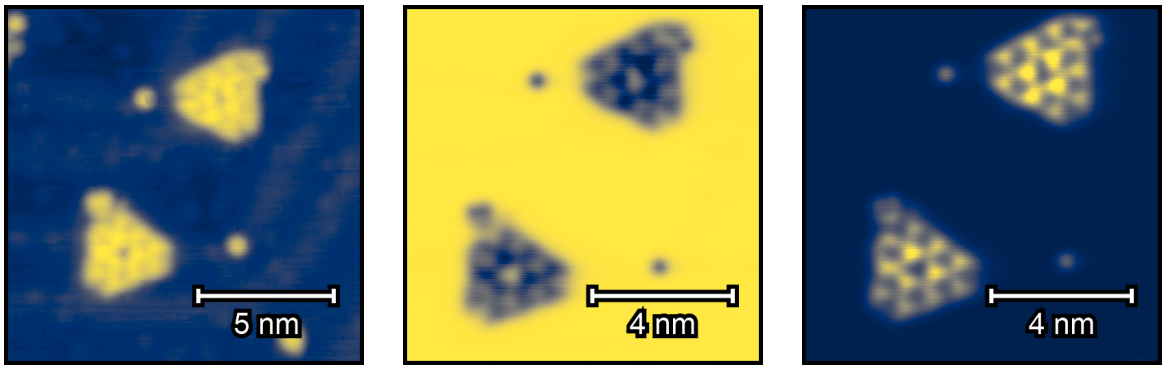

(a) (b) (c)

Figure 7.13: Close up of two twelve molecular assemblies measured at three measuring condition. (a) Constant current mode (50 pA, −1 V). (b) Constant height mode (−1 V). (c) Constant height mode, (1 V).

In both assemblies, there is an additional molecule adjacent to one apex of the twelve molecular unit that is not properly aligned within the unit. This suggests that the alignment of an additional caffeine molecule at these corners is energetically unfavorable. In addition, larger defined triangular shaped assemblies are not found on the surface. In comparison, this particular twelve molecular assembly occurred relativity frequently. The FFT of these assemblies revealed only six broad spots indicating a hexagonal order. Hence, no additional information about the domain crystallization is obtained with these measurements. Concluding that three different arrangements of caffeine molecules on Au(111) can be identified. In the next section, a superposition of these structures is shown, which can produce a chiral arrangement on the sample surface.

7.2.3 Handed 'propeller' assemblies

Larger superstructures can be formed with the triangular supramolecular arrangements of caffeine molecules described previously. An example is the here called 'propeller' formation, which is a superposition of the small three molecule triangular arrangements and is shown in figure 7.14. The formation is called 'propeller' because six three-molecular triangles are aligned in such a way that they form a star-shaped hole. This star-shaped hole has arms that are all bent in one direction, creating a resemblance to the helical blades of a screw

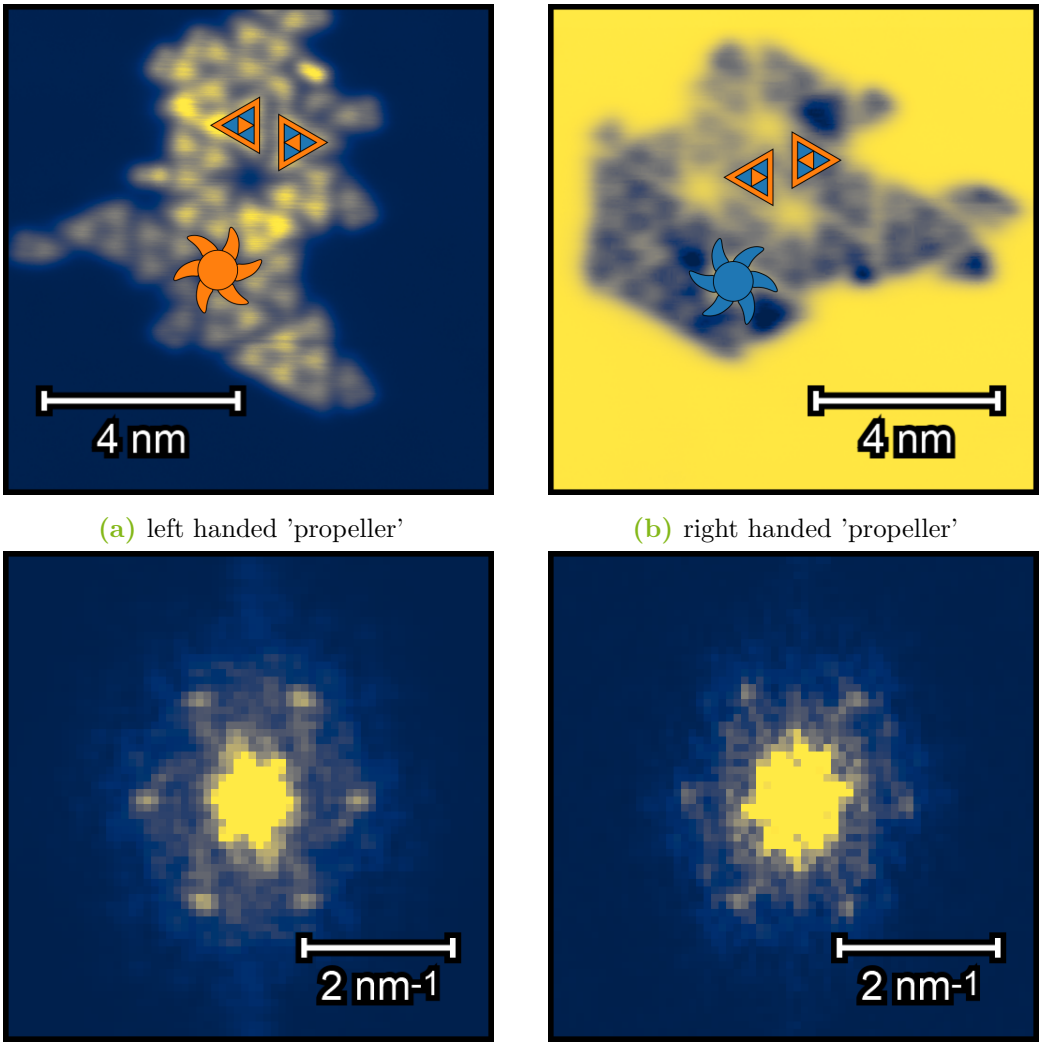

(a) left handed 'propeller'

(b) right handed 'propeller'

(c) FFT of 7.14 (a)

(d) FFT of 7.14 (b)

Figure 7.14: Constant height STM images of chiral superstructes of caffeine molecule assemblies on Au(111). (a) Two left handed 'propeller' alignments are present. The chiral character is indicated with a orange 'propeller'. ($10 \times 10\,\text{nm}$, $1\,\text{V}$). (b) Four right handed 'propeller' alignments. An indicator is depicted in blue. ($10 \times 10\,\text{nm}$, $-1\,\text{V}$). (c) FFT of (a). (d) FFT of (b). Both FFT images show the same hexagonal pattern oriented in the same directions.

propeller commonly used for ships or airplanes [194]. A model of both variants is depicted in figure 7.14, the left handed one in orange and the right handed one in blue.

The chiral behavior is induced by the order in which the three molecular triangles are aligned. Taking two of these triangles and aligning them along one of their sides introduces two possibilities to achieve a hexagonal order. One option is to go up half a molecule length with the left triangle and the other option is to go down half a molecule length with the left triangle. Both options are depicted, one in figure 7.14 (b) and one in figure 7.14 (a), respectively. Below the measurements which reveal the two chiral 'propeller' alignments, their FFTs are shown in figure 7.14 (c) and 7.14 (d), respectively. Both FFTs show six spots indicating a hexagonal order for both alignments. Furthermore, the direction of the spots are comparable as both measurements are obtained from the same sample and no angular rotation of the STM is applied in the measurement or post processing software. Both patterns are congruent and the spots point in the same direction within the measurement uncertainty. Therefore, the assembly of the chiral 'propellers' is not a sign of the two mirror domains.

Concluding, that the supramolecular assemblies of caffeine molecules on Au(111) induce chiral superstructures. These structures occur at low coverage and are resolvable with a LT-STM. At higher coverage, the caffeine molecules form a dense monolayer formation and the hole induced by the chiral superstructure is filled. Presumably, the 'propeller' structure grows in a single domain, since the FFTs in figure 7.14 (c) and 7.14 (d) reveal only one hexagonal pattern. Therefore, the 'propeller' formation should occur in both mirrored domains, which was not measured here.

Comparing these results with previous studies of xanthine derivatives on Au(111), no direct transfer of assemblies is found. A study of theobromine monolayers on Au(111) at room temperature showed, that theobromine molecules are also prochiral. There, two enantiomers are aligned in a zig-zag structure, which is explained by glide reflections [54]. Noting, that the formation of theobromine exhibit a rectangular unit cell in the monolayer coverage and thus differs from the structures found here. Moreover, for theophylline spontaneous chiral symmetry breaking was found between racemic monolayers. This was observed with unichiral stripes between molecular domains [53]. As show above, the domain borders between the found caffeine formations are not sharp on a single terrace and no ordered transition phase was found in this work. Furthermore, the DFT simulation shows that the caffeine film exhibits a ratio of 1:2 of its prochiral constituents. In addition, the formation of core xanthine molecules on Au(111) revealed self-assembled homochiral quintet networks, zickzag stripes, and sunflower structures consisting of di-pentamers assemblies [157], which are also different from the triangular formations found here.

Chapter 8

Conclusion

In this work, a structural analysis of the caffeine formations on a Au(111) substrate was performed using a combination of different surface sensitive tools and techniques. For this purpose, the VT-STM chamber was extended by a new experimental table and equipped with a new manipulator. Moreover, several minor upgrades were implemented to enable and ensure stable and reproducible sample preparation. For the analysis of the caffeine formations, the experimental results were divided into three main parts - the preparation, the room temperature analysis and the low temperature study.

The preparation of a defined coverage of caffeine molecules on the Au(111) substrate was studied in chapter 5. There, the molecular-beam epitaxy of caffeine molecules in UHV was studied with a quartz crystal microbalance and a quadrupole mass spectrometer. The preparation method found, was applied and successfully reproduced at several UHV chambers located at different research facilities. Many thanks to the staff of DELTA and the group of PD Dr. Daniel Bürgler and Dr. Frank Matthes for access to their experiments. Moreover, the reproduction shows the robustness of the presented preparation method.

The main part of this work was the investigation of the dense monolayer formation of caffeine molecules on Au(111) at room temperature, presented in chapter 6. The experimental investigation was performed by STM, LEED, and XPS, complemented by a DFT analysis, which was gratefully conducted by Andreas Jeindl and the group around Prof. Dr. Oliver T. Hofmann. In this investigation two mirrored domains of a densely packed monolayer film of caffeine molecules on Au(111) were found. The molecules form a quasi-hexagonal structure with a nearest neighbor distance of (8.6 ± 0.3) Å and an angle of $(\pm 11.0 \pm 0.8)°$ towards the $[1\bar{1}0]$-Au-axis for each domain, respectively. This quasi-hexagonal structure is observed in real space with STM and in reciprocal space with LEED and can be described as a $\begin{pmatrix} 10/3 & 2/3 \\ 8/3 & 10/3 \end{pmatrix}$-structure or as $\left(2/3\sqrt{21} \times 2/3\sqrt{21}\right) R \pm 10.9°$ with respect to an unreconstructed Au(111)-surface. The DFT simulation of a hypothetical free-standing monolayer dismissed the hexagonal superstructure with only one molecule in the unit cell. Therefore, a configuration of differently orientated molecules is energetically favorable compared to a structure with all molecules aligned in the same orientation. Taking this into account, the caffeine monolayer can be described as a $\begin{pmatrix} 6 & 4 \\ 2 & 6 \end{pmatrix}$- superlattice or $\left(2\sqrt{7} \times 2\sqrt{7}\right) R \pm 19.1°$ with three caffeine molecules within a unit cell and a lattice constant of 15.2 Å. This superstructure is the smallest commensurable surface structure on the Au(111)-surface, which is in accordance with the experimental results. The ab-initio

simulations led to a proposed geometrical structure of a three molecular unit cell, which is shown in figure 6.11 and is in accordance with all experimental data. Moreover, the optimized structure shows a mixture of both on-surface chiralities of caffeine molecules in a ratio of 1:2 and vice versa for the mirrored domain. This indicates the importance of the prochiral nature of caffeine in relation to structure formation.

An additional study of the formation of caffeine molecules on Au(111) was performed at low temperature and is shown in chapter 7. There, the dense monolayer formation was reproduced at the NSCT. A slightly smaller nearest neighbor distance was found for the dense monolayer formation with $a = (8.3 \pm 0.4)$ Å, which is within the uncertainty estimate. In addition, a correlation was found between the applied bias voltage and the RMS of the measured STM images, and as well for the current setpoint and the RMS. The level of detail of the substructure of the caffeine molecules also depends on the applied bias voltage and current setpoint. Stable tunneling conditions were found in these measurements. Moreover, for the low temperature measurements the focus was on the study of the caffeine submonolayer coverage. In this submonolayer coverage, the caffeine molecules showed a strong tendency to form supramolecular assemblies. Three macro molecular triangle formations were distinguished and are shown in section 7.2.2. Furthermore, a chiral 'propeller' motif build from three molecular triangle formations was found. This 'propeller' formation shows the ability of achiral molecules to form larger chiral assemblies and underlines the importance of chirality.

The caffeine monolayer structure found here is in excellent accordance with previous studies on different substrates. A hexagonal crystal structure was found in surface mediated crystals on substrates like silicon, silver, or soda lime glass [21]. Similar results were found for the layers of metastable hexagonal bulk crystals of caffeine discovered by Derollez et al. [47]. In addition, disorder effects were predicted for form II caffeine crystals [195]. Moreover, the here found two preferred orientations of caffeine alignments show the influence of the prochiral character of the achiral caffeine molecule on the monolayer growth on Au(111). Therefore, the prochiral character might play a role in the formation of surface mediated crystals on substrates like ionic crystals [23].

In conclusion, within this thesis the formation of caffeine molecules on a Au(111) surface was investigated comprehensively. In a further investigation, the electronic structure of the assemblies in the submonolayer regime could be studied with scanning tunneling spectroscopy (STS). A study of tip-induced change in the assembly could yield interesting results, as well as the change of the substrate. Moreover, the combination of caffeine molecules with similar molecules like adenine, xanthine, or theobromine could form cocrystals on the surface, which could be studied with a similar approach.

Bibliography

[1] I. Langmuir, *Two-Dimensinal Gases, Liquids and solids*, Science **84**, 379 (1936).

[2] K. B. Blodgett, *Monomolecular Films of Fatty Acids on Glass*, Journal of the American Chemical Society **56**, 495 (1934).

[3] K. B. Blodgett, *Films Built by Depositing Successive Monomolecular Layers on a Solid Surface*, Journal of the American Chemical Society **57**, 1007 (1935).

[4] D. Tabor, *The Solid Surface*, Physics Bulletin **29**, 521 (1978).

[5] D. P. Woodruff, *Modern techniques of surface science*, Cambridge University Press, Cambridge (2016).

[6] C. B. Duke, *The birth and evolution of surface science: child of the union of science and technology*, Proceedings of the National Academy of Sciences of the United States of America **100**, 3858 (2003).

[7] G. Binnig, H. Rohrer, C. Gerber, and E. Weibel, *7 × 7 Reconstruction on Si(111) Resolved in Real Space*, Physical Review Letters **50**, 120 (1983).

[8] A. Ulman, *An Introduction to Ultrathin Organic Films: From Langmuir–Blodgett to Self–Assembly*, Academic Press, San Diego (1991).

[9] R. Blankenburg, P. Meller, H. Ringsdorf, and C. Salesse, *Interaction between biotin lipids and streptavidin in monolayers: formation of oriented two-dimensional protein domains induced by surface recognition*, Biochemistry **28**, 8214 (1989).

[10] S. Romer, B. Behzadi, R. Fasel, and K.-H. Ernst, *Homochiral conglomerates and racemic crystals in two dimensions: tartaric acid on Cu(110)*, Chemistry - A European Journal **11**, 4149 (2005).

[11] M. Ortega Lorenzo, C. J. Baddeley, C. Muryn, and R. Raval, *Extended surface chirality from supramolecular assemblies of adsorbed chiral molecules*, Nature **404**, 376 (2000).

[12] S. J. Sowerby, N. G. Holm, and G. B. Petersen, *Origins of life: A route to nanotechnology*, Biosystems **61**, 69 (2001).

[13] L. Kong, A. Enders, T. S. Rahman, and P. A. Dowben, *Molecular adsorption on graphene*, Journal of Physics: Condensed Matter **26**, 443001 (2014).

[14] A. Kumar, K. Banerjee, and P. Liljeroth, *Molecular assembly on two-dimensional materials*, Nanotechnology **28**, 082001 (2017).

[15] S. R. Forrest, *The path to ubiquitous and low-cost organic electronic appliances on plastic*, Nature **428**, 911 (2004).

[16] H.-W. Chen, J.-H. Lee, B.-Y. Lin, S. Chen, and S.-T. Wu, *Liquid crystal display and organic light-emitting diode display: present status and future perspectives*, Light: Science & Applications **7**, 17168 (2018).

[17] C. Becker, *From Langmuir to Ertl: The "Nobel" History of the Surface Science Approach to Heterogeneous Catalysis*, in *Encyclopedia of Interfacial Chemistry*, edited by K. Wandelt, Elsevier, Amsterdam (2018).

[18] R. Otero, A. L. Vázquez de Parga, and J. M. Gallego, *Electronic, structural and chemical effects of charge-transfer at organic/inorganic interfaces*, Surface Science Reports **72**, 105 (2017).

[19] V. R. Preedy, editor, *Coffee in health and disease prevention*, Nutrition and dietetics, Elsevier, Amsterdam (2015).

[20] J. Leiterer, F. Emmerling, U. Panne, W. Christen, and K. Rademann, *Tracing coffee tabletop traces*, Langmuir **24**, 7970 (2008).

[21] A. Sarfraz, A. Simo, R. Fenger, W. Christen, K. Rademann, U. Panne, and F. Emmerling, *Morphological Diversity of Caffeine on Surfaces: Needles and Hexagons*, Crystal Growth & Design **12**, 583 (2012).

[22] C. Röthel, M. Radziown, R. Resel, A. Zimmer, C. Simbrunner, and O. Werzer, *Complex Behavior of Caffeine Crystallites on Muscovite Mica Surfaces*, Crystal Growth & Design **15**, 4563 (2015).

[23] C. Röthel, M. Radziown, R. Resel, A. Grois, C. Simbrunner, and O. Werzer, *Crystal alignment of caffeine deposited onto single crystal surfaces via hot-wall epitaxy*, CrystEngComm **19**, 2936 (2017).

[24] C. Ambrosch-Draxl, D. Nabok, P. Puschnig, and C. Meisenbichler, *The role of polymorphism in organic thin films: Oligoacenes investigated from first principles*, New Journal of Physics **11**, 125010 (2009).

[25] T. Yoshihara, M. Zaitsu, F. Shiraishi, H. Arima, F. Takahashi-Yanaga, M. Arioka, S. Kajioka, and T. Sasaguri, *Influence of genetic polymorphisms and habitual caffeine intake on the changes in blood pressure, pulse rate, and calculation speed after caffeine*

intake: A prospective, double blind, randomized trial in healthy volunteers, Journal of Pharmacological Sciences **139**, 209 (2019).

[26] T. Fallavena, M. Antonow, and R. S. Gonçalves, *Caffeine as non-toxic corrosion inhibitor for copper in aqueous solutions of potassium nitrate*, Applied Surface Science **253**, 566 (2006).

[27] F. S. de Souza, C. Giacomelli, R. S. Gonçalves, and A. Spinelli, *Adsorption behavior of caffeine as a green corrosion inhibitor for copper*, Materials Science and Engineering C **32**, 2436 (2012).

[28] L. G. da Trindade and R. S. Gonçalves, *Evidence of caffeine adsorption on a low-carbon steel surface in ethanol*, Corrosion Science **51**, 1578 (2009).

[29] R. Wang, J. Xue, L. Meng, J.-W. Lee, Z. Zhao, P. Sun, Le Cai, T. Huang, Z. Wang, Z.-K. Wang, Y. Duan, J. L. Yang, S. Tan, Y. Yuan, Y. Huang, and Y. Yang, *Caffeine Improves the Performance and Thermal Stability of Perovskite Solar Cells*, Joule **3**, 1 (2019).

[30] H.-J. Lee, G. Kim, and Y.-K. Kwon, *Molecular adsorption study of nicotine and caffeine on single-walled carbon nanotubes from first principles*, Chemical Physics Letters **580**, 57 (2013).

[31] A. Nehlig, J.-L. Daval, and G. Debry, *Caffeine and the central nervous system: Mechanisms of action, biochemical, metabolic and psychostimulant effects*, Brain Research Reviews **17**, 139 (1992).

[32] A. R. Costenla, R. A. Cunha, and A. de Mendonça, *Caffeine, adenosine receptors, and synaptic plasticity*, Journal of Alzheimer's Disease **20**, 25 (2010).

[33] X. Chen, Y. Liu, E. C. Jaenicke, and A. N. Rabinowitz, *New concerns on caffeine consumption and the impact of potential regulations: The case of energy drinks*, Food Policy **87**, 101746 (2019).

[34] J. J. Barone and H. Roberts, *Human Consumption of Caffeine*, in *Caffeine*, edited by B. Siegel, Springer, Berlin, Heidelberg (2012).

[35] C. D. Frary, R. K. Johnson, and M. Q. Wang, *Food sources and intakes of caffeine in the diets of persons in the United States*, Journal of the American Dietetic Association **105**, 110 (2005).

[36] G. Grosso, J. Godos, F. Galvano, and E. L. Giovannucci, *Coffee, Caffeine, and Health Outcomes: An Umbrella Review*, Annual Review of Nutrition **37**, 131 (2017).

[37] L. M. Juliano and R. R. Griffiths, *A critical review of caffeine withdrawal: empirical validation of symptoms and signs, incidence, severity, and associated features*, Psychopharmacology **176**, 1 (2004).

[38] D. C. Mitchell, C. A. Knight, J. Hockenberry, R. Teplansky, and T. J. Hartman, *Beverage caffeine intakes in the U.S*, Food and Chemical Toxicology **63**, 136 (2014).

[39] R. M. Gilbert, J. A. Marshman, M. Schwieder, and R. Berg, *Caffeine content of beverages as consumed*, Canadian Medical Association Journal **114**, 205 (1976).

[40] J. P. Higgins, T. D. Tuttle, and C. L. Higgins, *Energy beverages: content and safety*, Mayo Clinic Proceedings **85**, 1033 (2010).

[41] O. P. Mathew, *Apnea of prematurity: pathogenesis and management strategies*, Journal of Perinatology **31**, 302 (2011).

[42] B. A. Weinberg and B. K. Bealer, *The world of caffeine: The science and culture of the world's most popular drug*, Routledge, New York (2001).

[43] Nobel Media, *All Nobel Prizes in Chemistry,* ***https://www.nobelprize.org/prizes/lists/all-nobel-prizes-in-chemistry/*** (Retrieved: 28.05.2021).

[44] C. M. Gibson and P. W. Fowler, *Aromaticity of caffeine, xanthine and the dimethyl xanthines*, Tetrahedron Letters **55**, 2078 (2014).

[45] K. Momma and F. Izumi, *VESTA 3 for three-dimensional visualization of crystal, volumetric and morphology data*, Journal of Applied Crystallography **44**, 1272 (2011).

[46] D. J. Sutor, *The structures of the pyrimidines and purines. VII. The crystal structure of caffeine*, Acta Crystallographica **11**, 453 (1958).

[47] P. Derollez, N. T. Correia, F. Danède, F. Capet, F. Affouard, J. Lefebvre, and M. Descamps, *Ab initio structure determination of the high-temperature phase of anhydrous caffeine by X-ray powder diffraction*, Acta Crystallographica B **61**, 329 (2005).

[48] C. W. Lehmann and F. Stowasser, *The crystal structure of anhydrous beta-caffeine as determined from X-ray powder-diffraction data*, Chemistry **13**, 2908 (2007).

[49] E. Dichi, B. Legendre, and M. Sghaier, *Physico-chemical characterisation of a new polymorph of caffeine*, Journal of Thermal Analysis and Calorimetry **115**, 1551 (2014).

[50] H. R. Brand, P. E. Cladis, and H. Pleiner, *Symmetries and physical properties of polar columnar phases in materials composed of achiral molecules*, Europhysics Letters **57**, 368 (2002).

[51] O. Stetsovych, M. Švec, J. Vacek, J. V. Chocholoušová, A. Jančařík, J. Rybáček, K. Kosmider, I. G. Stará, P. Jelínek, and I. Starý, *From helical to planar chirality by on-surface chemistry*, Nature Chemistry **9**, 213 (2017).

[52] F. Zaera, *Chirality in adsorption on solid surfaces*, Chemical Society Reviews **46**, 7374 (2017).

[53] M. Pividori, C. Dri, M. E. Orselli, F. Berti, M. Peressi, and G. Comelli, *Spontaneous symmetry breaking on ordered, racemic monolayers of achiral theophylline: Formation of unichiral stripes on Au(111)*, Nanoscale **8**, 19302 (2016).

[54] I. Baltaci, M. G. H. Schulte, and C. Westphal, *Structural Analysis of Theobromine Monolayers on Weakly Interacting Surfaces*, The Journal of Physical Chemistry C **124**, 23648 (2020).

[55] K. Oura, V. G. Lifšic, A. A. Saranin, A. V. Zotov, and M. Katayama, *Surface science*, Springer, Berlin, Heidelberg (2003).

[56] T. K. Piskorz, C. Gobbo, S. J. Marrink, S. de Feyter, A. H. de Vries, and J. H. van Esch, *Nucleation Mechanisms of Self-Assembled Physisorbed Monolayers on Graphite*, The Journal of Physical Chemistry C **123**, 17510 (2019).

[57] L. Zhou, *Progress and problems in hydrogen storage methods*, Renewable and Sustainable Energy Reviews **9**, 395 (2005).

[58] F. Huber, J. Berwanger, S. Polesya, S. Mankovsky, H. Ebert, and F. J. Giessibl, *Chemical bond formation showing a transition from physisorption to chemisorption*, Science **366**, 235 (2019).

[59] M. Henzler and W. Göpel, *Oberflächenphysik des Festkörpers*, Teubner, Stuttgart (1994).

[60] F. Schreiber, *Structure and growth of self-assembling monolayers*, Progress in Surface Science **65**, 151 (2000).

[61] B. K. W. Thomson, *Baltimore Lectures on Molecular Dynamics and the Wave Theory of Light*, Cambridge University Press, Cambridge (1904).

[62] C. J. Baddeley and N. V. Richardson, *Chirality at Metal Surfaces*, in *Scanning Tunneling Microscopy in Surface Science*, edited by M. Bowker and P. R. Davies, Wiley-VCH, Weinheim (2009).

[63] R. S. Cahn, C. Ingold, and V. Prelog, *Specification of Molecular Chirality*, Angewandte Chemie International Edition **5**, 385 (1966).

[64] K.-H. Ernst, *Molecular chirality at surfaces*, Physica Status Solidi B **249**, 2057 (2012).

[65] L. Pasteur, *Recherches sur les relations qui peuvent exister entre la forme cristalline, la composition chimique et le sens de la polarisation rotatoire*, Annales de Chimie et de Physique **24**, 442 (1848).

[66] K.-H. Ernst, *Molecular chirality in surface science*, Surface Science **613**, 1 (2013).

[67] G. J. Hutchings, M. Brust, and H. Schmidbaur, *Gold–an introductory perspective*, Chemical Society Reviews **37**, 1759 (2008).

[68] D. A. Papaconstantopoulos, *Handbook of the Band Structure of Elemental Solids: From Z = 1 To Z = 112*, Springer, New York (2015).

[69] N. Takeuchi, C. T. Chan, and K. M. Ho, *Au(111): A theoretical study of the surface reconstruction and the surface electronic structure*, Physical Review B **43**, 13899 (1991).

[70] A. R. Sandy, S. G. J. Mochrie, D. M. Zehner, G. Grübel, K. G. Huang, and D. Gibbs, *Reconstruction of the Pt(111) surface*, Physical Review Letters **68**, 2192 (1992).

[71] Ž. Crljen, P. Lazić, D. Šokčević, and R. Brako, *Relaxation and reconstruction on (111) surfaces of Au, Pt, and Cu*, Physical Review B **68**, 195411 (2003).

[72] J. V. Barth, H. Brune, G. Ertl, and R. J. Behm, *Scanning tunneling microscopy observations on the reconstructed Au(111) surface*, Physical Review B **42**, 9307 (1990).

[73] M. P. Everson, *Effects of surface features upon the Au(111) surface state local density of states studied with scanning tunneling spectroscopy*, Journal of Vacuum Science & Technology B **9**, 891 (1991).

[74] S. Narasimhan and D. Vanderbilt, *Elastic stress domains and the herringbone reconstruction on Au(111)*, Physical Review Letters **69**, 1564 (1992).

[75] Y. Hasegawa and P. Avouris, *Manipulation of the Reconstruction of the Au(111) Surface with the STM*, Science **258**, 1763 (1992).

[76] F. Hanke and J. Björk, *Structure and local reactivity of the Au(111) surface reconstruction*, Physical Review B **87**, 235422 (2013).

[77] A. P. Seitsonen, *Electronic structure of reconstructed Au(111) studied with density functional theory*, Surface Science **643**, 150 (2016).

[78] J. A. Meyer, I. D. Baikie, E. Kopatzki, and R. J. Behm, *Preferential island nucleation at the elbows of the Au(111) herringbone reconstruction through place exchange*, Surface Science **365**, 647 (1996).

[79] G. Binnig, H. Rohrer, C. Gerber, and E. Weibel, *Surface Studies by Scanning Tunneling Microscopy*, Physical Review Letters **49**, 57 (1982).

[80] G. Binnig, H. Rohrer, C. Gerber, and E. Weibel, *Tunneling through a controllable vacuum gap*, Applied Physics Letters **40**, 178 (1982).

[81] G. Binnig and H. Rohrer, *Geburt und Kindheit der Rastertunnelmikroskopie (Nobel-Vortrag)*, Angewandte Chemie **99**, 622 (1987).

[82] Nobel Media, *All Nobel Prizes in Physics,* `https://www.nobelprize.org/prizes/lists/all-nobel-prizes-in-physics/` (Retrieved: 28.05.2021).

[83] R. H. Fowler and L. Nordheim, *Electron Emission in Intense Electric Fields*, Proceedings of the Royal Society A **119**, 173 (1928).

[84] G. Gamow, *Zur Quantentheorie des Atomkernes*, Zeitschrift für Physik **51**, 204 (1928).

[85] F. Schwabl, *Quantenmechanik*, Springer, Berlin, Heidelberg (2007).

[86] J. Bardeen, *Tunnelling from a Many-Particle Point of View*, Physical Review Letters **6**, 57 (1961).

[87] J. M. Blanco, F. Flores, and R. Pérez, *STM-theory: Image potential, chemistry and surface relaxation*, Progress in Surface Science **81**, 403 (2006).

[88] P. A. M. Dirac, *The Quantum Theory of the Emission and Absorption of Radiation*, Proceedings of the Royal Society A **114**, 243 (1927).

[89] J. Tersoff and D. R. Hamann, *Theory and Application for the Scanning Tunneling Microscope*, Physical Review Letters **50**, 1998 (1983).

[90] J. Tersoff, *Theory of the scanning tunneling microscope*, Physical Review B **31**, 805 (1985).

[91] S. Ohnishi and M. Tsukada, *Molecular orbital theory for the scanning tunneling microscopy*, Solid State Communications **71**, 391 (1989).

[92] C. J. Chen, *Origin of atomic resolution on metal surfaces in scanning tunneling microscopy*, Physical Review Letters **65**, 448 (1990).

[93] U. K. Köhler, J. E. Demuth, and R. J. Hamers, *Surface Reconstruction and the Nucleation of Palladium Silicide on Si(111)*, Physical Review Letters **60**, 2499 (1988).

[94] M. Tsukada and N. Shima, *Theory of Electronic Processes of Scanning Tunneling Microscopy*, Journal of the Physical Society of Japan **56**, 2875 (1987).

[95] J. B. Pendry, A. B. Pretre, and B. C. H. Krutzen, *Theory of the scanning tunnelling microscope*, Journal of Physics: Condensed Matter **3**, 4313 (1991).

[96] T. N. Todorov, G. A. D. Briggs, and A. P. Sutton, *Elastic quantum transport through small structures*, Journal of Physics: Condensed Matter **5**, 2389 (1993).

[97] R. Hoffmann, *A chemical and theoretical way to look at bonding on surfaces*, Reviews of Modern Physics **60**, 601 (1988).

[98] C. Sánchez-Sánchez, C. González, P. Jelinek, J. Méndez, P. L. d. Andres, J. A. Martín-Gago, and M. F. López, *Understanding atomic-resolved STM images on TiO2(110)-(1 × 1) surface by DFT calculations*, Nanotechnology **21**, 405702 (2010).

[99] P. Sautet, *Atomic adsorbate identification with the STM: A theoretical approach*, Surface Science **374**, 406 (1997).

[100] J. P. Ibe, P. P. Bey, S. L. Brandow, R. A. Brizzolara, N. A. Burnham, D. P. DiLella, K. P. Lee, C. R. K. Marrian, and R. J. Colton, *On the electrochemical etching of tips for scanning tunneling microscopy*, Journal of Vacuum Science & Technology A **8**, 3570 (1990).

[101] L. Stevens, *Herstellung von STM-Spitzen mittels elektrochemischen Ätzens*, Bachelor's thesis, Technische Universität Dortmund, Dortmund (2014).

[102] T. T. Tsong, *Atom-probe field ion microscopy: Field ion emission and surfaces and interfaces at atomic resolution*, Cambridge University Press, Cambridge (1990).

[103] D. Nečas and P. Klapetek, *Gwyddion: An open-source software for SPM data analysis*, Open Physics **10**, 99 (2012).

[104] D. Nečas and P. Klapetek, *One-dimensional autocorrelation and power spectrum density functions of irregular regions*, Ultramicroscopy **124**, 13 (2013).

[105] P. Klapetek, *Quantitative data processing in scanning probe microscopy: SPM applications for nanometrology*, Elsevier, Amsterdam (2018).

[106] J. R. Nuñez, C. R. Anderton, and R. S. Renslow, *Optimizing colormaps with consideration for color vision deficiency to enable accurate interpretation of scientific data*, PloS one **13**, e0199239 (2018).

[107] L. de Broglie, *Recherches sur la théorie des Quanta*, Annales de Physique **10**, 22 (1925).

[108] C. Davisson and L. H. Germer, *Diffraction of Electrons by a Crystal of Nickel*, Physical Review **30**, 705 (1927).

[109] G. P. Thomson and A. Reid, *Diffraction of Cathode Rays by a Thin Film*, Nature **119**, 890 (1927).

[110] M. P. Seah and W. A. Dench, *Quantitative electron spectroscopy of surfaces: A standard data base for electron inelastic mean free paths in solids*, Surface and Interface Analysis **1**, 2 (1979).

[111] H. Shinotsuka, S. Tanuma, C. J. Powell, and D. R. Penn, *Calculations of electron inelastic mean free paths. X. Data for 41 elemental solids over the 50 eV to 200 keV range with the relativistic full Penn algorithm*, Surface and Interface Analysis **47**, 871 (2015).

[112] D. Geelen, J. Jobst, E. E. Krasovskii, S. J. van der Molen, and R. M. Tromp, *Nonuniversal Transverse Electron Mean Free Path through Few-layer Graphene*, Physical Review Letters **123**, 086802 (2019).

[113] H. Lüth, *Solid Surfaces, Interfaces and Thin Films*, Springer, Berlin, Heidelberg (2010).

[114] T. Fauster, *Oberflächenphysik: Grundlagen und Methoden*, De Gruyter, München (2013).

[115] M. A. Hove, W. H. Weinberg, and C.-M. Chan, *Low-Energy Electron Diffraction*, Springer, Berlin, Heidelberg (1986).

[116] H. Ibach, *Physics of Surfaces and Interfaces*, Springer, Berlin, Heidelberg (2006).

[117] J. B. Pendry, *The application of pseudopotentials to low energy electron diffraction*, Ph.D. thesis, University of Cambridge, Cambridge (1969).

[118] K. E. Hermann and M. A. van Hove, *LEEDpat - PC-based software tool to visualize and analyze LEED patterns of substrates and overlayers,* `http://www.fhi-berlin.mpg.de/KHsoftware/LEEDpat/index.html` (Retrieved: 28.05.2021).

[119] A. Einstein, *Über einen die Erzeugung und Verwandlung des Lichtes betreffenden heuristischen Gesichtspunkt*, Annalen der Physik **322**, 132 (1905).

[120] F. de Groot and A. Kotani, *Core level spectroscopy of solids*, CRC Press, Boca Raton (2008).

[121] J. C. Vickerman and I. S. Gilmore, *Surface analysis: The principal techniques*, Wiley, Chichester (2009).

[122] S. Doniach and M. Sunjic, *Many-electron singularity in X-ray photoemission and X-ray line spectra from metals*, Journal of Physics C: Solid State Physics **3**, 285 (1970).

[123] U. Gelius, E. Basilier, S. Svensson, T. Bergmark, and K. Siegbahn, *A high resolution ESCA instrument with X-ray monochromator for gases and solids*, Journal of Electron Spectroscopy and Related Phenomena **2**, 405 (1973).

[124] R. Hesse and R. Denecke, *Improved Tougaard background calculation by introduction of fittable parameters for the inelastic electron scattering cross-section in the peak fit of photoelectron spectra with UNIFIT 2011*, Surface and Interface Analysis **43**, 1514 (2011).

[125] S. Tougaard, *Quantitative analysis of the inelastic background in surface electron spectroscopy*, Surface and Interface Analysis **11**, 453 (1988).

[126] N. Mårtensson and A. Nilsson, *Core-Level line shapes of adsorbates: effects of electronic and vibrational excitations*, Journal of Electron Spectroscopy and Related Phenomena **52**, 1 (1990).

[127] M. Tolan, T. Weis, C. Westphal, and K. Wille, *DELTA: Synchrotron light in nordrhein–westfalen*, Synchrotron Radiation News **16**, 9 (2003).

[128] K. Wille, *The physics of particle accelerators: An introduction*, Oxford University Press, Oxford (2000).

[129] C. Westphal, U. Berges, S. Dreiner, R. Follath, M. Krause, F. Schäfers, D. Schirmer, and M. Schürmann, *The plane-grating monochromator beamline at the U55 undulator for surface and interface studies at DELTA*, Journal of Electron Spectroscopy and Related Phenomena **144-147**, 1117 (2005).

[130] R. M. Martin, *Electronic Structure: Basic theory and practical methods*, Cambridge University Press, Cambridge (2020).

[131] P. Hohenberg and W. Kohn, *Inhomogeneous Electron Gas*, Physical Review **136**, 864 (1964).

[132] W. Kohn and L. J. Sham, *Self-Consistent Equations Including Exchange and Correlation Effects*, Physical Review **140**, 1133 (1965).

[133] O. T. Hofmann, E. Zojer, L. Hörmann, A. Jeindl, and R. J. Maurer, *First-principles calculations of hybrid inorganic–organic interfaces: from state-of-the-art to best practice*, Physical Chemistry Chemical Physics **23**, 8132 (2021).

[134] V. G. Ruiz, W. Liu, E. Zojer, M. Scheffler, and A. Tkatchenko, *Density-functional theory with screened van der Waals interactions for the modeling of hybrid inorganic-organic systems*, Physical Review Letters **108**, 146103 (2012).

[135] V. Blum, R. Gehrke, F. Hanke, P. Havu, V. Havu, X. Ren, K. Reuter, and M. Scheffler, *Ab initio molecular simulations with numeric atom-centered orbitals*, Computer Physics Communications **180**, 2175 (2009).

[136] F. Schönbohm, *Temperaturverhalten und Strukturbestimmung dünner Metalloxidschichten auf Siliziumoberflächen*, Ph.D. thesis, Technische Universität Dortmund, Dortmund (2013).

[137] J. A. Hochhaus, *Automatisierung der Präparation von Einkristallen*, Bachelor's thesis, Technische Universität Dortmund, Dortmund (2018).

[138] S. Hilgers, *Oberflächencharakterisierung von Einkristallen mit LEED, AES und STM*, Bachelor's thesis, Technische Universität Dortmund, Dortmund (2019).

[139] Y. Wang, N. S. Hush, and J. R. Reimers, *Simulation of the Au(111) surface reconstruction*, Physical Review B **75**, 233416 (2007).

[140] C. Seidel, *Charakterisierung organischer Adsorbate auf Silbereinkristallen mit den Meßmethoden LEED und STM*, Ph.D. thesis, Universität Stuttgart, Stuttgart (1993).

[141] P. Roese, *Untersuchung von meso-Tetraphenylporphyrin auf einer Au(111)-Oberfläche mittels Photoelektronenspektroskopie*, Masters's thesis, Technische Universität Dortmund, Dortmund (2015).

[142] G. Sauerbrey, *Verwendung von Schwingquarzen zur Wägung dünner Schichten und zur Mikrowägung*, Zeitschrift für Physik **155**, 206 (1959).

[143] A. Wittrock, *Schichtdickenbestimmung von Koffein mit einer Quarzwaage*, Bachelor's thesis, Technische Universität Dortmund, Dortmund (2018).

[144] National Institute of Standards and Technology, *Mass Spectra Caffeine*, NIST Mass Spectrometry Data Center, Gaithersburg MD (2018).

[145] J. H. Gross, *Massenspektrometrie*, Springer, Berlin, Heidelberg (2013).

[146] H. G. M. Edwards, E. Lawson, M. de Matas, L. Shields, and P. York, *Metamorphosis of caffeine hydrate and anhydrous caffeine*, Journal of the Chemical Society, Perkin Transactions **2**, 1985 (1997).

[147] E. Dichi, M. Sghaier, B. Fraisse, F. Bonhomme, and G. Keller, *New preparation by sublimation at low pressure of glycine and physicochemical study*, Journal of Alloys and Compounds **458**, 595 (2008).

[148] M. G. H. Schulte, A. Jeindl, I. Baltaci, P. Roese, M. Schmitz, U. Berges, O. T. Hofmann, and C. Westphal, *Structural investigation of caffeine monolayers on Au(111)*, Physical Review B **101**, 245414 (2020).

[149] M. Mavrikakis, P. Stoltze, and J. K. Nørskov, *Making gold less noble*, Catalysis Letters **64**, 101 (2000).

[150] R. Otero, M. Lukas, R. E. A. Kelly, W. Xu, E. Laegsgaard, I. Stensgaard, L. N. Kantorovich, and F. Besenbacher, *Elementary structural motifs in a random network of cytosine adsorbed on a gold(111) surface*, Science **319**, 312 (2008).

[151] Y.-S. Park, S.-E. Choi, H. Kim, and J. S. Lee, *Fine-Tunable Absorption of Uniformly Aligned Polyurea Thin Films for Optical Filters Using Sequentially Self-Limited Molecular Layer Deposition*, ACS Applied Materials & Interfaces **8**, 11788 (2016).

[152] L. A. Bumm, J. J. Arnold, L. F. Charles, T. D. Dunbar, D. L. Allara, and P. S. Weiss, *Directed Self-Assembly to Create Molecular Terraces with Molecularly Sharp Boundaries in Organic Monolayers*, Journal of the American Chemical Society **121**, 8017 (1999).

[153] X. He, L. Zhang, R. Chua, P. K. J. Wong, A. Arramel, Y. P. Feng, S. J. Wang, D. Chi, M. Yang, Y. L. Huang, and A. T. S. Wee, *Selective self-assembly of 2,3-diaminophenazine molecules on MoSe2 mirror twin boundaries*, Nature Communications **10**, 2847 (2019).

[154] C. J. Chen, *Introduction to scanning tunneling microscopy*, Oxford University Press, Oxford (2013).

[155] M. Lackinger, S. Griessl, W. M. Heckl, and M. Hietschold, *Coronene on Ag (111) Investigated by LEED and STM in UHV*, The Journal of Physical Chemistry B **106**, 4482 (2002).

[156] A. Maeland and T. B. Flanagan, *Lattice spacings of gold–palladium alloys*, Canadian Journal of Physics **42**, 2364 (1964).

[157] M. Yu, J. Wang, M. Mura, Q.-q. Meng, W. Xu, H. Gersen, E. Lægsgaard, I. Stensgaard, R. E. A. Kelly, J. Kjems, T. R. Linderoth, L. N. Kantorovich, and F. Besenbacher, *Homochiral xanthine quintet networks self-assembled on Au(111) surfaces*, ACS Nano **5**, 6651 (2011).

[158] J. P. Perdew, K. Burke, and M. Ernzerhof, *Generalized gradient approximation made simple*, Physical Review Letters **77**, 3865 (1996).

[159] L. Hörmann, A. Jeindl, A. T. Egger, M. Scherbela, and O. T. Hofmann, *SAMPLE: Surface structure search enabled by coarse graining and statistical learning*, Computer Physics Communications **244**, 143 (2019).

[160] B. Cordero, V. Gómez, A. E. Platero-Prats, M. Revés, J. Echeverría, E. Cremades, F. Barragán, and S. Alvarez, *Covalent radii revisited*, Dalton Transactions **21**, 2832 (2008).

[161] A. Jeindl, *Simulation Data of Caffeine on Au(111),* `https://doi.org/10.17172/NOMAD/2020.01.08-1`, NOMAD (2020).

[162] C. Colliex, J. M. Cowley, S. L. Dudarev, M. Fink, J. Gjønnes, R. Hilderbrandt, A. Howie, D. F. Lynch, L. M. Peng, G. Ren *et al.*, *Electron diffraction*, International Tables for Crystallography **C**, 259 (2006).

[163] National Institute of Standards and Technology, *X-ray Photoelectron Spectroscopy Database*, NIST Standard Reference Database 20, Gaithersburg MD (2012).

[164] K. Asami, *A precisely consistent energy calibration method for X-ray photoelectron spectroscopy*, Journal of Electron Spectroscopy and Related Phenomena **9**, 469 (1976).

[165] K. Heister, M. Zharnikov, M. Grunze, and L. S. O. Johansson, *Adsorption of Alkanethiols and Biphenylthiols on Au and Ag Substrates*, The Journal of Physical Chemistry B **105**, 4058 (2001).

[166] P. Heimann, J. F. van der Veen, and D. E. Eastman, *Structure-dependent surface core level shifts for the Au(111), (100), and (110) surfaces*, Solid State Communications **38**, 595 (1981).

[167] G. Wertheim and S. Dicenzo, *Least-squares analysis of photoemission data*, Journal of Electron Spectroscopy and Related Phenomena **37**, 57 (1985).

[168] R. W. Bernstein and J. K. Grepstad, *XPS intensity analysis for assessment of thickness and composition of thin overlayer films: Application to chemically etched GaAs(100) surfaces*, Surface and Interface Analysis **14**, 109 (1989).

[169] S. Tanuma, C. J. Powell, and D. R. Penn, *Calculations of electron inelastic mean free paths. V. Data for 14 organic compounds over the 50-2000 eV range*, Surface and Interface Analysis **21**, 165 (1994).

[170] P. Gunter and J. W. Niemantsverdriet, *Thickness determination of uniform overlayers on rough substrates by angle-dependent XPS*, Applied Surface Science **89**, 69 (1995).

[171] O. Plekan, V. Feyer, R. Richter, A. Moise, M. Coreno, K. C. Prince, I. L. Zaytseva, T. E. Moskovskaya, D. Y. Soshnikov, and A. B. Trofimov, *X-ray spectroscopy of heterocyclic biochemicals: Xanthine, hypoxanthine, and caffeine*, The Journal of Physical Chemistry A **116**, 5653 (2012).

[172] M. Giesbers, A. T. M. Marcelis, and H. Zuilhof, *Simulation of XPS C1s spectra of organic monolayers by quantum chemical methods*, Langmuir **29**, 4782 (2013).

[173] E. Frydman, H. Cohen, R. Maoz, and J. Sagiv, *Monolayer Damage in XPS Measurements As Evaluated by Independent Methods*, Langmuir **13**, 5089 (1997).

[174] P. C. Rieke, D. R. Baer, G. E. Fryxell, M. H. Engelhard, and M. S. Porter, *Beam damage of self–assembled monolayers*, Journal of Vacuum Science & Technology A **11**, 2292 (1993).

[175] A. Schöll, Y. Zou, M. Jung, T. Schmidt, R. Fink, and E. Umbach, *Line shapes and satellites in high-resolution x-ray photoelectron spectra of large pi-conjugated organic molecules*, The Journal of Chemical Physics **121**, 10260 (2004).

[176] A. Schöll, Y. Zou, T. Schmidt, R. Fink, and E. Umbach, *High-Resolution Photoemission Study of Different NTCDA Monolayers on Ag(111)*, The Journal of Physical Chemistry B **108**, 14741 (2004).

[177] A. Soltani, M. T. Baei, E. Tazikeh Lemeski, and M. Shahini, *Sensitivity of BN nano-cages to caffeine and nicotine molecules*, Superlattices and Microstructures **76**, 315 (2014).

[178] D. García-Toral, M. González-Melchor, J. F. Rivas-Silva, E. Meneses-Juárez, J. Cano-Ordaz, and G. H Cocoletzi, *Dopamine and Caffeine Encapsulation within Boron Nitride (14,0) Nanotubes: Classical Molecular Dynamics and First Principles Calculations*, The Journal of Physical Chemistry B **122**, 5885 (2018).

[179] J. Repp, G. Meyer, S. M. Stojković, A. Gourdon, and C. Joachim, *Molecules on insulating films: scanning-tunneling microscopy imaging of individual molecular orbitals*, Physical Review Letters **94**, 026803 (2005).

[180] J. Lagoute, K. Kanisawa, and S. Fölsch, *Manipulation and adsorption-site mapping of single pentacene molecules on Cu(111)*, Physical Review B **70**, 245415 (2004).

[181] M. K. Mishra, K. Mishra, A. Narayan, C. M. Reddy, and V. R. Vangala, *Structural Basis for Mechanical Anisotropy in Polymorphs of a Caffeine–Glutaric Acid Cocrystal*, Crystal Growth & Design **20**, 6306 (2020).

[182] M. Wiklund, A. Jawarowski, F. Strisland, A. Beutler, A. Sandell, R. Nyholm, S. L. Sorensen, and J. N. Andersen, *Vibrational fine structure in the C 1s photoemission spectrum of the methoxy species chemisorbed on Cu(100)*, Surface Science **418**, 210 (1998).

[183] I. L. Volkov, A. Smirnova, A. A. Makarova, Z. V. Reveguk, R. R. Ramazanov, D. Y. Usachov, V. K. Adamchuk, and A. I. Kononov, *DNA with Ionic, Atomic, and Clustered Silver: An XPS Study*, The Journal of Physical Chemistry B **121**, 2400 (2017).

[184] G. Mattioli, L. Avaldi, P. Bolognesi, J. D. Bozek, M. C. Castrovilli, J. Chiarinelli, A. Domaracka, S. Indrajith, S. Maclot, A. R. Milosavljević, C. Nicolafrancesco, C. Nicolas, and P. Rousseau, *Unravelling molecular interactions in uracil clusters*

by XPS measurements assisted by ab initio and tight-binding simulations, Scientific Reports **10**, 13081 (2020).

[185] M. G. Pamato, I. G. Wood, D. P. Dobson, S. A. Hunt, and L. Vočadlo, *The thermal expansion of gold: point defect concentrations and pre-melting in a face-centred cubic metal*, Journal of Applied Crystallography **51**, 470 (2018).

[186] F. Pendolino, *Self-assembly of molecules on nanostructured graphene*, Ph.D. thesis, Universidat Autónoma de Madrid, Madrid (2014).

[187] M. Pividori, *Self-assembled molecular structures on solid-state surfaces and in realistic environment: Ab-initio modelling*, Ph.D. thesis, Università degli Studi di Trieste, Trieste (2016).

[188] M. Descamps, N. T. Correia, P. Derollez, F. Danede, and F. Capet, *Plastic and glassy crystal states of caffeine*, The Journal of Physical Chemistry B **109**, 16092 (2005).

[189] K. Comanici, F. Buchner, K. Flechtner, T. Lukasczyk, J. M. Gottfried, H.-P. Steinrück, and H. Marbach, *Understanding the contrast mechanism in scanning tunneling microscopy (STM) images of an intermixed tetraphenylporphyrin layer on Ag(111)*, Langmuir **24**, 1897 (2008).

[190] D. Nečas, M. Valtr, and P. Klapetek, *How levelling and scan line corrections ruin roughness measurement and how to prevent it*, Scientific Reports **10**, 15294 (2020).

[191] M. Vladimirova, G. Trimarchi, A. Baldereschi, J. Weckesser, K. Kern, J. V. Barth, and A. de Vita, *Substrate-induced supramolecular ordering of functional molecules: theoretical modelling and STM investigation of the PEBA/Ag(111) system*, Acta Materialia **52**, 1589 (2004).

[192] C. Wang, H. Wang, T. Huang, X. Xue, F. Qiu, and Q. Jiang, *Generalized-stacking-fault energy and twin-boundary energy of hexagonal close-packed Au: A first-principles calculation*, Scientific Reports **5**, 1 (2015).

[193] M. Batzill, *Mirror twin grain boundaries in molybdenum dichalcogenides*, Journal of Physics: Condensed Matter **30**, 493001 (2018).

[194] P. Aref, M. Ghoreyshi, A. Jirasek, M. Satchell, and K. Bergeron, *Computational Study of Propeller–Wing Aerodynamic Interaction*, Aerospace **5**, 79 (2018).

[195] M. Habgood, *Form II Caffeine: A Case Study for Confirming and Predicting Disorder in Organic Crystals*, Crystal Growth & Design **11**, 3600 (2011).

Publications

Articles

[A1] M. G. H. Schulte, A. Jeindl, I. Baltaci, P. Roese, M. Schmitz, U. Berges, O. T. Hofmann, and C. Westphal, *Structural investigation of caffeine monolayers on Au(111)*, Physical Review B **101**, 245414 (2020).

[A2] I. Baltaci, M. G. H. Schulte, and C. Westphal, *Structural Analysis of Theobromine Monolayers on Weakly Interacting Surfaces*, Journal of Physical Chemistry C **124**, 23648 (2020).

[A3] M. Schmitz, L. Kesper, M. G. H. Schulte, P. Roese, U. Berges, and C. Westphal, *Surface and interface analysis of a low-dimensional Au-Si surface alloy on Au(110) by means of XPS and XPD*, Journal of Physics: Condensed Matter **33**, 275001 (2021).

Conference contributions

[C1] M. G. H. Schulte, I. Baltaci, P. Mehring, and C. Westphal, *Naphthalocyanine on metal surfaces studied with a variable temperature STM*, DPG Spring Meeting, Regensburg (2016).

[C2] M. G. H. Schulte, A. Budde, I. Baltaci, P. Roese, and C. Westphal, *Investigation of Caffeine Monolayer Formation on Au(111)*, DPG and EPS Spring Meeting, Berlin (2018).

[C3] M. G. H. Schulte, I. Baltaci, P. Roese, and C. Westphal, *Investigation of Self-Assembled Caffeine Monolayer Formation on Au(111)*, DPG Spring Meeting, Regensburg (2019).

[C4] M. G. H. Schulte, A. Jeindl, I. Baltaci, M. Schmitz, P. Roese, U. Berges, O. T. Hofmann, and C. Westphal, *Investigating the monolayer structure of caffeine molecules on Au(111)*, APS March Meeting, Denver, Colorado (2020).

[C5] M. G. H. Schulte, A. Jeindl, J. A. Hochhaus, I. Baltaci, M. Schmitz, U. Berges, O. T. Hofmann, and C. Westphal, *Investigation of the formation of densely packed caffeine monolayers on Au(111)*, DPG Spring Meeting, Dresden (2020).

Supervised theses

[T1] A. Budde, *Untersuchung von Koffein auf einer Au(111)-Oberfläche mit Rastertunnelmikroskopie*, Master's thesis, Technische Universität Dortmund, Dortmund (2017).

[T2] J. A. Hochhaus, *Automatisierung der Präparation von Einkristallen*, Bachelor's thesis, Technische Universität Dortmund, Dortmund (2018).

[T3] A. Wittrock, *Schichtdickenbestimmung von Koffein mit einer Quarzwaage*, Bachelor's thesis, Technische Universität Dortmund, Dortmund (2018).

[T4] S. Hilgers, *Oberflächencharakterisierung von Einkristallen mit LEED, AES und STM*, Bachelor's thesis, Technische Universität Dortmund, Dortmund (2019).

[T5] J. A. Hochhaus, *Präparation und Charakterisierung von Submonolagen Zinn auf Au(111)*, Masters's thesis, Technische Universität Dortmund, Dortmund (2020).

Acronyms

ACF	autocorrelation function
AES	Auger electron spectroscopy
DELTA	Dortmund Electron Accelerator
DFT	density functional theory
DPRF	differentially pumped rotary feedthrough
fcc	face-centered cubic
FFT	fast Fourier transform
FIB	focused ion beam
FWHM	full width at half maximum
hcp	hexagonal close-packed
HOMO	highest occupied molecular orbital
IMFP	inelastic mean free path
KS	Kohn-Sham
LHe	liquid helium
LN_2	liquid nitrogen
LEED	low-energy electron diffraction
LT-STM	low temperature scanning tunneling microscope
LUMO	lowest unoccupied molecular orbital
MBE	molecular-beam epitaxy
ML	monolayer
NIST	National Institute of Standards and Technology
NSCT	Nano-Spintronics-Cluster-Tool
OLED	organic light-emitting diode
PBN	pyrolytic boron nitride
PSDF	power spectral density function

PVD	physical vapor deposition
QCM	quartz crystal microbalance
QMS	quadrupole mass spectrometer
RMS	root mean squared roughness
RT-STM	room temperature scanning tunneling microscope
SAMPLE	surface structure search enabled by coarse graining and statistical learning
SEM	scanning electron microscope
SEMPA	scanning electron microscopy with polarization analysis
STM	scanning tunneling microscope
STS	scanning tunneling spectroscopy
UHV	ultra-high vacuum
VdW	Van der Waals force
VT-STM	variable temperature scanning tunneling microscope
XPD	x-ray photoelectron diffraction
XPS	x-ray photoelectron spectroscopy

Danksagung

Viele Menschen haben mich in den letzten Jahren beim Erstellen dieser Arbeit unterstützt, und daher möchte ich mich an dieser Stelle herzlich bei Ihnen bedanken. Ohne die Unterstützung wäre diese Arbeit nicht möglich gewesen.

Ein ganz besonderer Dank gilt Prof. Dr. Carsten Westphal, für die Möglichkeit in seiner Arbeitsgruppe auf dem Gebiet der Oberflächenphysik zu forschen und für die Betreuung dieser Arbeit. Ich danke ebenfalls Prof. Dr. Dr. Wolfgang Rhode für sein Interesse an meinem Forschungsthema und für seine Zeit das Zweitgutachten für diese Arbeit anzufertigen.

Ganz besonders möchte ich mich bei Andreas Jeindl und Prof. Dr. Oliver T. Hofmann für die intensive Zusammenarbeit und die Simulation der Koffeinstruktur bedanken.

Zusätzlich gilt mein großer Dank PD Dr. Daniel E. Bürgler und Dr. Frank Matthes für die Möglichkeit an Ihrem experimentellen Aufbau zu messen und die angenehme Aufnahme in Ihre Arbeitsgruppe.

Beim DELTA Team und besonders bei Dr. Ulf Berges möchte ich mich für die Bereitstellung der Synchrotronstrahlung bedanken. Mein Dank gilt außerdem den wissenschaftlichen Werkstätten der TU Dortmund und insbesondere Dirk Schemionek, Gisela Pike und Susanne Kralemann.

Diese Arbeit wäre niemals möglich gewesen ohne die kontinuierliche Unterstützung aller Kollegen, Vorgänger und Freunde in der Arbeitsgruppe der experimentellen Physik EIb in Dortmund. Besonders möchte ich mich bei Ismail Baltaci, Marie Schmitz, Julian Hochhaus, Lukas Kesper, Stefanie Hilgers, Adrian Wittrock, Adam Budde, Dr. Peter Roese, Dr. Richard Hönig und Dr. Ulf Berges bedanken. Darüber hinaus gilt mein Dank Julian Hochhaus, Ismail Baltaci und Marie Schmitz für Ihre hilfreichen Anmerkungen zu diesem Manuskript.

Und zu guter Letzt möchte ich mich bei meinen Freunden, meiner Familie und allen bedanken, die es mir ermöglicht haben diesen Weg so lange zu verfolgen und mich dabei tatkräftig unterstützt haben.

Vielen herzlichen Dank!